Christian Gösweiner, BSc

Hydrogen adsorption and helium interaction studies on Sb(111) using He-atom scattering experiments

MASTER THESIS

For obtaining the academic degree
Diplom-Ingenieur

Master Program of
Technical Physics

Graz University of Technology

Supervisor:
Univ.-Prof. Mag. Dr.rer.nat Wolfgang E. Ernst
Institute of Experimental Physics

Graz, May 2015

Abstract

The study of hydrogen adsorption on crystalline surfaces has yielded deep insight into the fundamental mechanisms of adsorption, desorption, surface diffusion, surface reactions or surface bonding ever since. Hydrogen is, due to its electronic simplicity, a highly suitable adsorbate for theoretical models and predictions. However, on the experimental side, many conventional detection techniques in surface science which are based on electron scattering (AES, LEED) or adsorption induced work function changes (STM) do not produce satisfying results in case of hydrogen adsorption. The strictly surface sensitive method *helium atom scattering* (HAS) in contrast provides high sensitivity also upon hydrogen adsorption because of its giant cross section for diffuse scattering. Also, HAS is able to reveal surface structure, dynamics and electronic corrugation from a wider surface area.

This work presents the first surface adsorption experiments carried out by means of helium atom scattering on the H.A.N.S (Helium Atom Nondestructive Scattering) apparatus at the Institute of Experimental Physics at TU Graz.
Measurements for the H/Sb(111)-system, which has not been reported before, are analyzed qualitatively in a temperature range from -160°C to 200°C. It is shown, that atomic hydrogen forms a saturated (1x1) superstructure on the Sb(111) surface, which can be desorbed by annealing at 200°C. At low sample temperatures in contrast, hydrogen adsorbs randomly distributed in an amorphous state. Also, the clean Sb(111) structure and its interaction potential with helium is discussed in detail using Close-Coupling calculations.
As the semimetal antimony belongs to the very promising materials class of topological insulators, the influence of adsorbed hydrogen on its conductive (111) surface is of special interest.
Within the context of this work, a source for atomic hydrogen has been installed at the H.A.N.S apparatus, where the proof for successful dissociation and an operation manual are provided in the experimental part of this thesis.

Kurzfassung

Die Untersuchung von Wasserstoff adsorbiert auf kristallinen Oberflächen hat während ihrer langen Tradition tiefe Einblicke in die fundamentalen Mechanismen von Adsorption, Desorption, Oberflächendiffusion und Oberflächen Reaktionen hervorgebracht. Wasserstoff ist, aufgrund seiner einfachen elektronischen Struktur, ein dankbares Adsorbat für theoretische Modelle und Vorhersagen. Auf experimenteller Seite hingegen gibt es viele etablierte Analysemethoden in der Oberflächenphysik, basierend auf Elektronenstreuung (AES, LEED) oder auf adsorptions-induzierten Änderungen der Austrittsarbeit (STM), welche für Wasserstoff keine zufriedenstellenden Ergebnisse liefern. Helium Atom Streuung (HAS) hingegen ist eine streng oberflächensensitive Methode, welche aufgrund ihres großen Streuquerschnittes für diffuse Streuung auch für adsorbierten Wasserstoff hohe Empfindlichkeit aufweist. Darüber hinaus können mithilfe der Helium Atom Streuung Oberflächenstruktur, Oberfächendynamik und sogar die Elektronendichteverteilung knapp über der Oberfläche bestimmt werden.

In dieser Arbeit werden die allerersten Adsorptions-Experimente, durchgeführt an der institutseigenen Atomstreu-Anlage (H.A.N.S, Helium Atom Nondestructive Scattering), vorgestellt. Vorerst rein qualitativ analysiert werden HAS- Messungen an H/Sb(111), ein System welches bislang noch nicht untersucht wurde, in einem Temperaturbereich zwischen -160°C und 200°C. Es konnte gezeigt werden, dass Wasserstoff eine (1x1) Überstruktur auf der Sb(111) Oberfläche ausbildet, welche durch Aufheizen der Probe auf 200°C wieder desorbiert werden kann. Im Niedrigtemperaturbereich hingegen ordnen sich die Wasserstoffatome nicht periodisch an, sondern bilden eine amorphe Phase. Zusätzlich wird die reine Sb(111) Oberflächenstruktur unter der Verwendung von Close-Coupling- Rechnungen, besonders im Hinblick auf das He-Sb(111) Interaktionspotential, diskutiert. Das Halbmetall Antimon gehört zur besonders vielversprechenden Materialgruppe der topologischen Isolatoren. Somit ist der Einfluss von adsorbiertem Wasserstoff auf dessen leitfähiger (111) Oberfläche von besonderem Interesse.

Um die Wasserstoff-Adsorptionsexperimente zu ermöglichen, wurde eine Quelle für atomaren Wasserstoff an der Streu-Anlage installiert. Arbeitsweise, Bedienung, und der Beweis für erfolgreiche Wasserstoffdissoziation werden im experimentellen Teil der vorliegenden Arbeit beschrieben.

EIDESSTATTLICHE ERKLÄRUNG

AFFIDAVIT

Ich erkläre an Eides statt, dass ich die vorliegende Arbeit selbstständig verfasst, andere als die angegebenen Quellen/Hilfsmittel nicht benutzt, und die den benutzten Quellen wörtlich und inhaltlich entnommenen Stellen als solche kenntlich gemacht habe. Das in TUGRAZonline hochgeladene Textdokument ist mit der vorliegenden Dissertation identisch.

I declare that I have authored this thesis independently, that I have not used other than the declared sources/resources, and that I have explicitly indicated all material which has been quoted either literally or by content from the sources used. The text document uploaded to TUGRAZonline is identical to the present doctoral dissertation.

Datum / Date

Unterschrift / Signature

Contents

List of Figures

1 Introduction

Up to now the H.A.N.S (Helium Atom Nondestructive Scatttering) apparatus of our institute has been applied exclusively to investigate the clean crystal surfaces of bismuth (Bi)[1,2,3,4,5] and antimony (Sb)[6,7,8]. This work deals with the attempt to exploit the methods suitability for studying adsorbate systems. In the field of surface science, helium atom scattering (HAS) complements standard methods like scanning tunneling microscopy (STM) for investigating surface disorder and adsorbate systems in a sense that global information on the surface is gained from a wider area including dynamic processes. In particular the investigation of adsorbed hydrogen is not easily manageable by conventional methods like field emission microscopy (FEM), field-ion microscopy (FIM) or STM due to the small change of the system's work function compared to the clean surface. Also it is not possible to exclude the possibility of hydrogen contamination on the surface of interest using Auger electron microscopy (AES).
This work should serve as an introduction to surface science and adsorption mechanisms with special focus on hydrogen adsorption and gives an overview on the possibilities of using HAS as a probe for the analysis of adsorption systems.
The H/Sb(111) system is not only interesting as a trial system to gain experience using HAS on adsorption systems, it also has not been reported so far despite the great popularity of studies of hydrogen on metals[9].
Hydrogen on metal- systems has always been a playground to understand and investigate fundamental surface effects such as bond-making, bond-breaking or diffusion processes. This is mainly because of the simplicity of the electronic structure of hydrogen atoms and molecules. There is also a great technological interest in hydrogen reactions in general, concerning hydrogen storage, bulk sorption or hydrogenation reactions.
Antimony was found to belong to the very promising material class of topological insulators, and especially the Sb(111) surface possesses unusual electronic character connected with special conduction mechanisms. Not least, the influence on these properties induced by hydrogen adsorbed on the Sb(111) surface is of valuable interest.

2 Theory

2.1 Surfaces of crystalline solids

Surface physics deals with the solid-vacuum interface; where interface refers to a small number of atomic layers separating two phases[10]. The models for describing and analyzing the physical properties of surfaces base to some degree on the concepts of bulk solid state physics[11,12], and can in parts be derived from transferring and projecting three dimensional problems into two dimensions. But of course there are more fundamental differences, most obvious, the inhomogeneous neighboring surroundings. The concept of an infinitely extended crystal obeying translational symmetries is not valid any more which has considerable consequences. The broken symmetry in one dimension leads to significantly different properties of the surface and make greater mathematical efforts necessary. Also the complexity of the topic is extended to all kinds of interactions with the outside as for example adsorption or chemical reactions. Further, defects on surfaces play an important role in many effects. The surface is everything which is neglected in traditional solid state physics concepts.

2.1.1 Surface structure

The most general way to consider surface conditions and its physical properties uses thermodynamics. In that sense, the transition from the solid bulk to its surrounding vapor (solid-vapor interface) is treated as a small layer where the pressure drops from p_{solid} to p_{vapor} continuously (see figure 2.1 a). The surface free enthalpy in this interface region, which is considered to be in thermodynamical equilibrium, can than be written as[13]

$$dG = -SdT \; + \; Vdp \; - \; Ad\gamma \; + \; \sum_i \mu_i dn_i. \tag{2.1}$$

S is the entropy, V the Volume and n the number of particles of the interface region. The *surface free energy* γ is an excess free energy per unit area which is necessary to create a unit area of surface of a system at constant temperature, volume, chemical potential

and number of particles.
The physical origin of this energy is the necessity of breaking and forming bonds between atoms or molecules to create a piece of surface. Therefore the surface energy $\gamma_{\mathbf{n}}$ is strongly dependent on the orientation of the crystal plane $\mathbf{n}$. The macroscopic equilibrium shape of the surface is governed by the minimum of the surface free energy which is given by

$$\int_A \gamma(\mathbf{n}) \;=\; min \;. \tag{2.2}$$

More on the topic can be found in books of G.A. Somorjai[14], H. Lüth[10] and A. Zangwill[13].

As already mentioned, the surface structure differs from the arrangement of the atoms in the bulk. There are several processes that can occur- as for example *reconstruction*, *relaxation* or *facetting*, which lead to altered dimensions or geometry of the surface atoms. Reasons for this alteration are the reduced dimensionality and missing neighboring atoms at the surface border. A surface is not simply generated by cutting through a crystal, but rather formed via redistribution effects of electrons and ions that lower the surface free energy with respect to the altered conditions.

Relaxation: The relaxation process does not effect the unit cell of the surface atoms but changes bond length and angle between first and second layer atoms. The surface atoms will move slightly towards a new equilibrium position. Coordination number and rotational symmetry stays the same. Normal but also lateral relaxation is possible.

Reconstruction: In this case the surface unit cell does not correspond to the bulk-projection anymore. Also rotational symmetry and coordination number will change. Reconstructed surfaces can change their structure again over different temperature ranges. There is the possibility of conservative reconstruction, where the number of surface atoms is conserved and non-conservative reconstruction where the number of surface atoms changes in the reconstructed region.

The driving force for this rearrangement (see figure 2.1 (b)) is the introduced surface free energy γ which is the energy necessary to create a unit area of surface in J/m^2. Surface structure is unfavorable compared to bulk structure because the surface free energy is always positive. Consequently, the system tends to minimize the surface area. Cu(111) has a surface energy[14] of 2.0 J/m^2, water only 0.072 J/m^2. This has a lot of physi-

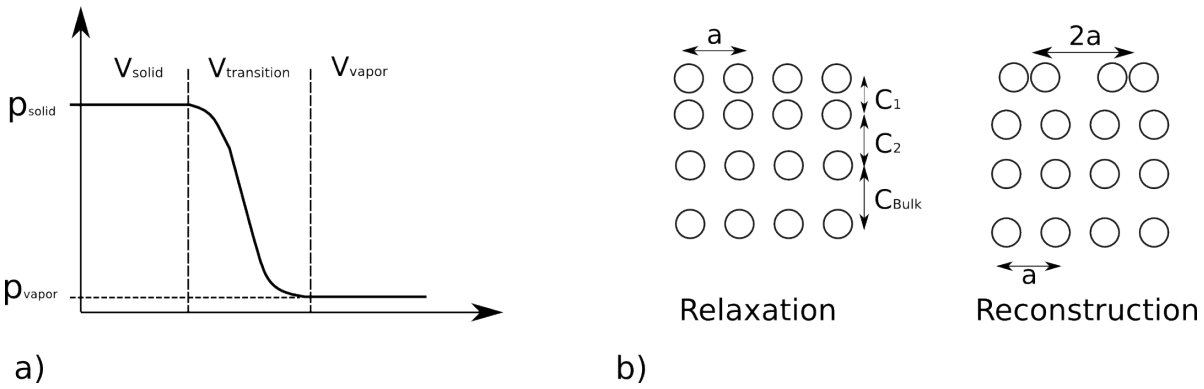

Figure 2.1: Density distribution as a function of the distance from the surface in (a). Example for simple surface relaxation and reconstruction in (b).

cal consequences when it comes to adsorption, adhesion, condensation or nucleation of particles. Metal surfaces tend to relax while for semiconductors and noble metals reconstruction appears. The minimization of surface energy is done by charge transfer, redistribution of ions or saturation of so called dangling bonds.

2.1.2 Surface description

Although the surface region is three-dimensional and contains lots of defects, it is convenient to describe surfaces using an ideal two-dimensional lattice. This simplification is valid for well prepared samples with a low density of defects and large well ordered areas. An ideal surface is defined as a cut along a certain plane through an ideal crystal. As a consequence, symmetry properties operate parallel to the surface and the concept of Bravais lattices is restricted to two dimensions. From the point group symmetry operations[12], which are compatible with 2D periodicity, five different Bravais lattices and their unit cell can be derived[10] (see figure 2.3 a).
Starting out with a cut through a particular bulk plane denoted by the Miller indices[11] (hkl), (X(hkl), eg. Sb(111)) the resulting periodic arrangement of surface atoms (lattice) can be described by a set of 2D translational vectors, the *lattice vectors* $\mathbf{R_{m,n}}$:

$$\mathbf{R_{m,n}} = n \cdot \mathbf{A}_1 + m \cdot \mathbf{A}_2 \tag{2.3}$$

$$\mathbf{R}' = \mathbf{R} + \mathbf{R_{m,n}} \tag{2.4}$$

From any point $\mathbf{R}'$ the lattice described by the integer numbers (m,n) and the primitive unit vectors $\mathbf{A}_1$ and $\mathbf{A}_2$ looks exactly the same. Its primitive unit cell spanned by $\mathbf{A}_1$

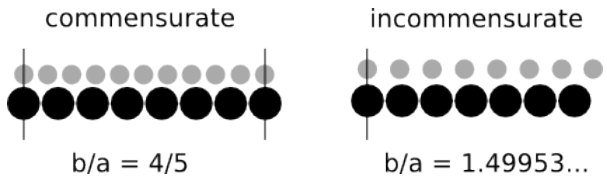

Figure 2.2: Depending on the substrate- superstructure lattice constant relation, it is possible to distinguish between a commensurate and an incommensurate overlayer. An integer, a rational or an irrational relation gives either a simple superlattice, a coincidence (commensurate) or an incoherent (incommensurate) lattice.

and $\mathbf{A}_2$ fills the whole area when repeated along the surface. Additionally to the lattice, the position of the atoms within the unit cell must be described by a basis.
For a lattice there is an infinite number of possibilities to define a unit cell. A "primitive" unit cell encloses the smallest possible area and only one lattice point while at the same time filling the whole crystal area when repeated. A very popular choice for a primitive unit cell is the so called Wigner-Seitz cell. This cell contains one lattice point in the middle and all lattice-points that are closer to this center point than to any other lattice point[12].
When it comes to real surfaces, possible reconstruction or relaxation effects of the first layer atoms and adsorbate structures have to be considered. This is done by determining a superlattice, which is a lattice superimposed on the ideal substrate surface. This superlattice can be described using the primitive lattice vectors.

$$\begin{pmatrix} \mathbf{B_1} \\ \mathbf{B_2} \end{pmatrix} = \mathbf{M} \begin{pmatrix} \mathbf{A_1} \\ \mathbf{A_2} \end{pmatrix} \tag{2.5}$$

$\mathbf{M}$ is a 2×2 matrix which can be written as

$$\mathbf{M} = \begin{pmatrix} m_{11} & m_{12} \\ m_{21} & m_{22} \end{pmatrix}. \tag{2.6}$$

This definition helps to characterize the relation between substrate and superstructure lattice using

$$B = \mid \mathbf{B_1} \times \mathbf{B_2} \mid = A \cdot det(\mathbf{M}) \tag{2.7}$$

with A and B the unit cell areas of the substrate and the superstructure lattice respectively. The value det($\mathbf{M}$) gives either an integer number, a rational number or an irrational number which gives a simple superlattice, a coincidence lattice or an incoherent lattice (see figure 2.2). A very widespread concept for describing adsorbate superstruc-

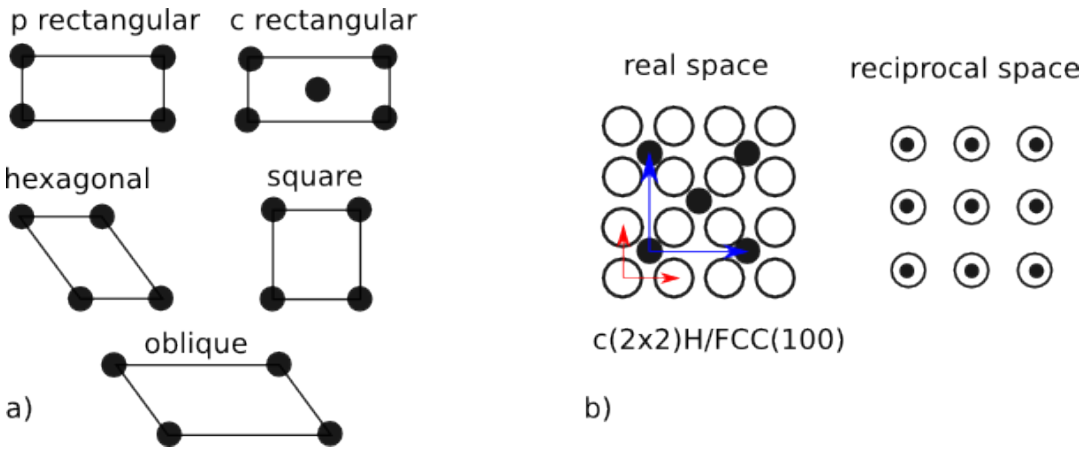

Figure 2.3: The five different Bravais lattices in two dimensions (a). A superstructure on a fcc(100) crystal surface and corresponding Wood-notation (b). As an example, H settles on the four-fold site of Ni(100) [15].

tures or reconstructions is the Wood notation. The ratio of the length of the translation vectors of the superlattice and those of the substrate p and q given via

$$\mathbf{B_1} = p\mathbf{A_1} \ , \quad \mathbf{B_2} = q\mathbf{A_2} \tag{2.8}$$

on a certain substrate X(hkl) lead to the notation

$$X(hkl)(p \times q) \tag{2.9}$$

that can be extended to $X(hkl)c(p \times q)$ when the superstructure also has a center atom. If the lattice unit vectors are not parallel to each other $X(hkl)c(p \times q) - R^\circ$ can be used, where R° is the rotation. When the superstructure is an adsorbate layer, a common notation is

$$(p \times q)A/X(hkl) \tag{2.10}$$

where A is the adsorbate type. An example would be (1x1)H/Pt(111), which is a one by one hydrogen overlayer on a Pt(111) surface, or c(2x2)H/Ni(100) as shown in figure 2.3 b.

Reciprocal lattice in 2D

When describing diffraction events, the real space lattice has to be transferred into the reciprocal space which is the space of wavevectors. The real space lattice points are

referred to plain waves $e^{i\mathbf{k}\cdot\mathbf{r}}$ and give the equation

$$e^{i\mathbf{G}\cdot\mathbf{R}} \;=\; 1 \tag{2.11}$$

when periodic boundary conditions are applied and $\mathbf{R}$ and $\mathbf{G}$ are the translation vectors of the real and the reciprocal space. The set of translation vectors $\mathbf{G_{h,k}}$ in reciprocal space obey the same periodicity as their real space counterparts and can be expressed as

$$\mathbf{G_{h,k}} \;=\; h \cdot \mathbf{A_1^*} \;+\; k \cdot \mathbf{A_2^*} \tag{2.12}$$

where the reciprocal unit vectors $\mathbf{A_1^*}$ and $\mathbf{A_2^*}$ can be evaluated from

$$\mathbf{A_1^*} \;=\; 2\pi \frac{\mathbf{A_2} \times \mathbf{n}}{\mathbf{A_1} \cdot (\mathbf{A}_2 \times \mathbf{n})} \tag{2.13}$$

$$\mathbf{A_2^*} \;=\; 2\pi \frac{\mathbf{A_1} \times \mathbf{n}}{\mathbf{A_2} \cdot (\mathbf{A}_1 \times \mathbf{n})} \tag{2.14}$$

where $\mathbf{n}$ is the surface normal unit vector and the integers h and k correspond to the Miller indices of a particular plane.
The equivalent construction of the Wigner-Seitz cell in reciprocal space is the first Brillouin zone, where crystal or surface directions in k-space usually are referred to. All crystal or surface properties can be represented within the first Brillouin zone because of translation symmetries. Further, the available points in k-space are discrete and the number of states in the first Brillouin zone corresponds to the number of unit cells in real space[11]. A transformation of a real space lattice into reciprocal space is given in figure 2.3 b.

2.1.3 Surface Defects

Real surfaces possess a number of defects of structural nature. There are point defects, as for example adatoms, vacancies, dislocations, kink or step atoms. Furthermore line defects, as for example step edges, domain boundaries and terraces can be found. Their distribution mainly depends on their formation energy and on the surface temperature. Some of them are mobile as well. This is of practical importance for many surface analysis methods where sufficiently clean and flat surfaces are needed. The most common way for many surfaces is ion sputtering, to get rid of contamination, followed by annealing at high temperature, to smooth out defects and create periodic and ”perfect” areas. Especially steps on surfaces, where adatoms preferably settle, play an important role for

adsorption or growth effects.

2.2 The lattice structure of Sb(111)

Antimony (Sb) has the atomic number 51 and belongs to group 15 of the periodic table of elements. Due to its high mass, spin-orbit coupling is very pronounced which leads to interesting electronic properties. It has been found that Sb is a topological semimetal [16] and shows good surface conductivity despite the rather bad bulk conductivity.
Antimony crystallizes in the rhombohedral A7 structure with two atoms per unit cell. Perpendicular to the [111] direction this crystal structure is built up of puckered bilayers as shown in figure 2.4 b. The weaker bonding in between these bilayers enforces a preferred cleavage direction. The Sb(111) surface is easily produced by cleaving the crystal along this plane, which gives a sixfold-symmetric layer of the top atoms (see figure 2.4 a). The Wigner-Seitz cell and its corresponding first Brillouin zone are hexagonal and possess two high symmetry directions (figure 2.4 c). The lattice constant is a = (4.3084 ± 0.0002) Å at standard conditions. Furthermore the layer distances have been determined as b = 1.50 Å and c = 2.24 Å [17].
Interestingly, it has been shown via STM [18], LEED [19] and HAS [6,7] experiments, that neither reconstructions nor mentionable relaxations occur at the (111) surface of Sb. In the paper of F. Jona [19] it is also claimed, that the Sb(111) surface is very inert against oxygen and wet-oxygen. However, oxidation of the surface occurs at elevated surface temperatures > 260 °C [20]. From the mentioned STM measurements, the amplitude of atomic corrugation along the surface is determined to (0.5 ± 0.1) Å at intermediate tip-sample distances.

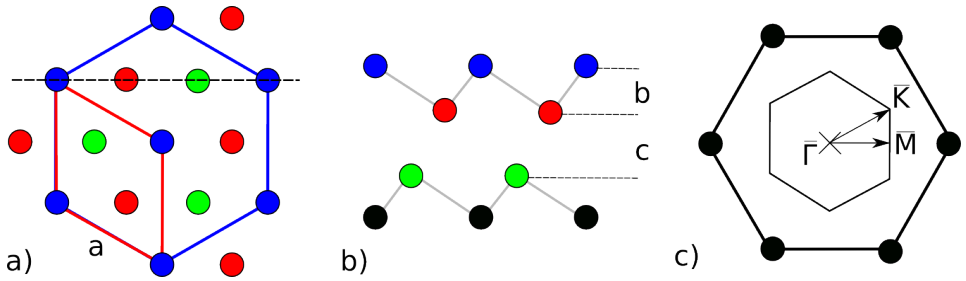

Figure 2.4: Top view of a cut perpendicular to the [111] direction through an Sb crystal and denoted unit cell of first layer atoms (a). Side view showing the puckered bilayer arrangement of the first four atom layers (b). Reciprocal lattice of first layer lattice and corresponding Wigner-Seitz cell containing the two high symmetry directions (c).

2.3 Lattice vibrations, surface phonons

For a complete description of crystal surfaces, also the dynamics of the lattice at temperatures > 0 K have to be considered. In solid crystals the ion cores perform oscillations around their equilibrium positions. This motion can be described by the so called *harmonic approximation*, where the lattice is imagined as built up from periodically arranged masses connected with Hookean springs (see figure 2.5 b). The forces between the ions result from Coulomb interactions.
Starting out with a crystal built up by N unit cells (satisfying periodic boundary conditions), each containing r ions of mass M, the ion positions can be described by the lattice vectors (figure 2.5 a)

$$\mathbf{R}_{n\alpha} = \mathbf{R}_n + \mathbf{R}_\alpha \ , \tag{2.15}$$

where the cell index n runs from 1 to N and the ion index α from 1 to r. The displacement of the ions is denoted $s_{n\alpha k}$, where k is the vector- component k = x,y,z.
The kinetic energy can then be written as

$$T(t) \ = \ \sum_{n,\alpha,k}^{N,r,K} \frac{M_\alpha}{2} \left(\frac{ds_{n,\alpha,k}}{dt} \right)^2 . \tag{2.16}$$

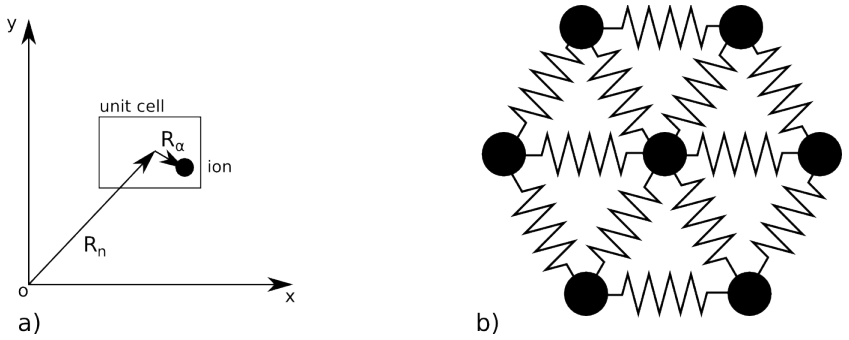

Figure 2.5: Lattice vectors denoting the ion position within a crystals unit cell (a). Two dimensional, hexagonal mass-spring system representing the harmonic approximation (b).

Taylor expanding the potential energy gives

$$W(t) \;=\; W_0(\mathbf{R}_{\mathbf{n},\alpha}) \;+\; \sum_{n,\alpha,k} \left(\frac{dW(x)}{ds_{n,\alpha,k}} \right)_{\mathbf{x}=\mathbf{R}_{\mathbf{n},\alpha}} s_{n,\alpha,k} \;+\; \ldots \tag{2.17}$$

$$\ldots \;+\; \frac{1}{2} \sum_{\substack{n,\alpha,k,\\ n',\alpha',k'}} \left(\frac{\partial^2 W(x)}{\partial s_{n,\alpha,k}\; \partial s_{n',\alpha',k'}} \right)_{\mathbf{x}=\mathbf{R}_{\mathbf{n},\alpha}} s_{n,\alpha,k}\; s_{n',\alpha',k'} \;+\; h.o.\;, \tag{2.18}$$

where the first term is the static potential and the second term corresponds to the force acting on the system in equilibrium position which both can be neglected for the dynamic case.
In accordance with the harmonic approximation, Bloch type periodic oscillations (waves) for the displacement $s_{n\alpha k}$ around the equilibrium position will further be assumed.
From the system's total energy, Newtons equations of motion can be derived which lead to an eigenvalue equation for the oscillators and solutions for the displacement $s_{n\alpha k}$. For each wavevector $\mathbf{q}$, eigenfrequencies ω of a particular polarization can be found which leads to the characteristic dispersion relation $\omega(\mathbf{q})$. Because of the in section 2.1.2 mentioned periodic boundary conditions for crystal lattices and the definition of reciprocal space, it is sufficient to restrict this relation to the first Brillouin zone of the crystal lattice and present only certain crystal directions.

Quantum mechanically, these collective oscillations of the crystal can be treated as quasiparticles, called *phonons*. From the systems total energy, the Hamilton operator can be derived and set into the Schrödinger equation, which gives the discrete eigenenergy spectrum of the phonons. In that sense phonons can be created or annihilated due to momentum and energy exchange with, for example, neutrons.

The shape of the above mentioned dispersion relation is governed by the crystal structure and the forces (binding forces, "spring constant") between the ions of the material. Also the crystal direction has to be considered when solving the equations of motion. The phonon dispersion determines a lot of material properties, like thermal conductivity, heat capacity or propagation of sound waves. In figure 2.6 a, an example for a dispersion relation of a three dimensional crystal (Sb) is given. A more exact and mathematical description on the topic can be found in the book on solid states physics of Kittel[11] or in the lecture notes of Professor Sormann[21] on theoretical solid state physics.

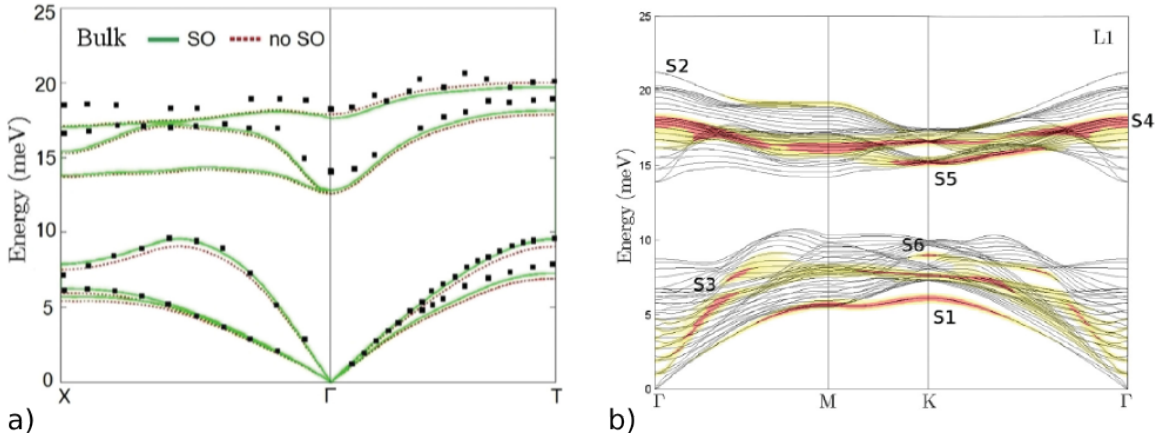

Figure 2.6: a) Bulk phonon dispersion of Sb with and without spin-orbit coupling[22]. Black squares are measured points from neutron scattering experiments. b) Surface phonon dispersion of Sb(111). Colored, labeled modes indicate localized surface modes and resonances calculated by density functional perturbation theory, taken from the publication of D. Campi et al.[22]

2.3.1 Surface phonons

For describing crystal vibrations at surfaces some modifications have to be considered when comparing them to the conditions for vibrations in the bulk material. One concern is the reduced dimensionality from three to two dimensions and the resulting broken translation invariance. Another aspect is the modified neighboring surrounding; on the vacuum side restoring forces are missing. This results in localized vibrational modes developing exclusively at the surface; *surface phonons*. Parallel to the surface these modes have wavelike behavior but the amplitude decays fast perpendicular into the bulk. Also the bulk modes are projected onto the surface, which results in a broad band of bulk modes. The dispersion relation for surface phonons therefore is slightly more complicated, as can be seen in figure 2.6 b. Such calculations are carried out using the Slab method, where a stack of 20-50 atom layers is considered to find both bulk and surface modes. The energetically lowest lying surface mode is called Rayleigh mode, but others appear as well, usually below or in between gaps of bulk modes.
These surface phonons are experimentally accessible by surface sensitive particles in the meV energy range, as for example thermal He or Ne atoms, which is more closely described in section 2.4.3.

2.3.2 The influence of adsorbates on surface dynamics

It is not possible to give a simple answer to the question of how adsorbates on a surface will influence the lattice dynamics. On the one hand it depends on the binding nature; is the adsorbate acting as an electron donor or acceptor? This influences redistribution effects of the surface. In case of a hydrogen layer on platinum, hydrogen acts as an electron donor, which has the consequence that bulk-mode conditions are almost restored also at the surface[23]. On the other hand, the adsorbate mass plays a role in damping the surface modes. When oxygen is adsorbed on platinum, it acts as electron acceptor and is therefore not restoring bulk conditions. But the platinum surface modes are lowered because of the additional mass, which in contrast would be negligible for the light hydrogen. Both effects are shown by D. Neuhaus et al.[24] via helium atom scattering.
The vibration modes of single adsorbed adatoms in contrast are dispersionless and therefore distinguishable from collective phonon modes. However, these single adsorbate vibrations can provide insight into the binding nature, orientation and site of adsorption. More on the topic is presented in section 2.8.

2.4 Helium atom scattering (HAS)

Helium atom scattering, well described for example in an article of J.P. Toennies[25] or D. Farías and K.-H. Rieder[26], is a unique method to reveal structure and dynamics of crystal surfaces in a complete nondestructive way. In particular, the possibility of creating a high intensity beam of atoms with low angular and energetic spread using supersonic expansion (see section 3.2) has enabled sophisticated high resolution experiments. Compared to other particle scattering techniques using neutrons, hydrogen, deuterium, neon or electrons, helium has a number of advantages from a surface scientists point of view.

Maybe the most outstanding property is the strict surface sensitivity which excludes bulk contributions in the signal which are always present for penetrating methods using X-ray, electrons or neutrons. Comparing the number of bulk atoms 10^{23} /cm^3 of a typical crystal solid to 10^{15} /cm^2 atoms on its surface makes clear[13] , that there always emerges a strong bulk background.
He is also a noble gas and therefore chemically, electrically and magnetically inert. Its spherical shape does not support rotational or vibrational excitations. Also its electronic excitations are out of the range of thermal surface energies. The lower mass of He compared to Ne results in a shorter, more localized interaction with the surface, suppressing multiphonon effects. Compared to hydrogen, helium is more easy to handle and detectable. The energy range of thermal He atoms of 5-300 meV and its corresponding de Broglie wavelength allow elastic diffraction from crystalline surface structures. The high inelastic cross section of He with surface phonons combined with its low energy makes it perfect for single phonon events revealing the complete surface phonon dispersion relation. Surface sensitive optical spectroscopy methods on the contrary, only access low wave-vector phonon modes.
HAS reveals information from a larger surface area compared to more local methods like STM or electron microscopy. This makes HAS to complementary method for investigating microscopic surface properties including surface dynamics, defects or contamination.

Also weak points of the method should be mentioned here. Compared to electrons, neutrons or photons, He-atoms are large and slow which leads to an interaction timescale and dimension comparable to the lattice displacement in time and space. This results in a cutoff for large wavevectors and frequencies when looking at the Fourier-

series of the solid's vibration [27]. Also He-atoms do not interact with the surface atoms in a direct way but feel a rather complicated potential build up of static and dynamic contributions of attractive (long range van der Waals) and repulsive (overlap of electron densities, Pauli repulsion) nature which is corrugated along the surface.
Also the variety of samples is restricted because UHV- conditions always have to be maintained for the experiments. Only UHV- suitable crystals having low vapor pressure which also can be cleaned under UHV conditions without including serious contamination of the chamber are suitable. However, the efforts and restrictions connected when working with UHV- apparatus are present for scattering methods in general.

2.4.1 Basic Interactions

When the He-atom is approaching a crystal surface, it will at first feel an attractive force, resulting from induced dipoles (van der Waals) and secondly, very close to the surface, feel the Pauli repulsion due to overlapping electronic orbitals. Consequently, the atom is then scattered off the surface and again passes the described potential (see section 2.5). Because of the beam's low energy, the atoms will not even penetrate up to the first layer of atoms, but be scattered off from the electronic density distribution above the surface. When impinging this region, *elastic*, *inelastic* and *resonance* effects between He atom and surface have to be considered.

- In the coherent *elastic case*, the interaction with the periodic electronic corrugation above the surface gives rise to diffraction peaks resulting from the interference of the outgoing intensity, carrying information on the surface structure.

- The energy and momentum range of the He atoms makes the surface phonon dispersion accessible for *inelastic scattering events*, which allows the determination of surface dynamics. Also the inelastic interaction with other particles, as for example adsorbed molecules, is possible and detectable.

- The occurrence of *selective adsorption resonances* produces features in the signal important for determining the shape of the interaction potential. In this case, the He atom will be trapped for a short time in a bound state of the corrugated potential and is able to move along the surface. After a subsequent scattering event, the atom will leave the bound state and can interfere with other elastically scattered atoms.

- Another very valuable property lies within the large cross section of the diffuse elastic scattered atoms and surface defects. This leads to a great sensitivity for adsorbates and defects on clean surfaces [28].

The resulting qualitative potential shape and the occurring interactions are presented in figure 2.7. A closer description of the origin of the interaction potential is given in section 2.5.

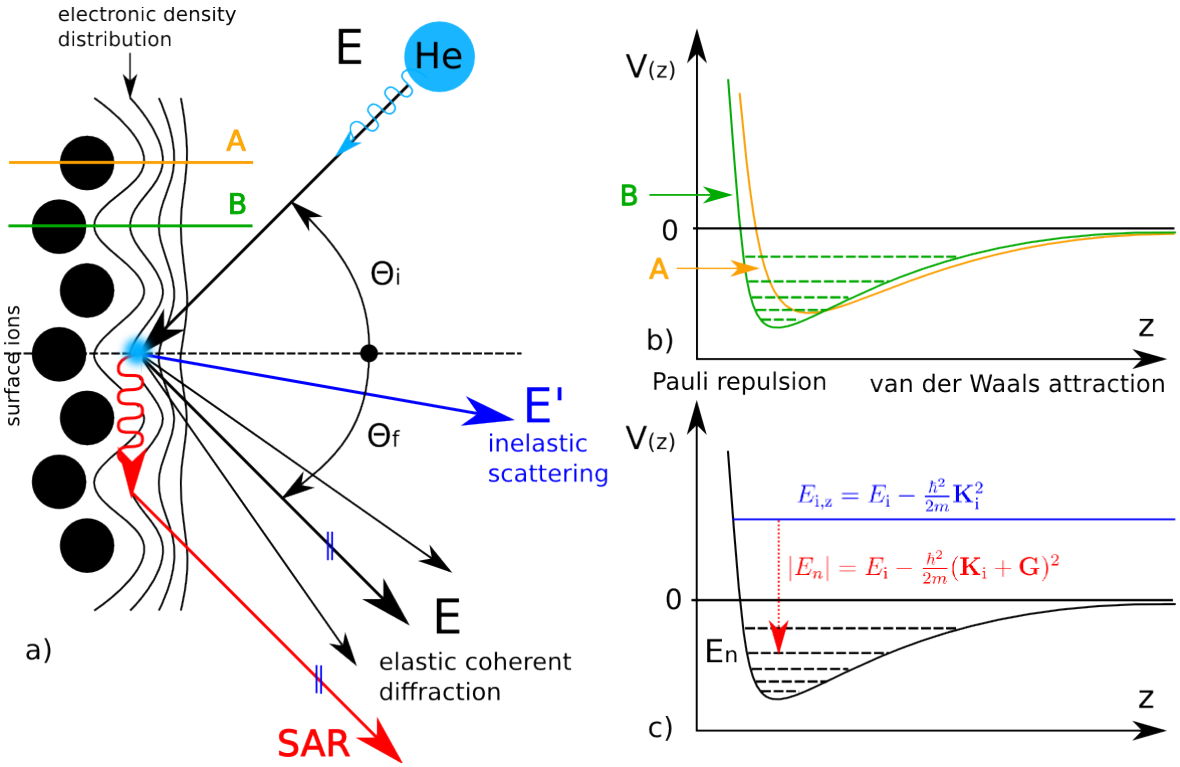

Figure 2.7: Schema of the He-surface scattering process. Basic interactions (elastic, inelastic and SAR) are shown (a) and explained in section 2.4.1. Qualitative potential shapes for two different surface positions including bound states (b). In (c) the condition for an elastic selective resonance is exemplified. When the normal energy of the incoming He atom matches a bound state plus a reciprocal lattice vector, the condition for SAR is fulfilled. The blue parallel-sign in (a) at the specular and the SAR- arrow indicate possible interference.

2.4.2 Elastic HAS

From diffraction intensity analysis, the position of scattering centers within the unit cell can be determined. Diffraction always occurs when a wave hits a periodic structure and their characteristic length dimensions are comparable. This effect results in higher intensities for distinct scattering angles as predicted by the Laue-condition.

$$\mathbf{k}_f - \mathbf{k}_i \;=\; \mathbf{G}_{h,k,l} \tag{2.19}$$

This implies, that when the final wavevector $\mathbf{k}_f$ differs from the incoming wavevector $\mathbf{k}_i$ by a reciprocal lattice vector $\mathbf{G}_{h,k,l}$, the condition for diffraction is fulfilled. Together with the law for conservation of energy for elastic scattering

$$E_f \;=\; E_i \;, \tag{2.20}$$

where E_f donates the final and E_i the incoming energy, the angles for diffraction can be determined.
The momentum $\mathbf{p}$ of a particle can be expressed by its wavevector $\mathbf{k}$

$$\mathbf{p} \;=\; \hbar \cdot \mathbf{k} \;, \tag{2.21}$$

which leads to

$$\Delta E \;=\; E_f \;-\; E_i \;=\; \frac{\Delta \mathbf{p}^2}{2m_{He}} \;=\; \frac{\hbar^2}{2m_{He}}(\mathbf{k_f}^2 \;-\; \mathbf{k_i}^2) \;=\; 0 \tag{2.22}$$

$$\Rightarrow\; \mathbf{k_f}^2 \;=\; \mathbf{k_i}^2 \;. \tag{2.23}$$

As HAS only probes the topmost layer of atoms, the problem becomes two dimensional. The periodicity along the z direction to the surface is broken, which means the distance between the reciprocal lattice points along z becomes infinitely close and so degenerate into so called lattice rods. Fig 2.8 shows the Ewald- construction for the two dimensional problem, where the Laue condition is fulfilled.
Also, our apparatus has a fixed-angle θ_{SD} between source and detector (see section 3.1), which gives an additional condition for the incoming θ_i and the final scattering angle θ_f

$$\theta_{SD} \;=\; \theta_i + \theta_f \tag{2.24}$$

Because of our two dimensional problem, equation 2.19 relaxes to

$$\mathbf{K}_f - \mathbf{K}_i \;=\; \mathbf{G}_{h,k} \;. \tag{2.25}$$

Capital letters indicate the parallel component of the incoming/final wavevector that can be derived from

$$|\mathbf{K}_i| \;=\; |\mathbf{k}_i| \cdot \; sin(\theta_i) \tag{2.26}$$

$$|\mathbf{K}_f| \;=\; |\mathbf{k}_f| \cdot \; sin(\theta_f) \;. \tag{2.27}$$

Combining equation 2.23, 2.24 and 2.25 and assuming $\mathbf{K_i}$ and $\mathbf{K_f}$ parallel to $\mathbf{G_{h,k}}$ gives

$$\theta_i \;=\; \frac{\theta_{SD}}{2} \;-\; \arcsin\left[\frac{|\mathbf{G}_{h,k}|}{2|\mathbf{k}_i| cos(\frac{\theta_{SD}}{2})}\right] \;. \tag{2.28}$$

This equation can be used to determine the length of the reciprocal lattice vector when the corresponding incidence angles for diffraction are measured via rotating the sample around θ_i and the incident beam energy (see equation 3.2) is known. The real positions of the scattering centers on the surface can be revealed carrying out measurements in different lattice directions, scanning along θ_i and using the definition of the reciprocal lattice (see section 2.1.2).
The diffracted intensities on the contrary contain information on the corrugation of the periodic scattering structure which will be discussed in section 2.6.

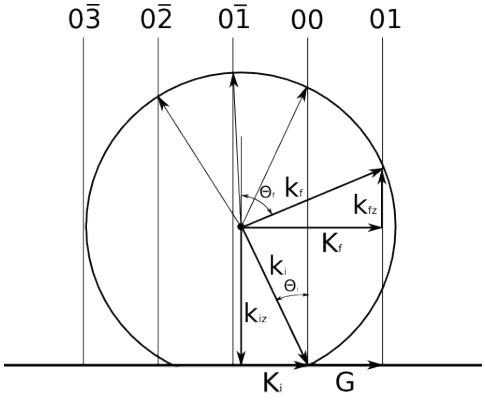

Figure 2.8: Ewald construction in two dimensions. The intersection of the Ewald-sphere with the lattice rods indicates the diffraction condition.

2.4.3 Inelastic HAS

When He-atoms scatter off the surface they can, besides being elastically diffracted, lose or gain energy due to inelastic interaction with accessible quasiparticles or adsorbates on the surface. In the majority of cases it will be an interaction with surface phonons[29], which are introduced in section 2.3.1, but also plasmon or electron-hole excitations are possible[30]. As a consequence, all measurements will exhibit a background originating from inelastic contributions. Using time-of-flight (TOF) measurements (see section 3.4) the energy transfer of the helium atoms to or from the surface can be determined.
From the equations for conservation of energy and momentum for the inelastic case, assuming only single phonon events and in plane scattering, we can find

$$E_f \;=\; E_i \;\pm\; \hbar\omega \tag{2.29}$$

$$\mathbf{K}_f \;=\; \mathbf{K}_i \;\pm\; \Delta K \;. \tag{2.30}$$

Together with equation 2.24 and 2.26 the so called *scan-curve* can be derived[31]:

$$\frac{\Delta E}{E_i} \;+\; 1 \;=\; \frac{\sin^2(\theta_i)}{\sin^2(\theta_{SD}-\theta_i)}\left(1 \;+\; \frac{\Delta K}{K_i}\right)^2 \tag{2.31}$$

The inelastic event is described by the phonon energy $\pm\hbar\omega$, which can be transfered to (+, phonon annihilation) or taken from (−, phonon creation) the impinging He-atom. ΔK is the occurring momentum transfer where (+) means backward and (−) forward phonon scattering.
The scan curve defines the experimentally accessible energy-momentum range. For particular beam conditions, given by its incident energy E_i and angle θ_i, the possible energy and momentum transfer dependence during a scattering event is restricted. When measuring ΔE via TOF measurements, the corresponding momentum transfer $\Delta\mathbf{K}$ can be calculated that way via equation 2.31.
Shifting the scan curve via altering the beam conditions in the ΔE - ΔK space probes the whole Brillouin-zone of the analyzed crystal.

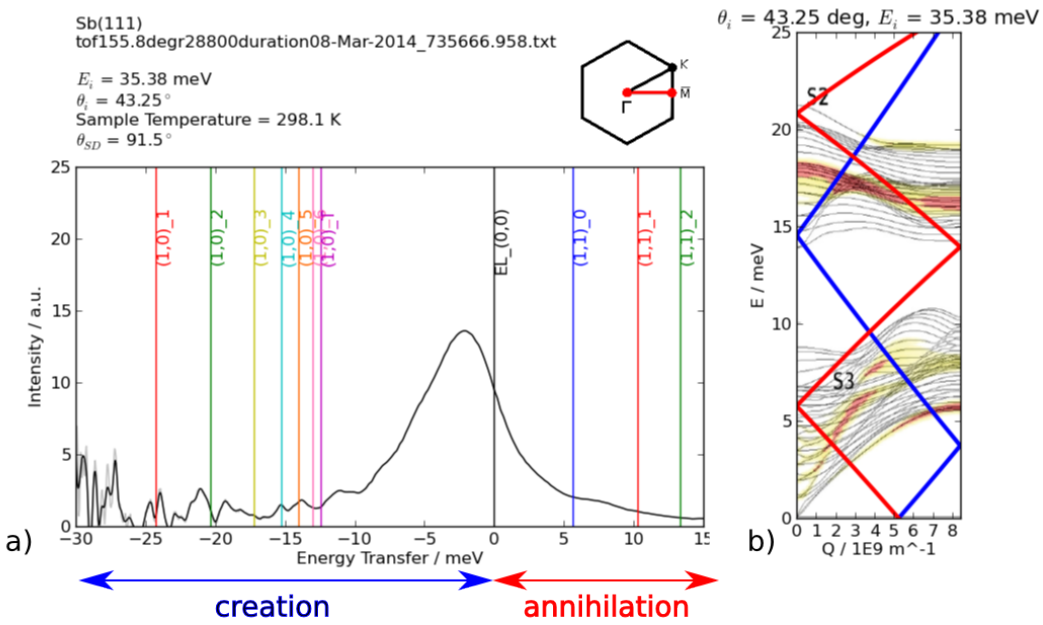

Figure 2.9: Inelastic HAS measurement (TOF) in (a) for a particular scattering condition. Intensity of the He beam versus energy transfer to the surface. Zero energy transfer corresponds to the diffuse elastic intensity. Vertical lines denote possible resonances for lattice vectors. In (b) the corresponding scan-curve for phonon creation (blue) and annihilation (red) is plotted in the first Brillouin zone along Γ-M. In the background a DFT-calculation of the surface phonon dispersion is shown[22]

.

2.4.4 Selective adsorption resonances

A less straightforward effect producing intensity features in the diffraction spectrum as well as in TOF-measurements emerges from so called *selective adsorption resonances* (SARs)[32]. The particle-surface interaction potential (section 2.5) gives rise to a discrete spectrum of bound states which can also be involved in the scattering process. Identifying the resulting features in a measured angular or TOF-spectrum makes it possible to derive these bound state energies and consequently describe and fit the responsible interaction potential.

The SARs mechanism can be described as follows: An incoming atom is transferred into a bound state via diffraction which corresponds to a perpendicular energy $E_z \sim \mathbf{k}_z^2 = -|\varepsilon_n| < 0$ after the scattering process. The atom is now bound to the surface in this transient state but moves parallel along the surface with an energy bigger than the incident energy $\mathrm{E} = E_i + |\varepsilon_n|$. After some time, the bound atom will scatter off the surface again, producing an outgoing wave. This outgoing wave and the direct elastically scattered beam

can interfere destructively or constructively leading to the mentioned intensity features (see figure 2.7). Conservation of energy for the described process can be written as

$$\mathbf{k}_i^2 \;=\; \mathbf{K}_i^2 \;-\; \frac{2m}{\hbar^2}|\varepsilon_n| \;. \tag{2.32}$$

Additionally the the parallel momentum $\mathbf{K}_i$ must be equal to a reciprocal lattice vector $\mathbf{G}_{hk}$ for satisfying Bragg's law. Splitting $\mathbf{G}_{hk}$ into a component parallel $\mathbf{G}_{||}$ and perpendicular $\mathbf{G}_{\perp}$ to the incident scattering direction and obeying Bragg's law, equation 2.32 becomes

$$\mathbf{k}_i^2 \;=\; (\mathbf{K}_i \;+\; \mathbf{G}_{||})^2 \;+\; \mathbf{G}_{\perp}^2 \;-\; \frac{2m}{\hbar^2}|\varepsilon_n| \;. \tag{2.33}$$

Purely elastic resonances as described above only alter the intensities of the elastic or a diffracted beam. However, the resonant scattering process is also possible when the He-atom is entering or leaving the transient bound state inelastically where a surface phonon with momentum $\mathbf{Q}$ and energy E($\mathbf{Q}$) is involved. Equation 2.33 then becomes

$$\mathbf{k}_i^2 \;=\; (\mathbf{K}_i \;+\; \mathbf{G}_{||} \;+\; \mathbf{Q}_{||})^2 \;+\; \mathbf{G}_{\perp}^2 \;+\; \mathbf{Q}_{\perp}^2 \;\pm\; E(\mathbf{Q}) \;-\; \frac{2m}{\hbar^2}|\varepsilon_n| \;. \tag{2.34}$$

The subscripts $||$ and $\perp$ again denote components parallel and perpendicular to the incoming wavevector $\mathbf{k}_i$.
Such inelastic resonant scattering also produces intensity features in between diffraction peaks and in the TOF-spectrum. The involved phonon is determined by the scancurve given by the incoming beam conditions and the surface phonon dispersion.
A careful analysis of TOF and angular scans enables determination of the interaction potential's bound state levels. These energies are the basis for fitting an adequate potential shape (section 4.1) and therefore the basis for calculating the intensities using Close-Coupling methods (section 2.6).

2.5 Particle- surface interaction

The particle- surface interaction potential is the key for describing and understanding all effects occurring in scattering experiments. A very detailed review of H. Hoinkes [33] deals with theoretical origin as well as experimental determination of gas-surface potentials. In several other publications [34] [35] [32], these considerations are expanded and applied to quantum mechanical atom-surface scattering models including dynamical and inelastic contributions. Following earlier works of our group [31] [36] [37],a brief introduction will be

given here.
First it should be mentioned that at thermal energies of the incoming particle, reaching from 10 to 100 meV, there is no chance for the atom to penetrate up to the first layer atoms of the surface and the turning point will be in the region of the electron density distribution above the surface. Also no charge exchange contributions need to be considered so that for example no covalent bonding will be expected and the maximum attractive energy lies within the energy range of the incoming particle.
Starting with a static lattice, where the thermal vibrations are averaged out, the potential has to describe three main regions acting on the particle when approaching the surface along the z coordinate (see figure 2.7 b):

- Far away from the surface the particle will feel van der Waals forces arising from dipole fluctuation of polarizable atoms or molecules. This is an attractive force that can be derived from second order perturbation theory of Coulomb forces between neutral atoms (London dispersion forces). As the approaching particle is interacting with all the atoms on the surface their influence will average out and the potential can be assumed to be constant parallel to the surface.

- Close to the surface the particle will experience a strong repulsion of overlapping electron orbitals resulting from the Pauli exclusion principle. In detail, the electron shell of the impinging particle interacts with the electron density distribution on the surface. For crystals that exhibit ionic binding character with strongly localized electron orbitals varying according to the arrangement of the underlying ions, also the arising repulsive force will exhibit a lateral dependency along the surface. This periodic modulation of the repulsive part of the potential is referred to as *corrugation* of the crystal surface and can be probed and quantified by diffracting particles. The more pronounced corrugation of insulators and semiconductors usually produces stronger diffraction intensities than the shallow corrugation of metals.

- In the transient region between the attractive and the repulsive part the potential possesses a minimum and exhibits bound state levels describing so called *selective adsorption resonances* (section 2.4.4). A particle can be trapped in such a state for a short time ($\approx 10^{-12}$ s), traveling along the surface and scattered off again.

Although the true potential shape is unknown there are theoretically justified models that can be used. A good starting point for a reasonable potential shape is the well

known Lenard-Jones particle-particle interaction potential. It is a sum of exponentials describing the long range attractive part correctly and also giving a realistic repulsive part:

$$V_{LJ}(r) \;=\; 4\epsilon\left[\left(\frac{\sigma}{r}\right)^{12} \;-\; \left(\frac{\sigma}{r}\right)^{6}\right] \tag{2.35}$$

In equation 2.35, ϵ is the potential depth and σ is the distance where the interaction energy turns from a positive into a negative contribution. The potential minimum can be found at $r_m = 2^{1/6}\sigma$. Carrying out a pair-wise summation over all surface atoms will lead to the 9-3 potential

$$V_{9-3}(d) \;=\; \frac{2}{3}\pi\epsilon\sigma^3\left[\frac{2}{15}\left(\frac{\sigma}{d}\right)^{9} \;-\; \left(\frac{\sigma}{d}\right)^{3}\right] \tag{2.36}$$

where d is the distance from the surface. The integration can be found in the book of W. A. Steele[35]. This potential already describes the surface- particle interaction quite well.
Another potential, which has a mathematical very handy form, is the Morse potential. It is a sum of exponentials and its one dimensional form can be written as

$$V_{M,1D}(r) \;=\; \epsilon\left(e^{-2\kappa r} \;-\; 2\cdot e^{-\kappa r}\right)\;. \tag{2.37}$$

The strength of the increase/decrease of the exponential function is described by the stiffness parameter κ and ϵ again gives the potential depth. However, the attractive part of this potential does decay too fast and is not describing the long range van der Waals forces adequately.

Looking at our problem of describing the scattering process on a two dimensional lattice of atoms, the considerations have to be expanded to a three dimensional potential reproducing the lattice periodicity and its corrugation parallel to the surface. Also the mathematical formulation has to be suited to the later introduced Close-Coupling algorithm for calculating scattering intensities (section 2.6).
For a periodic surface the potential V($\mathbf{r}$) can generally be expressed in terms of a Fourier expansion of its two dimensional reciprocal lattice vectors:

$$V(\mathbf{r}) \;=\; \sum_{\mathbf{G}} V_{\mathbf{G}}(z)e^{i\mathbf{G}\cdot\mathbf{R}} \tag{2.38}$$

The position of the particle from the surface is $\mathbf{r} = (\mathbf{R},z)$ and $\mathbf{G} = \mathbf{G}_{hk}$ is a reciprocal lattice vector of the two-dimensional surface (section 2.1.2). For $\mathbf{G} = \mathbf{0}$ the Fourier coefficient $V_{\mathbf{0}}(z)$ corresponds to the laterally and thermally averaged central interaction potential which has to fulfill the properties described above. The higher terms $V_{\mathbf{G}}$ represent the couplings to other reciprocal lattice vectors and therefore describe the diffraction.

$$V_{\mathbf{G}}(\mathbf{z}) \;=\; \frac{1}{\Sigma}\int_{\Sigma} V(\mathbf{r})e^{-i\mathbf{G}\cdot\mathbf{R}}d\mathbf{R} \tag{2.39}$$

with the unit cell area Σ.

A very purposeful choice for V($\mathbf{r}$) is using a three dimensional Morse potential with a repulsive part following the surface corrugation $\xi(\mathbf{R})$,

$$V_{CMP}(\mathbf{R},z) \;=\; D\left[\frac{1}{\nu_0}e^{-2\kappa[z-\xi(\mathbf{R})]} - 2e^{-\kappa z}\right], \tag{2.40}$$

where ν_0 is the surface average of the exponential of the corrugation function

$$\nu_{\mathbf{G}} \;=\; \frac{1}{\Sigma}\int_{\Sigma} e^{-i\mathbf{G}\cdot\mathbf{R}}e^{2\kappa\xi(\mathbf{R})}d\mathbf{R}\;. \tag{2.41}$$

with $\mathbf{G} = \mathbf{0}$. Equation 2.40 is the so called *Corrugated Morse Potential (CMP)* which results, when inserted into equation 2.39, in a very simple expression for the coupling terms:

$$V_{\mathbf{G}}(z) \;=\; D\frac{\nu_{\mathbf{G}}}{\nu_{\mathbf{0}}}e^{-2\kappa z} \tag{2.42}$$

The constant couplings are simply multiplied by a z-dependent exponential factor. For a given surface structure $\xi(\mathbf{R})$ also an analytical solution for the integral 2.41 can be found. This has been done for the Sb(111) surface and can be found in the paper of P. Kraus et al.[8].

The coupling term for $\mathbf{G} = \mathbf{0}$ in equation 2.38 gives the central potential which is a simple Morse potential

$$V_{\mathbf{0}}(z) \;=\; D\left[e^{-2\kappa z} \;-\; 2e^{-\kappa z}\right], \tag{2.43}$$

with the stiffness κ and the well depth D. The potential also supports bound state levels that can be found using

$$\epsilon_n = -D + \hbar\omega(n+1/2)[1-(n+1/2)/2\gamma] \tag{2.44}$$

Here n is the energy level, $\gamma = 2D/\hbar\omega$ and ω is the harmonic frequency $\omega = \sqrt{2\kappa^2 D/m}$ of a bound particle of mass m.

This central potential can in fact be chosen independently from the higher coupling terms where the CMP delivers an analytical expression. The central term involves the long range potential contribution, whereas the coupling terms are decaying exponentially with distance from the surface and represent the repulsive part. The couplings also include the periodic surface corrugation $\xi(\mathbf{R})$. A stronger corrugation requires a higher number of coupling terms for an adequate description.
As a result, another potential can be chosen for $V_{\mathbf{0}}(z)$ describing the attractive part more conveniently while still using the analytical form of the couplings $V_{\mathbf{G}}(z)$ in equation 2.41 and 2.42.

A mathematical description of the sixfold symmetric Sb(111) lattice (see section 2.2) in particular is

$$\xi(x,y) = \xi_0 \cdot \left(\cos\left[\frac{2\pi}{a}\left(x - \frac{y}{\sqrt{3}} \right) \right] + \cos\left[\frac{2\pi}{a}\left(x + \frac{y}{\sqrt{3}} \right) \right] \right) + \xi_0 \cdot \cos\left[\frac{2\pi}{a} \cdot \frac{2y}{\sqrt{3}} \right]. \quad (2.45)$$

2.5.1 Model Potentials

Literature[33] [32] [35] suggests a variety of potential shapes which differ in the capability of describing the physical forces as well in their their mathematical handiness. Also they provide different free parameters which can be fitted to experimentally obtained data.

Morse Potential (MP)[38,39]

$$V_{00}^{\mathrm{M}}(z) = D\left[e^{-2\kappa z} - 2e^{-\kappa z} \right]. \quad (2.46)$$

$$\epsilon_j = -\left[\sqrt{D} - \frac{\hbar\kappa}{\sqrt{2m}}\left(j + \frac{1}{2} \right) \right]^2 \quad (2.47)$$

Hybrid Morse Potential (HMP)[32]

$$V_{00}^{\mathrm{HM}}(z) = V_{00}^{\mathrm{M}}(z) \text{ for } z < z_{\mathrm{p}} \quad (2.48)$$
$$V_{00}^{\mathrm{HM}}(z) = -C_3 z^{-3} \text{ for } z \geq z_{\mathrm{p}}$$

where C_3 is chosen for continuity at the inflection point z_p. This potential improves the Morse potential since it displays the right asymptotic behavior.

Shifted Morse Potential (SMP) [40]

$$V_{00}^{\mathrm{SM}}(z) = D\left[e^{-2\kappa z} - 2e^{-\kappa z} - \Delta\right] \tag{2.49}$$

with Δ the shift parameter and a total well-depth of $D(1+\Delta)$.

$$\epsilon_j = -D(1+\Delta) + \hbar\kappa\sqrt{\frac{2D}{m}}\left(j+\frac{1}{2}\right) - \left(\frac{\hbar^2\kappa^2}{2m}\right)\left(j+\frac{1}{2}\right)^2 \tag{2.50}$$

Shifted Morse Hybrid Potential (SMHP) [40]

$$\begin{aligned} V_{00}^{\mathrm{SMH}}(z) &= V_{00}^{\mathrm{SM}}(z) \text{ for } z < z_\mathrm{p} \\ V_{00}^{\mathrm{SMH}}(z) &= -C_3 z^{-3} \text{ for } z \geq z_\mathrm{p} \end{aligned} \tag{2.51}$$

where C_3 is chosen for continuity at the inflection point z_p.

(9-3) Potential [41]

$$V_{00}^{9-3}(z) = \frac{\sqrt{27}}{2} D\left[\left(\frac{\sigma}{(z-z_\mathrm{e})}\right)^9 - \left(\frac{\sigma}{(z-z_\mathrm{e})}\right)^3\right] \tag{2.52}$$

$$\epsilon_j \simeq -D\left[1 - \frac{\pi\hbar\left(j+\frac{1}{2}\right)}{3.07\sigma\sqrt{2mD}}\right]^6 \tag{2.53}$$

(12-3) Potential [42]

$$V_{00}^{12-3}(z) = \frac{D}{3}\left[\left(\frac{\sigma}{(z-z_\mathrm{e})}\right)^{12} - 4\left(\frac{\sigma}{(z-z_\mathrm{e})}\right)^3\right] \tag{2.54}$$

Exponential-3 Potential (Exp3) [43]

$$V_{00}^{\exp-3}(z) = \frac{\kappa z_0}{\kappa z_0 - 3} D \left[\frac{3}{\kappa z_0} e^{-\kappa(z - z_0 + z_e)} - \left(\frac{z_0}{z + z_e} \right)^3 \right] \tag{2.55}$$

Variable Exponent Potential (Var-Ex) [44]

$$V_{00}^{\mathrm{VE}}(z) = D \left[\left(1 + \frac{\kappa z}{p} \right)^{-2p} - 2 \left(1 + \frac{\kappa z}{p} \right)^{-p} \right] \tag{2.56}$$

with the variable exponent p as a fit parameter.

$$\epsilon_j = -D \left[(1 - \frac{\delta}{A^2})^{-\frac{1}{s}} - \frac{j + \frac{1}{2}}{As} \right]^s \tag{2.57}$$

with $\delta = \frac{1+1/p}{32p}$, $A = \frac{\sqrt{2mD}}{2\hbar\kappa}$ and $\frac{1}{s} = \frac{1}{2} - \frac{1}{4p} \cdot (3 + \frac{1}{p})$.

2.5.2 Dynamical potential

For a complete treatment of the scattering process also inelastic events have to be taken into account and the static lattice considerations need to be expanded. The surface atoms vibrate around their equilibrium positions which can be described via

$$\mathbf{r}_j \;=\; \mathbf{R}_j + \mathbf{u}_j, \tag{2.58}$$

where $\mathbf{R}_j$ defines the position on the fixed lattice and $\mathbf{u}_j$ describes the time-dependent displacement of atom j (the index j refers to the atom within the unit cell in a distinct layer). Accordingly an expression for the dynamic interaction potential can be written as a Taylor expansion up to first order:

$$V(\mathbf{r}, t) = V_{stat} + V_{dyn} \approx V(\mathbf{r}) + \sum_j \mathbf{u}_j \cdot \nabla V(\mathbf{r}) \tag{2.59}$$

V(r) is the already introduced time and spatially averaged static potential and $\nabla V(R)$ is the force exerted from the lattice potential on the incoming particle. The displacement

$\mathbf{u}_j$ parallel to the lattice is assumed as harmonic:

$$\mathbf{u}(\mathbf{R},t) = \sum_{\mathbf{Q},\nu} \mathbf{A}(\mathbf{Q},\nu,T) e^{i\mathbf{Q}\cdot\mathbf{R}} cos(\omega_\nu(\mathbf{Q})t) \ , \tag{2.60}$$

where $\mathbf{A}$ denotes polarization and amplitude and ($\mathbf{Q}$,ν) are the phonon quantum numbers indicating a phonon with momentum $\mathbf{Q}$ in mode ν. For vertical phonon modes perpendicular to the surface the displacement behaves Gaussian-like[45]:

$$\mathbf{u}(\mathbf{z},t) \ = \ \mathbf{u}_{\mathbf{z},0} \ e^{\frac{-z^2}{z_c^2}} cos(\omega t) \ , \tag{2.61}$$

where ω is the frequency of the active phonon mode, $\mathbf{u}_{\mathbf{z},0}$ its amplitude at t=0 and z_c the width of the Gaussian distribution.
Using equation 2.38 the force on an impinging particle can be written as

$$\mathbf{F}_\mathbf{G}(z) \ = \ -\nabla V(\mathbf{r}) \ = \ -\sum_\mathbf{G} \left[i\mathbf{G}\cdot\mathbf{V}_\mathbf{G}(z), \mathbf{V'}_\mathbf{G}(z) \right] e^{i\mathbf{G}\mathbf{R}} \ . \tag{2.62}$$

This treatment finally leads to the consideration of the lattice dynamics in the interaction potential.

2.6 Methods describing the scattering process

There exists a number of theoretical approaches[26,32] to describe the He-surface scattering process used for calculating and predicting the appearing intensities of the scattered He-beam. Starting point for all methods is the Schrödinger equation of the scattering problem

$$\left[-\frac{\hbar^2}{2m}\nabla^2 \ + \ V(\mathbf{r}) \right] \Psi(\mathbf{r}) \ = \ E\Psi(\mathbf{r}) \ , \tag{2.63}$$

with the particle-surface interaction potential $V(\mathbf{r})$ as the central part of the equation. This potential is often simplified by the hard corrugated wall model (HCW), where no attractive part and a infinitely steep repulsive part is assumed. Using the Rayleigh assumption for plane waves, lots of surface analysis has been carried out successfully. A close description of these approximative methods can be found in the thesis of A. Tamtögl[31] or M. Mayrhofer -Reinhartshuber[36].
The aim of the efforts is of course to fit variable parameters of the calculation, like the exact structure of the surface unit cell, its electronic corrugation along the x-y

plane, the distribution of defects and terraces or the arrangement of adsorbates, in short; its interaction potential, to experimentally found data. Including also inelastic contributions, as for example originating from surface phonons, into the calculations is a great challenge promising more exact results.
The most sophisticated method is a fully quantum mechanical model- referred to as "the Close-Coupling (CC) method" which is - when including inelastic effects - the most natural way to solve the problem and therefore probably closest to the truth. In this chapter the elastic and inelastic CC will be presented. In section 4.1 the elastic CC method is applied to the He-Sb(111) structure.

2.6.1 Elastic Close Coupling

Starting out with the time independent Schrödinger equation (from now on $-\frac{\hbar^2}{2m}$ is set to 1),

$$\left[-\nabla^2 \; + \; V(\mathbf{r}) \; - \; \mathbf{k}_i^2\right] \Psi(\mathbf{r}) \; = \; 0, \tag{2.64}$$

developing the Bloch-form wave function in terms of the reciprocal lattice vectors

$$\Psi(\mathbf{r}) \; = \; e^{i\mathbf{K}_i \cdot \mathbf{R}} \sum_{\mathbf{G}} \Psi_{\mathbf{G}}(z) e^{i\mathbf{G}\cdot\mathbf{R}} \tag{2.65}$$

and using the potential V($\mathbf{r}$) introduced in section 2.5 one ends up with a set of coupled differential equations when multiplying both sides with exp(-i($\mathbf{K}_i$ + $\mathbf{G} \cdot \mathbf{R}$)) and integrating over a unit cell area:

$$\left[\frac{\mathrm{d}^2}{\mathrm{d}z^2} + \mathbf{k}_{\mathbf{G},z}^2 - V_{\mathbf{0}}(z)\right] \Psi_{\mathbf{G}}(z) \; = \; \sum_{\mathbf{G}' \neq \mathbf{G}} V_{\mathbf{G}-\mathbf{G}'}(z).\Psi_{\mathbf{G}'}(z). \tag{2.66}$$

When solving this equation for one wavefunction $\psi_{\mathbf{G}}$(z) all other wavefunctions and the corresponding Fourier-terms of the potential (*couplings*) have to be known. The couplings determine the partition of the incoming intensity into the outgoing waves. The z-component of the kinetic energy of the scattered particle $\mathbf{k}_{\mathbf{G},z}^2$ can be expressed as

$$\mathbf{k}_{\mathbf{G},z}^2 \; = \; \mathbf{k}_i^2 - (\mathbf{K}_i + \mathbf{G})^2. \tag{2.67}$$

Set into equation 2.66, an effective potential $V_{00} + (\mathbf{K}_i + \mathbf{G})^2$ called *channel* can be identified which is governing the scattering process for each reciprocal lattice vector and is therefore labeled accordingly, eg. (h,k)-channel. The asymptotic energy (AE)

$(\mathbf{K}_i + \mathbf{G})^2$ compared with $\mathbf{k}^2_{\mathbf{G},z}$ contains information whether a particular channel is accessible or not. Three cases can be distinguished: $(\mathbf{K}_i + \mathbf{G})^2 < \mathbf{k}^2_{\mathbf{G},z}$ denotes open channels. There is a finite number of open channels and the corresponding states are written as $|\mathbf{K}_i + \mathbf{G}, \mathbf{k}^2_{\mathbf{G},z}\rangle$. Closed channels obey $(\mathbf{K}_i + \mathbf{G})^2 - D > \mathbf{k}^2_{\mathbf{G},z}$, where D is the potential depth. A particle can not scatter into these channels, nevertheless some need to be included into calculation for numerical convergence. However, in the region where $(\mathbf{K}_i+\mathbf{G})^2-D < \mathbf{k}^2_{\mathbf{G},z} < (\mathbf{K}_i+\mathbf{G})^2$ the particle can scatter into a discrete potential bound state which leads to discrete states labeled by $|\mathbf{K}_i + \mathbf{G}, \nu\rangle$ where ν gives the involved bound state. All these conditions depend on scattering geometry and energy and result in so called *moving thresholds*, shifting the channels and altering the couplings for each scattering condition.

For solving the coupled differential equation 2.66 a numerical Numerov approach using a Fox-Goodwin propagator is used which is described in detail in the Doctoral Thesis of P. Kraus[37].

Here, only the used boundary conditions for the Fourier terms of the wavefunction $\Psi_{\mathbf{G}}$ will be given which are vanishing inside the crystal for z $\to -\infty$. For z $\to +\infty$, far away from the surface, closed channels decay exponentially whereas open channels form plane and propagating waves:

$$\Psi_{\mathbf{G}}(z \to -\infty) = 0 \tag{2.68}$$

$$\Psi_{\mathbf{G}}(z \to \infty) = \begin{cases} k^{-1/2}_{\mathbf{G},z} \mathrm{e}^{-\mathrm{i}k_{\mathbf{G},z}z}\delta_{\mathbf{G},\mathbf{0}} + k^{-1/2}_{\mathbf{G},z} S_{\mathbf{G}} \mathrm{e}^{\mathrm{i}k_{\mathbf{G},z}z}, & \text{if } \mathbf{k}^2_{\mathbf{G},z} > 0 \\ \kappa^{-1/2}_{\mathbf{G},z} S_{\mathbf{G}} \mathrm{e}^{-\kappa_{\mathbf{G},z}z}, & \text{if } \mathbf{k}^2_{\mathbf{G},z} < 0 \end{cases} \tag{2.69}$$

with $\kappa_{\mathbf{G},z} = \sqrt{-k^2_{\mathbf{G},z}}$.

The amplitudes $S_{\mathbf{G}}$ of the waves finally correspond to the measured intensities via $I_{\mathbf{G}} = |S_{\mathbf{G}}|^2$ and can be calculated by the numerical treatment mentioned above.

Debey- Waller Factor

The pure elastic Close-Coupling approach can not reproduce the temperature dependence of the scattering intensities. A simple way to consider the intensity-attenuation due to inelastic effects represents the Debye- Waller (DW)- factor W(T_S), following the relation

$$I(T_S) = I_0 e^{-2W(T_S)}. \tag{2.70}$$

This equation relates the intensity at zero temperature to the intensity at a sample temperature T_S, where $W(T_S)$ is given by

$$2W(T_s) \simeq \left\langle u_z^2 \right\rangle \cdot (\Delta k_z)^2. \tag{2.71}$$

This approximation holds for small angles and neglected parallel momentum transfer. $\langle u_z^2 \rangle$ is the averaged squared atomic displacement perpendicular to the surface and Δk_z is the momentum transfer perpendicular to the surface during the scattering event. Further, harmonic displacement of the atoms is assumed which gives, together with the Debye frequency, an expression for the DW- factor:

$$W(T_S) = \frac{3\hbar^2 T_S}{2M k_{\mathrm{B}} \Theta_D^2} \Delta k_z^2. \tag{2.72}$$

The applicability of the conventional DW-factor, which was originally introduced for X-ray diffraction [26], has been discussed extensively in theory as well as in experiments. In a paper of B. Gumhalter [46] the derivation and physical origin of the DW-Factor from different approaches is presented in detail. The issue of scattering from the electron density above the surface rather than at the ion cores is discussed in [47]. A. C. Levi [48] predicts an increase of diffraction intensities for soft potentials.
However, the DW- factor, as derived in equation 2.72, has been used successfully in several publications [1] [3] [6] [7]. The following section on the inelastic close coupling presents a way to avoid the inconsistency of the traditional DW- factor.

2.6.2 Inelastic Close Coupling

For the inelastic treatment of the close coupling method starting point is the time-dependent Schrödinger equation. Within this formulation, the time-dependent lattice vibrations will be taken into account- rendering the DW-factor unnecessary.

$$\mathrm{i}\hbar \frac{\partial \Psi(\mathbf{r}, t)}{\partial t} = \left[-\nabla^2 + V(\mathbf{r}, t) \right] \Psi(\mathbf{r}, t) \tag{2.73}$$

is the time-dependent Schrödinger equation for a structureless particle. The interaction potential $V(\mathbf{r}, t)$ has been introduced in section 2.5.2 for a dynamic lattice.
Expanding the wavefunction according to Blochs' theory and applying a periodicity in

time they can be written as

$$\Psi(\mathbf{r},t) \;=\; \mathrm{e}^{-\mathrm{i}\mathbf{k}_i^2 t/\hbar} \sum_{\mathbf{G},\mathbf{Q},\nu,n_{\mathbf{Q},\nu}} \Psi_{\mathbf{G}+\mathbf{Q},n_{\mathbf{Q},\nu}}(z)\cdot \mathrm{e}^{\mathrm{i}(\mathbf{K}_i+\mathbf{G}+\mathbf{Q})\cdot\mathbf{R}} \mathrm{e}^{\mathrm{i}n_{\mathbf{Q},\nu}\omega_\nu(\mathbf{Q})t}, \tag{2.74}$$

where n is the number of phonons with momentum Q in band ν equation 2.73 turns into a system coupled equations after multiplying both sides by $\exp(-\mathrm{i}(\mathbf{K}_i+\mathbf{G})\cdot\mathbf{R})$ and $\exp(-\mathrm{i}n\omega t)$ and integrating over time and the unit cell area:

$$\begin{aligned}
\left[\frac{\mathrm{d}^2}{\mathrm{d}z^2}+\mathbf{k}^2_{\mathrm{G},n,z}-V_{\mathbf{0}}(z)\right]\Psi_{\mathbf{G},n}(z) &= \sum_{\mathbf{G}\neq\mathbf{G}'} V_{\mathbf{G}-\mathbf{G}'}(z)\Psi_{\mathbf{G}',n}(z)\\
+\frac{1}{2}\mathbf{A}\cdot\sum_{\mathbf{G}'}\left[\mathbf{F}_{\mathbf{G}-\mathbf{G}'}(z)+\mathbf{F}_{\mathbf{G}-\mathbf{G}'}(z)\right]&\left[\Psi_{\mathbf{G}',n+1}(z)+\Psi_{\mathbf{G}',n-1}(z)\right],\\
\left[\frac{\mathrm{d}^2}{\mathrm{d}z^2}+\mathbf{k}^2_{\mathrm{G},n+1,z}-V_{\mathbf{0}}(z)\right]\Psi_{\mathbf{G},n+1}(z) &= \sum_{\mathbf{G}\neq\mathbf{G}'} V_{\mathbf{G}-\mathbf{G}'}(z)\Psi_{\mathbf{G}',n+1}(z)\\
+\frac{1}{2}\mathbf{A}\cdot\sum_{\mathbf{G}'}\left[\mathbf{F}_{\mathbf{G}-\mathbf{G}'}(z)+\mathbf{F}_{\mathbf{G}-\mathbf{G}'}(z)\right]&\left[\Psi_{\mathbf{G}',n+2}(z)+\Psi_{\mathbf{G}',n}(z)\right],
\end{aligned} \tag{2.75}$$

with

$$\mathbf{k}_{\mathbf{G},n,z} = \mathbf{k}_i^2-(\mathbf{K}_i+\mathbf{G})^2-n\hbar\omega \tag{2.76}$$

giving the energy of the particle after scattering perpendicular to the surface, and

$$\mathbf{F}_{\mathbf{G}-\mathbf{G}'}(z) = \left[\mathrm{i}(\mathbf{G}-\mathbf{G}')V_{\mathbf{G}-\mathbf{G}'}(z), V'_{\mathbf{G}-\mathbf{G}'}(z)\right] \tag{2.77}$$

giving the force components perpendicular and parallel to the surface.
The form of these equations is quite similar to the elastic case, described in section 2.6.1, extended with additional coupling factors. Again, a scattering channel is defined by the discrete asymptotic energy

$$(\mathbf{K}_i+\mathbf{G})^2+n\hbar\omega, \tag{2.78}$$

producing closed and open channels $|\mathbf{K}_i+\mathbf{G},n,\nu\rangle$ and $\left|\mathbf{K}_i+\mathbf{G},n,\mathbf{k}^2_{\mathbf{G},n,z}\right\rangle$. The elastic channels are, so to say, *dressed* by the phonon field. Assuming a number of phonons n, the potentials around n, considering annihilation (n-1) and creation (n+1), form a so called Floquet-block (at least three terms for single phonon events).
Looking at equations 2.75, the terms $\mathbf{A}(T)\cdot\mathbf{F}_{\mathbf{G}-\mathbf{G}'}(z)$ describe coupling within these blocks - interblock coupling- and $V_{\mathbf{G}-\mathbf{G}'}(z)$ enables intrablock coupling between different $\mathbf{G}$ vectors.

Besides considering only single phonon events, two more assumptions are made. First, the Rayleigh-curve is the only active mode, considered to be strictly shear vertical and following the Debye spectral density and secondly, the phonons do not carry any momentum and are therefore all located at the Γ - point.
These assumptions lead to an interblock-coupling where only the z-component is considered and the thermal displacement $A_z(T)$ can be estimated to

$$\mathbf{A}(T) \;=\; \frac{1}{aQ_c}\sqrt{\frac{384\hbar^2\pi T}{Mk_{\mathrm{B}}\Theta_D^2}}, \tag{2.79}$$

where Q_c is the Gaussian cut-off factor of the assumed harmonic movement.
This model has been implemented into a calculation of the diffraction intensities by P. Kraus and is described in detail in a paper on the interaction potential of the He-Bi(111) system[49].

2.7 Adsorption on solid surfaces

Atoms or molecules approaching a solid can interact with the surface in different ways. Besides the above well described elastic or inelastic scattering, one can distinguish two adsorptive processes: *Physisorption*, which originates from weak van der Waals forces, and the stronger *chemisorption*, which develops chemical bonds of covalent or ionic character. An indicator for adsorptive interaction is the residence time[50]

$$\tau = \tau_0 \cdot e^{\frac{E_{des}}{RT_s}} \tag{2.80}$$

of a particle on the surface. τ_0 is the vibration period of an adsorbed particle, T_s the surface temperature and E_{des} the energy gained upon desorption. For elastic and inelastic scattering τ turns out to be around 10^{-13} s to 10^{-12} s, whereas in case of chemisorption the residence time reaches $10^{-3} - 10^{3}$ s and more[51]. According to Tully[52], particles dissipating more than their thermal energy to the surface will be trapped at the surface.

Other important processes for understanding adsorption kinetics, adsorbate dynamics as well as two dimensional phase transitions of adsorbed layers and surface reactions are *desorption* and *diffusion* of adsorbates. When going beyond clean perfect surfaces and considering also the role of surface defects, as there are traps, vacancies, terraces or kinks, the field becomes very broad and complex. Eventually all these mechanisms are governed by the sum of the acting forces- their underlying potential conditions respectively.

As a matter of fact, at standard conditions (air, 1013 mbar and 300 K) all solid surfaces are covered with a monolayer of adsorbates. A monolayer (1 ML) is defined as 1 adsorbate atom or molecule for each 1x1 unit cell of substrate surface. When adsorption occurs, the energy of the particle-surface system is lowered and therefore an exothermic process. The amount of this energy is called the heat of adsorption ΔH_{ads}, which is always positive and corresponds to the particle/surface binding energy E_B. Coverage and heat of adsorption are experimentally accessible parameters. Widely used methods determining these quantities are desorption techniques, photoemission spectroscopy or Kelvin-Probe measurements. However, in this work the focus will be set on atom beam scattering as a method for revealing adsorbate characteristics.

2.7.1 Physisorption

The character and origin of the physisorption potential is described in section 2.5. The attractive $\sim -\frac{1}{z^3}$ behavior can be derived from treating the surface-approaching particle as an induced dipole Coulomb-interacting with its symmetric mirror charge inside the crystal[10]. This is, despite the similar origin, in contrast to molecular particle-particle van der Waals bonding where, the dipole fluctuations of one bonding partner induces an electric field at the site of the other and vice versa, resulting in a $\sim -\frac{1}{z^6}$ relation. Approaching closer to the surface, Pauli repulsion causes a steep rise of the potential. Typical physisorption potentials (see figure 2.10) have well depths in the meV region, where the minimum is positioned several Ångstrom above the solid. This leads to very high mobility of physisorbed adsorbates parallel to the surface. Hovever, physisorption will only occur at very low temperatures (compare $k_B T_{room} \approx 25$ meV) and when no chemisorption is present. For example[51] noble gas adsorption on metal surfaces usually occurs at temperatures lower than 70 K. The experimental determination of the averaged interaction potential of the He-Sb(111) system is presented in section 2.5.

2.7.2 Chemisorption

Chemisorption can be described similar to covalent bonds between atom or molecules. When an overlap between the valence orbital of the molecule or atom and a partially filled band of the solid is considered, the wavefunction for the adsorbate-solid system can be written as a linear combination of so called charge-transfer states, where one of the bonding partners is donating an electron to the orbital of the other partner. This wavefunction can then be used for minimizing the systems energy with respect to the Hamiltonian of the whole system. Finally the energy difference between the separated and the bonding system can be derived and also the chemisorption potential can be developed. The highest bonding energy is in the order of several eV located just a few Ångstroms above the solid. The bonding can be understood as an electron transfer from the Highest Occupied Molecular Orbital (HOMO) into an empty state at the surface or to the Lowest Unoccupied Molecular Orbital (LUMO) from a occupied surface state. A chemisorbed adsorbate therefore alters the electronic structure of the surface.
For molecules, this rearrangement of electronic orbitals can lead to so called *dissociative adsorption* (see figure 2.10). An example is the hydrogen molecule H_2 which will be discussed later. In the limit of very high heats of adsorption, chemical compounds as oxides or carbides may be formed.

2.7.3 Adsorption of Hydrogen

In this section the focus will be set on the adsorption of hydrogen molecules and atoms on surfaces. A brief overview on their physical properties will be given and their general behavior in terms of adsorption characteristics is summarized. A detailed treatment can be found in the review of K. Christmann[51].

The hydrogen molecule

The H_2 molecule has a very strong intramolecular covalent bond and is chemically more or less inert. It will develop mainly weak van der Waals- type interactions with a surface. For a chemical bond the energy positions of the highest occupied (ionization potential) and the lowest unoccupied (electron affinity) with respect to the surface bands would be most important. However, the molecule can dissociate when the bond formation energy with the surface exceeds the dissociation energy (436 kJ/mol).

Table 2.1: Properties of the hydrogen molecule.

Property	value	unit
mass	2	au
bond length	0.74	Å
binding energy	4.57	eV
first ionization energy	15.427	eV

The molecule has a very small electronic density of almost spherical shape and a large rotational constant which results in rather weak anisotropic forces acting on the molecule upon adsorption.
True physisorption of H_2 on metal surfaces is expected[53] to occur below 15 K, which means experiments will only be successful at liquid helium temperatures. Binding energies are in the range of 30-40 meV for noble metals[54] and little lower for simple metals[55].

The hydrogen atom

When the H_2 hydrogen molecule dissociates, the formed hydrogen atoms can chemisorb independently at the surface. Adsorption experiments have been carried out on many surfaces showing that H exhibits a high sticking coefficient especially on the transition metals[15].

Table 2.2: Properties of the hydrogen atom.

Property	value	unit
mass	1.008	au
atomic radius	25	pm
first ionization energy	13.59	eV
electron affinity	0.8	eV
electronegativity	2.20	Pauling

Due to its light mass hydrogen often shows its wave-like behavior, for example in tunneling, which influences H diffusion along surfaces resulting in abnormal kinetic behavior. The famous hydrogen bonding will effect H-containing molecules upon surface interaction. Adsorbed H atoms can even diffuse into the bulk (of Ti and Pd) forming for example TiH_2 where H is more densely packed than in solid hydrogen itself. Hydrogen very often forms stable hydrides with most of the metals. Either the H atom donates its single electron, leaving back a proton, or accepts an electron from the bonding partner, becoming a hydride ion H^-. This depends on the relative electronegativity of the bonding partners.

Chemisorption of Hydrogen

The H_2 molecule will usually dissociate at the surface before forming a chemical bond via the 1s- orbital with, for example, the partially filled d- band of a transition metal [51]. This dissociative adsorption can either be *non-activated* (spontaneous or direct) or *activated* (indirect), depending on the interaction potential shape. In the latter case, the potential develops a barrier between the physisorptive molecule state and the chemisorptive atom state higher than the asymptotic energy. This is visualized in figure 2.10. The effective potential can be seen as a superposition of the physisorption potential of the molecule-metal system and the chemisorptive potential of the 2-atoms-metal system. When there remains a repulsive barrier, the adsorbate has to overcome this activation energy E_{act} to finally adsorb dissociatively. If there is no barrier, the dissociation will be spontaneous and no activation energy is needed.
For the exothermic process (spontaneous), two times the hydrogen-metal bonding energy (E_{Me-H}) will be gained whereas the dissociation energy of the molecule (E_{diss}) has to

be spent. This leads to an expression for the adsorption energy (heat of adsorpiton E_{ad})

$$E_{ad} \;=\; 2E_{Me-H} - E_{diss} \tag{2.81}$$

which will be positive.
When the energy balance is negative, additional energy -the activation energy E_{act}- has to be provided which corresponds to activated or indirect adsorption. This has the consequence that for desorption this energy ads to the binding energy:

$$E_{des} \;=\; 2E_{Me-H} + E_{act} \tag{2.82}$$

Examples for both can be found in the paper of P. Ferrin et al.[15], where DFT calculations of H on different transition metal surfaces are presented. The majority of metals exhibit spontaneous adsorption, except from the noble metals Cu, Au and Ag, where activated dissociation is expected. Activated adsorption is often indicated by a very small sticking coefficient for molecular hydrogen and its temperature dependence.
The question now arises how the activation energy is provided during the adsorption process and how this influences the adsorption dynamics. In the review of Christmann[51] the process is described as follows: The H_2 molecule will approach the surface, feel van der Waals force and orientate parallel to the surface above a top site. It now is trapped in a precursor state and can move more or less freely along the surface with a slightly increased intermolecular bond length. Then it will move above a bridge site, where the activation energy is considerably lowered. At this point spontaneous adsorption will happen, if the metal-hydrogen bonding energy is high enough. If not, the energy necessary for dissociation can be implemented by vibrational excitation of the H_2 molecule via coupling of the molecular vibrations to surface phonons.
However, if the activation energy can not be mediated trough the surface, the H_2 molecule can be dissociated prior to adsorption using a source for atomic hydrogen as described in section 3.7.

2.7.4 Ordering and Phase transitions

Provided that the residence time for an adsorbate at the surface is long enough, the whole system will aspire towards thermal equilibrium amongst the adsorbates and the adsorbate-substrate system. For enabling ordering of adsorbates, diffusion along the surface has to be possible. This depends mainly on the surface diffusion activation

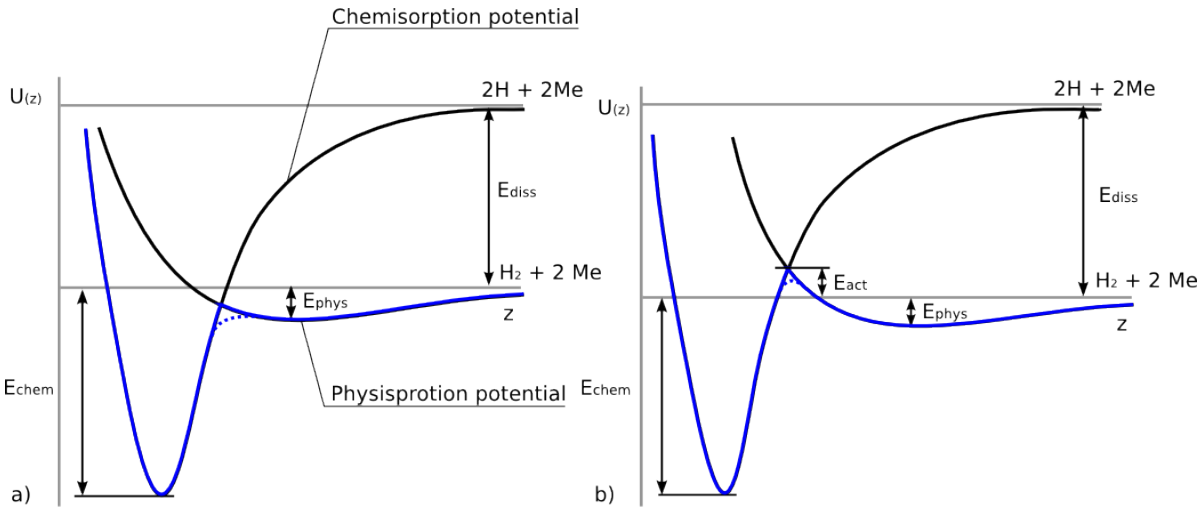

Figure 2.10: Dissociative adsorption can be illustrated by the superposition of a molecular physisorption and an atomic chemisorption potential. Spontaneous dissociation is shown in (a), whereas in (b) an activation energy is necessary for activated dissociative adsorption.

energy (which is of the order of the adsorption well depth), describing the hopping of the adsorbates between surface sites. Ordering therefore is temperature dependent; both too high or too low surface temperature will suppress ordering processes.
From the adsorbates' point of view, there are parallel and perpendicular forces acting. The latter ones correspond to the binding energy with the surfaces whereas the former are responsible for the surface site on which the adsorbate eventually comes to rest. The lateral adsorbate-adsorbate interactions can be repulsive or attractive and are decisive for the formation of any ordered overlayer. They are, however, strongly dependent on distance and therefore coverage. Also the adsorbates can change the underlying substrate which leads to surface-mediated interactions. As the perpendicular binding forces already have been discussed above, here the physical origin of the lateral forces will be mentioned briefly:

- van der Waals attraction
- Orbital overlap
- Permanent dipole moment of adsorbed molecules
- Substrate mediated interactions

The ordering is most of all a question of the relative strength of the vertical and the lateral forces. In the pyhsisorptive case of weak binding energies, the ordering won't fol-

low the sites of the underlying substrate and form an overlayer with independent lattice constant (incommensurate overlayer, figure 2.2). Chemisorbed overlayers on the other hand interact much stronger with the substrate and even alter the adsorption sites. A chemisorbed overlayer is controlled by the substrate (commensurate overlayer, figure 2.2) and the chosen adsorption sites are independent from the other adsorbates up to certain coverage. Often the adsorption site with the highest number of substrate neighbors is then chosen. Examples for forming physisorptive overlayers are noble gases on metals, whereas oxygen or sulfur for example chemisorb on metal surfaces. However, also intermediate states exist and the systems are in general strongly dependent on the surface temperature and coverage. An example in the low coverage regime is the formation of either a 2D gas phase of randomly distributed adsorbates, or the formation of crystalline islands (2D liquid droplets). Temperature change can cause a phase transition between these two cases.
Especially physisorbed adsorbates can phenomenologically be imagined as a 2D gas that undergoes phase transitions into a liquid or solid phase, depending on coverage and temperature. Surprisingly, this also works for chemisorbed adsorbates, where the perpendicular binding forces with the surface are not considered explicitly, but only keeping the two dimensional system in place. Using HAS, critical parameters of phase transitions can be measured and used to determine interaction forces of the adsorption systems.

A considerable way to describe such a system is rewriting the van der Waals equation for a non-ideal fluid with temperature T and pressure p in the liquid-vapor regime

$$(p + an^2)(1 - nb) \;=\; nk_BT \tag{2.83}$$

into an equation for a two dimensional adsorption system

$$(\pi + \frac{a\theta^2}{d})(\frac{1}{\theta} - f_p) \;=\; k_BT \tag{2.84}$$

using

$$nd = \theta, \quad b = df_p \;\; and \;\; \pi = dp \; . \tag{2.85}$$

Here a considers the attraction between particles and b their occupied volume. The volume particle density is denoted as n (n = N/V), d is the thickness of the quasi 2D-system (1-3 Å). θ becomes the area particle density and f_p is the area occupied by a particle. Often the relative coverage $\theta_r = \theta/\theta_0$ is used. π is the so called splay-pressure

which describes the force onto a line element under a certain pressure. Plotting splay pressure or temperature above the reciprocal density gives 2D-phase diagrams, where a liquid, gas and a liquid-gas-coexisting phase can be distinguished. Also order-disorder transitions of chemisorbed adsorbates forming crystallites and ordered monolayers, as for example H on Ni(111), which forms a (2x2) superstructure, exhibit a behavior following the simple van der Waals relation. The critical parameters where phase transitions occur can be found by finding the roots of the cubic equation 2.84. One ends up with [10]

$$\theta_c = \frac{1}{3f_p} \quad \pi_c = \frac{a}{27df_p^2}, \quad and \quad T_c = \frac{8}{27}\frac{a}{k_B df_p} \ . \tag{2.86}$$

The critical parameters can be found experimentally via LEED or HAS measurements and also phase diagrams can be obtained. The parameter f_p contains information on the adsorbate-distance and a gives insight into the interaction energy between particles. However, chemisorption systems exhibit phase diagrams of much higher complexity and often several ordered phase transitions. This originates from the much stronger ionic or covalent bonding to the surface which enhances substrate mediated interactions between the adatoms.
Interestingly, the lattice gas problem can be described with statistical mechanics by dividing the surface into N identical square cells and introducing a occupation variable for the cells. Referring an energy gain to any cell and adding an interaction energy combined with occupied sites, one can find an expression for the total energy of the system [13]. This problem can be treated with Monte-Carlo simulations and corresponds exactly to the spin 1/2 Ising- model where the coverage can be related to the magnetization. This model expanded to a many body problem can reproduce behavior like domain growing and critical parameter connected with phase transitions.

Lots of information about the ordered structure, the occupied adsorption sites and the mutual forces between the adsorbates can also be gathered from inelastic measurements using HAS. The collective vibrations of the adsorbates of a ordered structure develop certain modes with considerable dispersion that can be revealed by inelastic HAS. If the dispersion is flat, the adsorbate-adsorbate interactions are weak and the energy loss corresponds to the vibration modes of the adsorbed particle. Any contamination of a clean substrate is visible in the HAS-signal. This is further discussed in section 2.8 .

2.7.5 Surface diffusion

Also surface diffusion will be mentioned here briefly to complete the mechanisms of surface dynamics. Diffusion influences the kinetics of adsorption and desorption processes as well as phase transitions and plays an important role for example in high quality semiconductor crystal growth.
A particle in a physisorbed or bound precursor state only feels a weakly corrugated potential several Ångstroms above the surface. For that reason it will exhibit conventional kinetic behavior governed by particle-particle interactions and coverage. A chemisorbed particle in contrast, which is bound deep in a periodically repeated adsorption well, can only hop from one adsorption site to the next when overcoming a certain energy barrier E_d or activation energy respectively. This barrier depends on the modulation of the chemisorption energy along the corrugated electron density above the surface. The particles' motion can be considered discrete, completely random and uncorrelated from jump to jump as there is no a priori bias to favor a particular direction leading to a random walk motion. When P(x,y,t) is the probability to find a particle at lattice site (x,y) at time t, one can find [13]

$$\frac{dP}{dt} = D\nabla^2 P, \tag{2.87}$$

which corresponds to Fick's second law of diffusion where D is the diffusion constant. For diffusion in presence of other particles in surface reactions or phase transitions one should stick to another representation of Fick's law

$$\frac{dn}{dt} = D_C\nabla^2 n \ , \tag{2.88}$$

where n(r) is the adsorbate particle density n(r) at a finite coverage and D_C is the chemical diffusion constant. The jumping rate is proportional to thermal fluctuations around the activation barrier which makes the hopping frequency ($\nu(T)$) as well as the diffusion coefficient $D_C(T)$ proportional to a Boltzmann- factor depending on surface temperature T_S

$$\nu(T) = \nu_0 exp(-E_d/k_B T_s) \text{ and } D(T) = D_0 exp(-E_d/k_B T_s) \ . \tag{2.89}$$

This Arrhenius- behavior is accessible for example by HAS measurements by determining D at different surface temperatures. This method is briefly described in section 2.8.4.
In case of hydrogen at very low temperature, the movement is governed by tunneling, which makes the diffusion coefficient independent from surface temperature as shown for

H on W(110)[56].
Surface diffusion can theoretically be studied with surface dynamics or Monte Carlo simulations which both require a reasonable adsorbate-substrate interaction potential.

2.7.6 Electronic structure/Work function change

The electronic structure plays an important role in surface reconstruction. As adsorption is often connected with shifting or transfer of charge carriers, it will considerably alter the electronic conditions. A measure for this impact is the change of workfunction induced by the adsorbates. The workfunction $e\phi$ is the energy needed to raise an electron from the Fermi level (E_F) inside the bulk cross the surface to the vacuum level (E_{vac}) and consequently out of the material. The surface contribution to the workfunction rises from an electrostatic dipole barrier resulting from electronic surface states. Different surfaces of the same crystal have different electronic structures and therefore different workfunctions. Rough surfaces exhibit smaller workfunctions and generally in the range of some eV. Any electronic change of the surface -resulting from a changes in the density of states at the Fermi level- can be recognized by measuring the work function change, for example via photoemission spectroscopy.
The shifted charges at the surface, especially due to chemisorption, induce or alter the dipole-layer which consequently changes the work function of the surface. Hydrogen as an adsorbate settles very close to the surface and its single electron is easily screened which makes workfunction changes rather small. More on this complex topic can be found in the review of K. Christmann[51] or in relevant books[10] [13].

2.7.7 Adsorpion kinetics/desorption process

For describing adsorption kinetics and interpreting experiments quantitatively, a phenomenological thermodynamic approach is used. The argumentation is following mainly chapter 10.5 of the book on solid surfaces of H. Lüth[10]. In this work only the basic considerations will be presented for completeness as the analysis of the experimental data is focusing on structural changes.
The impingement rate (flux I) of gas particles of mass m at a certain pressure p and temperature T on a surface (per unit area and time) is

$$I = \frac{dN}{dt} = \frac{p}{\sqrt{2\pi mkT}} . \tag{2.90}$$

The sticking coefficient S is determined by the fraction of adsorbed atoms, so the adsorption rate becomes

$$r_{ads} \;=\; S \cdot I \;=\; S\frac{p}{\sqrt{2\pi mkT}} \;. \tag{2.91}$$

An integral over the time the surface is exposed to the gas then gives the coverage θ

$$\theta \;=\; \int r_{ads}\; dt \;=\; \int S\frac{dN}{dt}dt \;. \tag{2.92}$$

From equation 2.91 and 2.92 the sticking coefficient can be expressed as

$$S \;=\; \sqrt{2\pi mkT}\frac{u}{p} \;=\; \sqrt{2\pi mkT}\frac{1}{p}\frac{d\theta}{dt} \;. \tag{2.93}$$

This equation opens up a possibility to determine the sticking coefficient S from measuring the dependency of coverage θ on exposure (dosage). Exposure is simply pressure times time and is often expressed in L (Langmuir)

$$1\text{ L} \;=\; 1\text{ Torr} \cdot \mu\text{s} \;\approx\; 133\text{ Pa} \cdot 10^{-6}\text{ s} \;=\; 1,33 \cdot 10^{-6}\text{ mbar} \cdot \text{s} \tag{2.94}$$

When the sticking coefficient S = 1, L = 1 corresponds approximately to a coverage of 1 ML (monolayer).
The coverage can experimentally be derived from thermal desorption experiments[57,58]. In HAS, there is also a strong dependency of the intensity of the specular beam on adsorbates and coverage respectively, which also can be exploited as further described in section 2.8. Usually the relative coverage is used, which is defined as $\theta = \frac{n}{n_0}$, the ratio of adsorbed particles n to the number of adsorption sites on the surface n_0.
The sticking coefficient must be a function of the coverage and is dependent on the adsorption type which can be argued by several points.

- With increasing coverage, the number of available adsorption sites decreases. Also the diffusion path for precursor mediated adsorption becomes longer and the sticking probability will become lower.
- For activated adsorption, the incoming particle needs to overcome at least the activation energy E_{act}. This results in a Boltzmann factor $exp(-E_{act}/kT)$.
- Concerning chemisorption, the overlap of the electronic orbitals of surface and adsorbate is important. This leads to a local dependency on the surface structure and an orientation dependency of the incoming particle.

- Inelastic effects, emerging from interaction with phonons or plasmons, will cause energy transfer to or from the incoming particle influencing the adsorption kinetics. For adsorption the particle must dissipate some of its kinetic energy to the surface otherwise it will be desorbed within a vibrational period.

These considerations lead to an expression for the sticking coefficient

$$S(\theta) \;=\; \sigma f(\theta) e^{-E_{act}/k_B T}. \tag{2.95}$$

Here, f(θ) describes the behavior of the sticking coefficient depending on the coverage. The Langmuir adsorption model assumes that the adsorption is limited to one monolayer coverage, that all adsorption sites are equivalent and only one particle can reside in an adsorption site. For non-dissociative adsorption this gives simply

$$f(\theta) \;=\; 1 - \theta. \tag{2.96}$$

If the adsorbate is a dissociative diatomic molecule adsorbing immobile, the number of empty states in the neighboring of the first adsorbate is reduced, so the expression becomes

$$f(\theta) \;=\; \frac{z}{z-\theta}(1-\theta)^2, \tag{2.97}$$

where z is the maximum number of nearest adsorption sites for the second adsorbate. For mobile adsorbates and low coverage this gives

$$f(\theta) \;\simeq\; (1-\theta)^2. \tag{2.98}$$

as there is no restriction to the possible adsorption sites anymore.
In equation 2.95, σ is the so called condensation coefficient containing inelastic effects as well as the molecular orientation and mobility. This factor can be treated from a statistical point of view. The whole adsorption process can be considered as a transition from an initial state of free surface and free molecule (S+M) via an excited state (SM)* (including the activation energy) into a final state (SM). σ is then proportional to the ratio of $Z_{(SM)^*}/(Z_M \cdot Z_S)$, where Z is the partition function of each state. This requires a complicated quantum mechanical treatment and will not be further discussed. It should only be stated here, that for mobile adsorbates not loosing rotational freedom σ just gives unity, which is often the case for hydrogen adsorption (except for hydrides).
For desorption, the particle has to overcome the binding energy E_B and the activation

energy E_{act} resulting in $E_{des} = E_B + E_{act}$. The adsorption rate becomes

$$r_{des} = \overline{\sigma}\overline{f}(\theta)e^{-E_{des}/k_BT} , \tag{2.99}$$

where $\overline{f}(\theta)$ is the occupation factor and $\overline{\sigma}$ the desorption coefficient. These factors are complementary to the equivalent coefficients for adsorption, resulting for example in $\overline{f}(\theta) = \theta$ for single desorption.
Assuming the whole system in thermal equilibrium the adsorption and the desorption rate must be equal: $r_{ads} = r_{des}$. This leads to the so called Langmuir isotherms when single adsorption is assumed.

$$p(\theta) = \frac{\theta}{A(1-\theta)} , \quad \theta(p) = \frac{Ap}{1+Ap} \tag{2.100}$$

Here, $1/A = \frac{\overline{\sigma}}{\sigma}\sqrt{2\pi mkT}e^{-E_B/kT}$ is constant at a fixed temperature and can be derived from measuring the coverage θ as a function of ambient pressure p. So, if the condensation and desorption coefficients (σ and $\overline{\sigma}$) are known, the binding energy E_B of the adsorbate can be determined.
The simple Langmuir assumption does not provide the correct behavior for many realistic systems. Other models, as for example the BET isotherm (Brunauer, Emmett and Teller) also take into account multilayer adsorption which yields better results for more complicated systems.

2.8 Helium atom scattering from adsorbate-substrate systems

HAS is exceptionally well suited for the investigation of adsorbate systems: From observing single, randomly distributed adatoms at low coverages to the analysis of ordered overlayer superstructures. In the following sections different applications of the method revealing information on adsorbate structures will be presented based on the underlying interaction. Roughly, the range of applications of HAS on adsorption systems can be separated into two fields:

- **High coverage, ordered structures:**
  ⇒ Use straightforward *diffraction analysis*.
- **Low coverage regime, disordered distribution of adsorbates:**
  ⇒ Observe attenuation and width of *specular peak*.

The method can be used to examine a range of effects and processes connected with surfaces and adsorbates, as for example crystal growth, ordering transitions of adsorbates and adsorbate diffusion. When the experimental setup is adequate, these studies can be carried out at a high sensitivity, in situ and at different temperatures.
A problem however is the conversion of a particular adsorbate exposure into a substrate coverage, which depends on the sticking coefficient. This can only be achieved by additional thermal desorption spectroscopy (PTDS) results for the particular system. Also the method is not material specific, which makes complementary AES analysis of the surface necessary to exclude the possibility of undesired contamination.

2.8.1 Elastic coherent scattering from adsorbed monolayers

The mechanism of elastic diffraction from a two dimensional ordered array of atoms is discussed in section 2.4.2. The relation between the occurring intensities of the diffraction peaks and the corrugation of the electronic density distribution at the surface is treated quantum mechanically in section 2.6. These models can be applied straightforward onto ordered adlayers which replace or alter the clean termination layer of a substrate crystal. After exposing the clean substrate to the adsorbate gas, an angular diffraction scan as described in section 2.4.2 can simply be compared with a scan from a clean structure. Additional or altered diffraction peaks may occur and shed light into the adsorption system of interest. It is possible to verify the adsorbate structure and the adsorbate's

influence on the electronic conditions of the surface.
An example is the H/NiAl(110) system, where D. Farías et al. presented[59] two different H phases at a sample temperature of 90 K using HAS. The low coverage c(2x2) structure obeys the same shallow electronic corrugation as the clean NiAl(110) surface of 0.035 Å. Delocalized electrons at the surface might contribute to this unusual fact. The (1x1) saturation phase in contrast shows a strong increase of the corrugation (0.22 Å). An interesting study is also given by Ch. Wöll[60] who investigated a number of metal oxides with respect to H adsorption. Another example can be found in a paper of R. Apel et al[61]. , where H adsorption on Rh(311) is discussed using a He and a Ne atom beam. However, the strong corrugation of the Sb(111) surface (section 4.1) reinforces coherent scattering which probably complicates the elastic spectrum.

2.8.2 The cross section for diffusive scattering from adsorbates

The extreme sensitivity on the presence of adsorbates and defects of HAS (down to 0.001 ML[26]) can be explained by the large cross section for diffuse scattering introduced by B. Poelsema and G. Comsa[28]. By simply monitoring the dependence of the specular peak intensity (purely elastic, $\theta_i = \theta_f$) of the He-beam on adsorbate-coverage ($\Rightarrow$ the *adsorption curve* $I/I_0(\Theta)$), the lateral distribution of the adsorbates as well as their mutual interaction can be deduced.

To understand the nature and origin of this cross section one first has to consider the influence of a single adsorbate on a surface on the interaction potential introduced in section 2.5. First, the approaching He atom feels the adsorbate already from a larger distance because of dispersion forces resulting in a modification of the attractive part of the potential. And secondly, the repulsive potential will be altered locally creating a hill or a hollow in the electronic density distribution at the surface, depending on the binding mechanism. The former effect plays a major role at low coverage, leading to elastic diffuse scattering (at a low solid angle), whereas the latter is important at high coverage, when periodic superstructures develop, contributing to coherent intensity. Both influences attenuate the specular intensity, as indicated in figure 2.11 .
Also inelastic contributions from the vibrating lattice have to be taken into account which are commonly described by a Debye-Waller-factor, as mentioned in section 2.6.1. In addition to the surface phonon modes, the incoming He atom can now also interact with internal modes of the adsorbate and vibrations of the adsorbate-substrate bond. Momentum exchange leads to scattering into a wide solid angle and therefore atten-

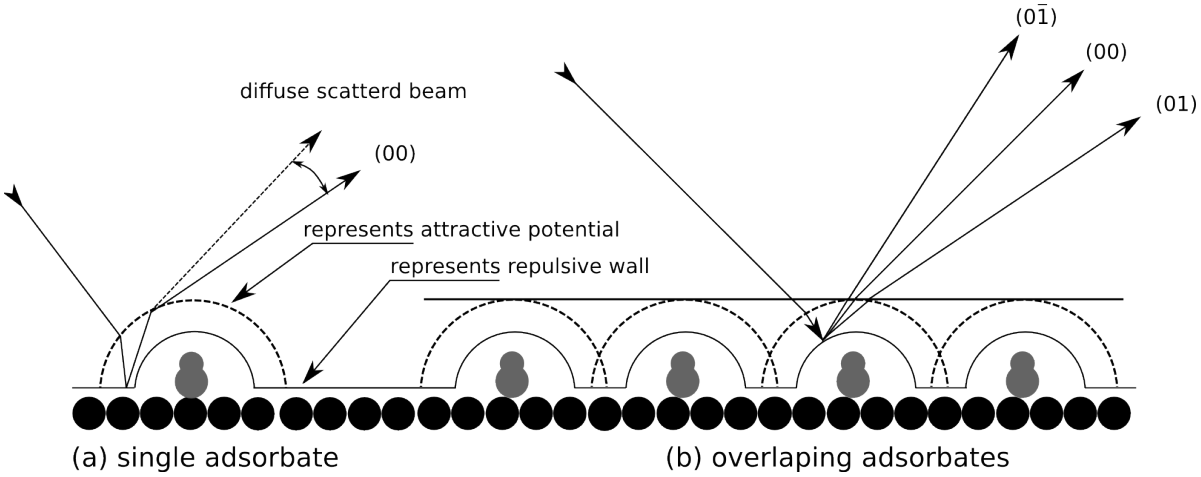

Figure 2.11: Illustration of the mechanism of diffuse elastic scattering from a single adsorbate (a). An incoming He-atom will be deflected by the modified attractive potential induced by the adsorbate. This leads to a small angle deviation compared to the specular peak from the uncovered surface. In (b) the geometrical overlap of scattering cross sections is shown. In case of a ordered superstructure this can lead to the development of coherent diffraction.

uation of the specular intensity. In that sense two different adsorbate species can be distinguished: There are diffuse scatterers, where the inelastic attenuation is very efficient and the specular intensity almost vanishes at total coverage (e.g. CO on Pt(111)). And there are "mirror like" adsorbates (eg. Pt on Pt or H on metals), where the specular intensity is restored more or less after adsorbing a full monolayer. In this case, also interference effects, similar to scattering from terraces, have to be considered. This leads to two different characteristic adsorption curves which in principle are illustrated in figure 2.12 a. Also it is necessary to mention that the presence of whatever adsorbate does not effect the specular peak profile[62].

At least for very flat and non-corrugated surfaces, where the specular peak is the only coherent contribution, diffuse and coherent scattering can be viewed as complementary phenomena. So the attenuation of the relative specular peak height directly represents the probability for diffuse scattering. In case of low coverage and no adsorbate-adsorbate interaction, a linear dependence of the intensity on the coverage can be assumed. The diffuse scattering cross section Σ is then defined as

$$1 - I/I_0 \;=\; n\Sigma \;=\; \Theta n_S \Sigma \;, \tag{2.101}$$

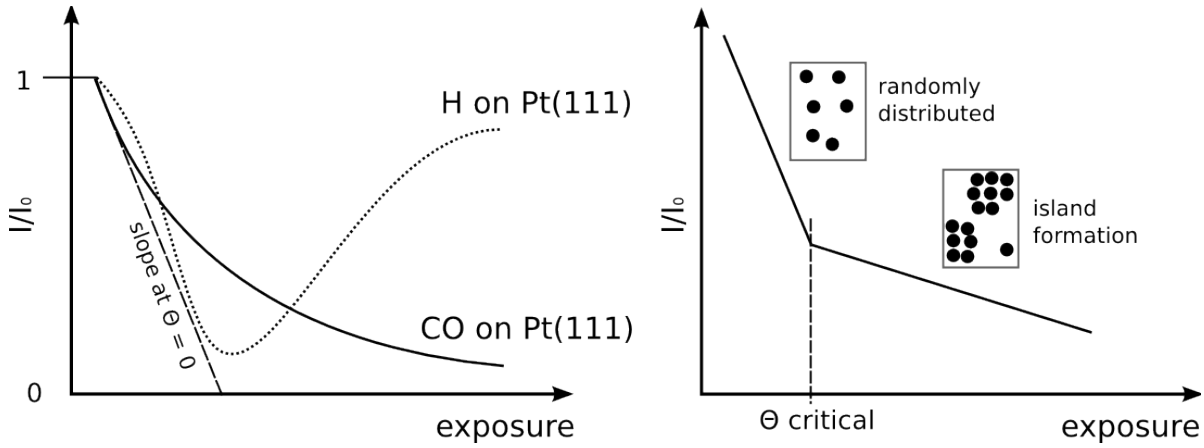

Figure 2.12: Attenuation of specular peak intensity with increasing adsorbate coverage. Principle adsorption curve behavior of diffuse and mirror-like adsorbates (a). Qualitative specular beam attenuation in case of a 2D gas-solid phase transition, as adapted from [63]

where n/n_S is the number of atoms per unit cell for the adsorbate/substrate per unit cell. This can be rewritten more general as

$$\Sigma \;=\; -\frac{1}{n_S} \cdot \frac{d(I/I_0)}{d\Theta} \mid_{\Theta=0} \quad . \tag{2.102}$$

From this equation the scattering cross section Σ can be determined. For CO on Pt(111), Σ has been determined [64] to 123 Å^2. Also in the paper of B. Poelsema et al., the similarity between gas phase scattering and the surface scattering from diffuse scatterers is shown.

For highly corrugated surfaces, as for example the Sb(111) or the Bi(111) surface, also the coherent contributions have to be considered and the above described simple approach will not be sufficient. This is discussed in a paper of G. Armand et al. [65], where K adsorption on Cu(115) is treated experimentally and theoretically.

A more recent and modern demonstration of HAS used on the low coverage CO/Pt(111) system is given by B.H. Choi et al. [66], where a realistic potential for He-CO system is derived from close coupling calculations.

2.8.3 Low coverage lateral distribution of adsorbates

When the scatterers are perfectly diffuse and the specular intensity results only from non-covered areas, the relationship between the He intensity and the adsorbate coverage can be given:

$$I/I_0 \;=\; (1-\Theta)^{\Sigma \cdot n_S} \tag{2.103}$$

This is called the lattice-gas formula, which follows a strict geometrical overlap approach of the scattering cross sections and assumes no interaction between the adsorbates. But already from this simple relation lots of systems can be described well. The equation is the surface scattering equivalent to the gas phase scattering equation, the Lambert-Beer law.
HAS can be used to exploit the dependency of the attenuation of a coherently scattered He beam on the lateral adsorbate distribution.
When there are attractive or repulsive forces present in between the adatoms, the adsorption curve will deviate from equation 2.103. The lattice gas formula can be adapted by assuming no geometrical overlap of the scattering cross sections in the repulsive case, and island formation in the attractive case. This is illustrated in figure 2.13 . An example for repulsive interactions would be the CO/Pt(111) system, whereas Xe atoms on Pt(111) attract each other[28]. Especially for physisorbed noble gases on metals, behaving similar to a 2D gas on a lattice (see section 2.7.4), also phase transitions can easily be detected because of the altered mutual forces resulting in a different adsorption curve behavior (see figure 2.12 b). This has been demonstrated for the first time by B. Poelsema et al.[67] for the 2D Xe gas-solid phase transition on Pt(111). From critical parameters, like the critical coverage, properties as for example the interaction energy between the adsorbates can be derived. K. Kern et al.[63] derived lateral interaction energies for the 2D lattice gas of Xe (43 meV), Kr (26 meV) and Ar (17 meV) on a Pt(111) surface from the critical coverage for phase transitions.

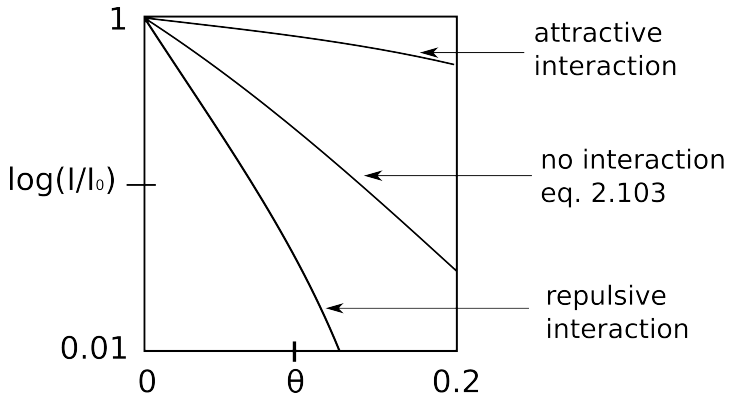

Figure 2.13: Specular peak attenuation depending on coverage for different adsorbate species obeying repulsive, attractive or no mutual interaction.

2.8.4 Quasielastic scattering from diffusing adsorbates

The term *quasielastic* refers to the interaction of an atom beam with diffusing particles on a surface. The motion of the adatoms leads to a broadening of the reflected energy distribution compared to the distribution of the incoming beam. This broadening is induced by small energy transfers (somewhat inelastic!) from a Doppler shift due to the diffusive motion of the adatoms. Consequently the specular peak is broadened in a Lorentzian shape which is depending on the diffusion conditions. Using HAS, the energetic broadening of the He atoms is measured as a function of momentum transfer and temperature.
The energy and intensity distribution resulting from quasielastic scattering on a flat surface with low coverage is well described by J.W.M. Frenken and B.J. Hinch[68]. The theory allows to apply different diffusion models and to derive diffusion parameters like the activation energy or the pre-exponential factor. An example for an investigated system is H and D on the Pt(111) surface[69]. The authors report a single jump mechanism with an activation energy of $E_{act} = 68$ meV and a prefactor of $D_0 = 1.1\text{x}10^{-3}$ cm^2s^{-1} which signify extremely mobile hydrogen atoms in the low coverage regime.

2.8.5 Inelastic scattering from adsorbates

In section 2.3.2, the influence of adsorbed particles on a surface lattice is discussed. The surface phonon dispersion relation will be altered compared to a clean structure due to electronic changes and/or the influence of the additional mass. This alteration can be measured using inelastic HAS[23]. Oxygen on Pt leads to a surface phonon mode damping[24] whereas H on Pt surprisingly restores the bulk phonon conditions.

Also the internal vibrations of single adsorbed molecules on a surface are accessible by elastic and inelastic high resolution HAS measurements as e.g. demonstrated for CO on Pt(111) by B.H. Choi et al.[66] [70]. In the elastic spectrum the specular peak from the flat Pt(111) surface dominates, but there are features of interference structures from single molecules visible. Also peaks due to coherent diffraction from the lattice gas of CO molecules appear. The lowest vibration mode of the CO molecules can be detected in TOF measurments even the intensity is 10 to 10^4 orders lower as the elastic peak. This mode (T- mode = 5.9 meV) is dispersionless over the whole range of possible momentum transfer.
However, for the H/Sb(111) system it is not likely to observe internal vibrational modes

as they are expected at much higher energies due to the short bond and the low hydrogen nuclear mass.

3 Experimental

This chapter deals with the experimental set-up of the HAS-apparatus H.A.N.S (Helium Atom Nondestructive Scattering) on which all experiments have been carried out. A very detailed description of the apparatus as well as calibration measurements on a LiF sample can be found in several publications[71,31,1], whereas in this work only a summary on the construction and all necessary technical data for analysis is provided. Also the newly installed hydrogen source will be introduced and described.

3.1 Description of the apparatus

The apparatus is made up of three separately pumped vacuum chambers each providing the conditions for the chambers' purpose. The helium atom beam is created in the source chamber, scattering takes place in the main chamber and then the beam will be detected in the detector arm (see figure 3.1). In the source chamber and the detector arm at least high vacuum conditions are required to provide the appropriate mean free path for supersonic expansion and beam propagation. In the main chamber, where the sample is positioned, ultra high vacuum is needed to avoid undesired coverage of the sample surface by residual gas atoms within the timescales of the experiment.
A turnable manipulator enables angular intensity scans. The fixed source-detector angle of 91.5° of the apparatus leads to a so called moving threshold scattering geometry. Also it is possible to carry out time-of-flight (TOF) measurements for detecting energy transfer between beam and sample.

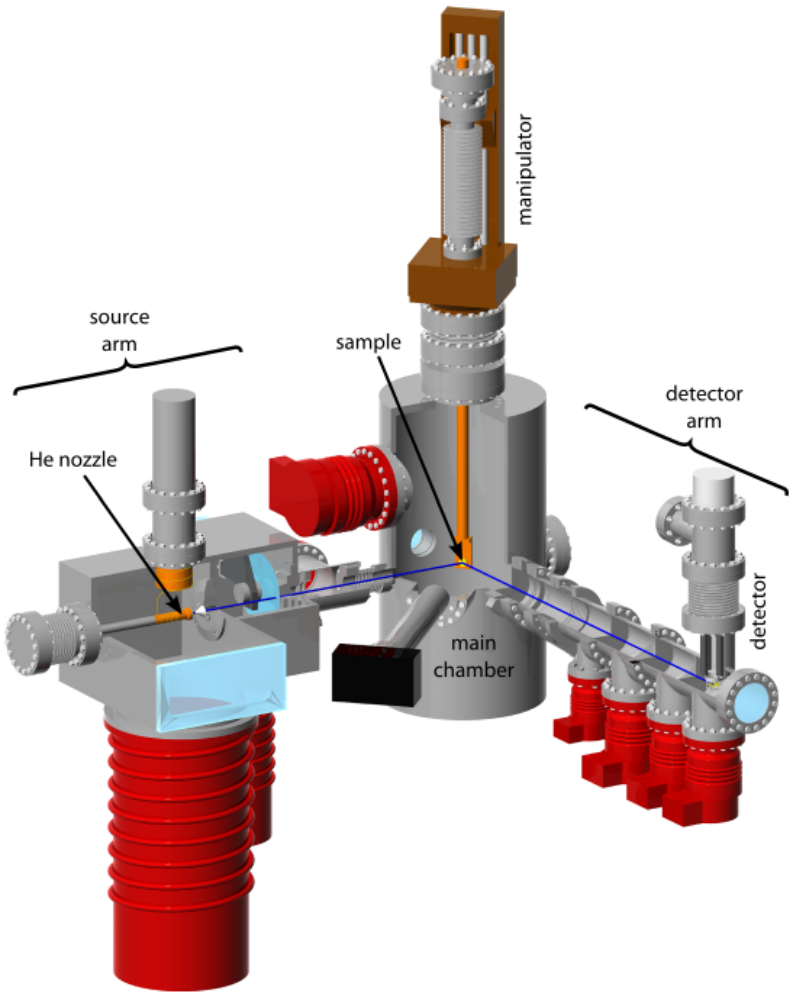

Figure 3.1: CAD- model of the H.A.N.S apparatus, taken from[31]. The beam propagation is marked by the blue line. The beam of He atoms is produced in the beam chamber, interacts with the sample in the main chamber and is finally detected in the detector arm.

3.2 Beam creation

The key to satisfying atom scattering experiments at high resolution is a well collimated atom beam providing a narrow velocity distribution. Both can be realized by an adiabatic supersonic expansion of the probing gas through a tiny nozzle (10 μm diameter).
Inside the first stage of the source chamber ($p_a < 10^{-6}$ mbar), the cooled He-nozzle ($T_0 =$ 60 K - 135 K) is supplied with high-purity He-gas at high pressure ($p_0 \sim 50$ bar). Due to the large pressure difference the gas is expanding very fast and adiabatically leading to a transformation of the particle's thermal energy into translational energy[72,73]. The final particle velocity can be derived from thermodynamics of an ideal gas and conservation of energy according to the book of H. Pauly[74] leading to

$$v \approx \sqrt{\frac{5 \cdot k_B \cdot T_0}{m_{He}}} \ , \tag{3.1}$$

where k_B is Boltzmann's constant and m_{He} the atomic mass of helium.
Afterwards a skimmer with a diameter of 310 μm is selecting the central part of the beam cross section ending up with a velocity distribution of roughly $\Delta v_{\parallel}/v_{\parallel} \approx 1\%$.
From 3.1 the relevant quantities for describing scattering events can easily be obtained when using the concept of de Broglie waves. The beam energy reads as

$$E_i = \frac{5}{2} k_B T_0 \ , \tag{3.2}$$

and the wavevector of the particle beam can be expressed as

$$\mathbf{k}_i^2 = \frac{2 m_{He}}{\hbar^2} E_i \ . \tag{3.3}$$

The temperature of the nozzle is adjusted using a cold head (working according to the Gifford McMahon-process), a Pt100 thermometer and resistive heating. This enables a energy range of the probing He-beam of 13 meV to 35 meV.

3.2.1 Beam chamber modifications

Due to an error of the cold head in use (Leybold, RGD 510) an available alternative cold head had to be installed. The new one (Leybold, RGD 1245) has more power and is larger in size which made some modifications in and around the beam chamber necessary. The original set-up is described in principle in the Master Thesis of N. Balak[71]. Most of the adaption parts, like a copper pre-cooling coil for the He gas, a cylindrical copper

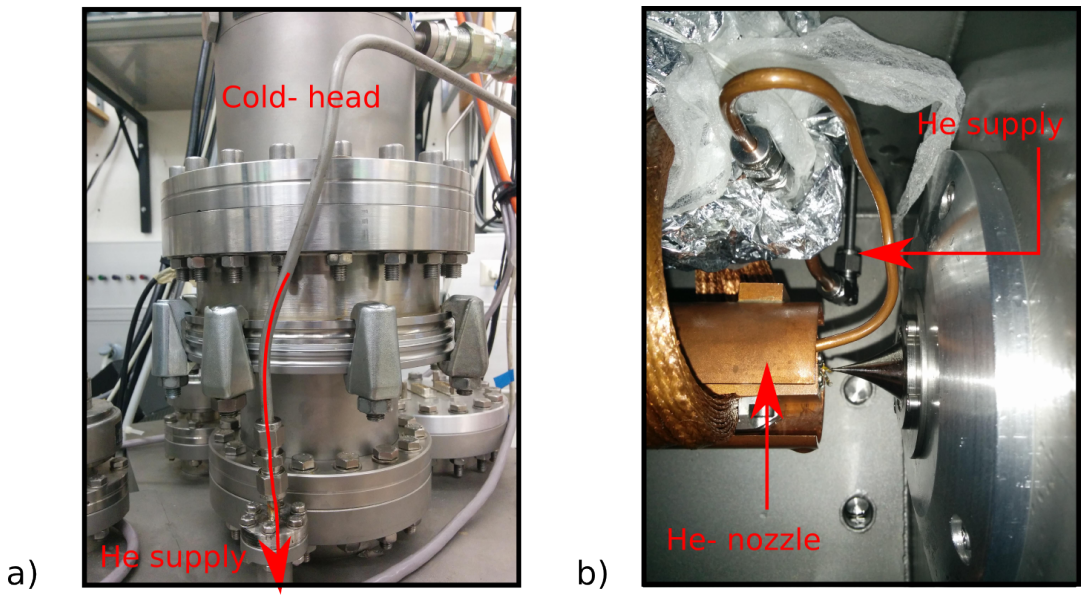

Figure 3.2: Outside (a) and inside (b) of the modified beam chamber with marked He-supply.

piece for adapting the changed cold head position and an adaption flange have been available and simply needed to be installed.
The He-supply pipe for the nozzle had to be rearranged. It is now fed through a flange directly into the beam chamber instead through a connection at the cold head. This also means the pipeline had to be guided differently and now leads from the feed-through at the chamber top to the pre- cooling coil and finally to the nozzle.

3.3 Main chamber and manipulator

The scattering events take place in the main chamber where the sample is mounted on a seven-axis manipulator crossing the He-beam. Rotating the manipulator makes angular scans (Θ_i) for diffraction experiments possible at a resolution of 0.1°. Besides positioning and aligning, the sample can also be cooled using liquid nitrogen down to 110 K or heated up to 450 K via a button heater, while the temperature is measured by a type K thermocouple.
The chamber must provide UHV conditions to avoid contamination of the sample surface and can be pumped down to a pressure of 10^{-11} mbar. A residual gas mass spectrometer is attached to ensure the necessary vacuum conditions. The sample can be cleaned using a Ar^+-Ion-gun for sputtering and subsequent annealing by a button heater mounted at

the sample holder. For checking surface contamination and crystal orientation, the chamber is equipped with a combined LEED (low energy electron diffraction)/AES (Auger electron spectrograph) device.
A molecular/atomic hydrogen source (see sec. 3.7) has recently been installed for carrying out adsorption experiments of hydrogen on metals, semimetals or other covalent crystals.

3.4 Beam detection

At the end of the differentially pumped source arm the scattered He-atoms will get ionized and are then deflected into a quadrupole mass spectrometer (QMS) followed by a multichannel analyzer (MCA) where the He-beam intensity is measured. The QMS is mounted in a cross beam geometry to ensure a well defined path length of the He-atoms. The distance between chopper disc and detector has been determined by Mayrhofer-Reinhartshuber[75] to $L_{CD} = (1650 \pm 3)$ mm.

3.5 Time of flight measurements

Following the thermal atom beam from the source, it is passing through a skimmer into the second stage where a pseudo-random chopper disc is positioned for enabling Time-of-Flight (TOF) measurements. Afterwards the beam hits the sample, is deflected and will be detected at the end of the detector arm. The pseudo-random chopper disc cuts the He-beam into packets and defines the starting-point for the TOF- and therefore energy-dispersive- measurement. The detector QMS is synchronized with the chopper rotation. The signal is then modulated with the chopper-pattern but can be deconvoluted after detection. A great advantage of the pseudo-random chopper disc is that about 50 % of intensity is maintained compared to around 1 % using a single slit disc[36].

3.6 Resolution of the apparatus

There are several effects resulting from beam creation, detector speed, apparatus geometry and inelastic scattering influencing signal peak intensity and width. They are all reviewed in detail in the Phd Thesis of A. Tamtögl[31]. Here only a short overview will be given.

- **Influence of Scattering Geometry on the Intensities**
  The angular incidence of the beam and the fixed angle source-detector arrangement lead to different intensities of symmetric diffraction peaks due to the kinematical factor $\frac{k_{G_z}}{k_{i_z}}$ when the illuminated spot size is smaller than the area seen by the detector (Rutherford-type). For the so called Toennies-type apparatus, the area seen by the detector is bigger than the spot size, so the kinematic factor will cancel out and the measurements should reveal symmetric diffraction peaks.

- **Broadening of Angular Distribution (specular and diffraction peaks)**
  The angular width of the diffraction peaks is a result of the velocity spread and the angular distribution of the incident He-beam, while the elastic peak is not influenced by the velocity distribution.

- **Transfer Width and Surface Coherence Length**
  The transfer width is the minimum lateral dimension where the surface must be perfect to produce diffraction peaks limited only by instrumental effects. The instrumental width θ_{app} can be approximated by a formula of Comsa[76] including all aperture dimensions, length and angles of the apparatus. The so called coherence length describes the contribution of surface defects to the broadening of the peak θ_w. So the total angular broadening gives $\theta_{tot}^2 = \theta_{app}^2 + \theta_w^2$.

- **Resolution of TOF and Phonon Dispersion Measurements**
  The contribution to the half-width of the measured TOF peaks originates from the velocity distribution of the He-beam, the finite width of the chopper slit and the finite ionization length of the QMS which are all known. This width can then be transfered into an energy spread ΔE_f. An additional contribution to that width is inherent to inelastic effects due to the uncertainty of the phonon energy and is referred to the so-called kinematic smearing effect.

- **Elastic Effects in Inelastic Measurements**
  Due to the energy spread of the He-beam, elastic peaks appear in inelastic measurement which are shifted from zero energy transfer. These peaks, which are called *deceptons* or *spurions*, could be misinterpreted as phonons but due to there characteristic dispersion they can easily be distinguished from real phonons.

Considering all the effects mentioned above, the angular resolution of H.A.N.S is 0.1° and the energy resolution is estimated to $\Delta E/E = 1\%$.

3.7 Atomic hydrogen source

For carrying out hydrogen adsorption experiments on crystal surfaces, a doser for atomic hydrogen of the Bischler and Bertel- type[77] has been installed at the main chamber. The source produces a beam of atomic hydrogen and basically consists of a tungsten capillary which is heated by electron bombardment from a tungsten filament. When a stream of molecular hydrogen flows through the capillary, the molecules will start to dissociate at a temperature above 1850 K and a beam of atomic hydrogen is formed at the tip. The angular distribution and the degree of dissociation of sources of this type have been determined in other works[78,79].

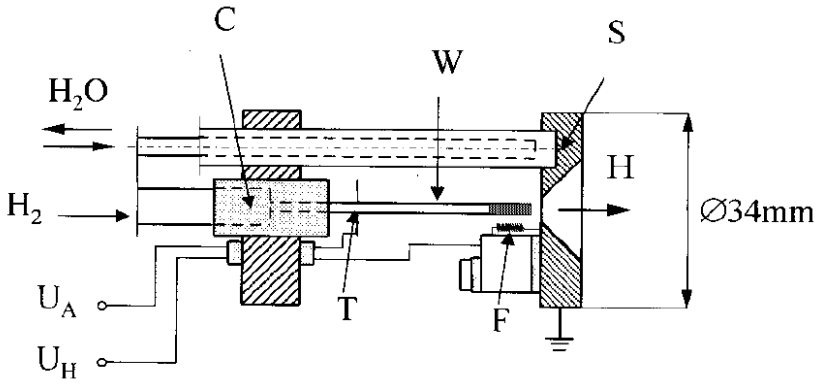

Figure 3.3: Schema of the hydrogen source[78]. The tungsten capillary (W) is heated by the filament (F). The copper shield (S) is water cooled to prevent the sample from undesired contamination. U_A and U_F are the acceleration and the filament voltage. Also the H_2 inlet is denoted.

The installed source is very similar to the hydrogen doser described and characterized in detail in a paper by C. Eibl et al.[78], which is schematically shown in fig 3.3. The tungsten capillary (W) has a length of 45 mm, an outer diameter of 1.6 mm and a inner diameter of 0.6 mm. The filament (F) originates from a 21 W car bulb and is heated by the filament voltage (U_H) until electron emission. The high voltage U_A accelerates the electrons towards the capillary and is heating it via bombardment. The water cooled copper piece surrounding the capillary tip shields the sample from radiation. For this source the angular distribution of the effusing hydrogen atoms has been experimentally obtained for different source temperatures at a distance of 63 mm from the tip and shows a strongly forward focused behavior. Also C. Eibl[78] reports nearly 100 % dissociation above 1900 K for a gas flux smaller than $2 \cdot 10^{14}$ H-atoms/s .

Figure 3.4 shows the position of the used hydrogen source within the chamber and with respect to the sample. The source is bent to aim at the sample. The distance from the capillary tip to the sample has been determined to $d_{TS} \simeq 68$ mm using a probe head when the manipulator is at position z = 24.5 mm and $\theta = 268°$.

Standard values for operating the installed source have been determined by L. Marx [80] on an experimental high vacuum set up using a pyrometer and a quadrupole mass spectrometer (QMS). A heating current of $I_H = 1.5$ A and an acceleration voltage of $U_A = 1100$ V lead to an electron emission current of $I_E = 31$ mA and a capillary temperature of 1450°C. The hydrogen dissociation was proved using a QMS and observing the decrease of the H_2 peak.

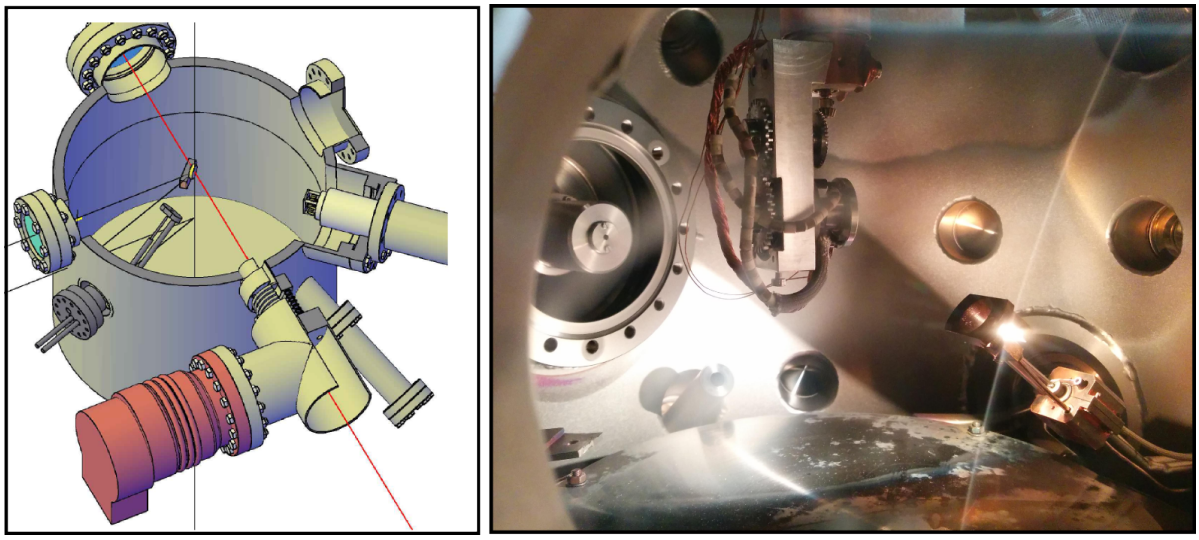

Figure 3.4: Hydrogen source position within the main chamber.

3.8 Operation of the H-source

In this section the operation of the hydrogen source inside the main chamber of HANS will be described. Also the proof for successful dissociation will be given.
For operating the hydrogen doser (see figure 3.5) a high voltage source [1], a conventional power supply [2], a water cooling system and a molecular hydrogen supply [3] are required. For precise dosing of the H_2 gas flow a fine leak-valve [4] is installed. To control and monitor the operation all important parameters are displayed on the equipment. Indication for dissociation can be recognized *tracking the H_2 peak* using the residual gas spectrometer.

As described above, the tungsten-capillary is heated by electron bombardment. The adjustable parameters are:

- The *heating current* $\mathbf{I_H}$ (max. 1.5 A !!) of the filament and
- the *acceleration voltage* $\mathbf{U_A}$ (max. 1.2 kV !!) to accelerate the electrons from the filament towards the capillary.

These two parameters will set the *emission current* $\mathbf{I_E}$ and therefore adjust the temperature of the capillary. I_E can be limited at the HV-source, this way it can be used to control the dissociation. The capillary temperature is $\approx$ 1700 K, for standard operation values I_H = 1.5 A, U_A = 1000 V, which give I_E = 28 mA.

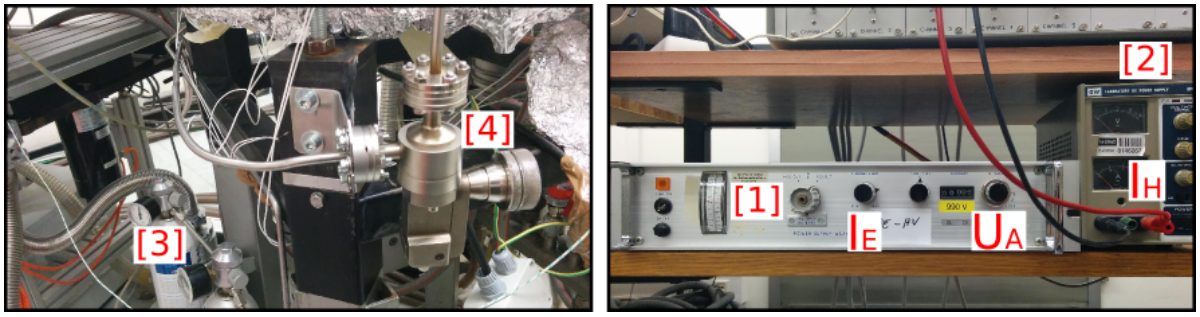

Figure 3.5: Control units for the atomic hydrogen source. High voltage source [1], conventional power supply [2], molecular hydrogen supply [3] and the fine leak-valve [4]. Control knobs for U_A, I_E and I_H are marked as well.

The following step by step manual shall be considered at each operation:

NOTE: When the H-source has not been in operation for a while and after each change of the H_2-minican, ensure that the H_2 pipeline is clean and has been pumped for a while. To check the cleanness, watch the residual gas spectrum and open the H_2 valve at cold capillary. Only the H_2 ad H peak should rise without any significant rise of the N_2, O_2 or H_2O peak. Also degas filament and capillary more carefully.
CAUTION!! At any move of the **manipulator**!!! Never move wide angles and great distances at once, always proceed in little steps and watch inside and outside the chamber to avoid any collision. Move the x and y axis if necessary before rotations. Unmount the AES/LEED connectors!

1. In the beginning make sure that the main chamber pressure is low ($\approx 10^{-10}$ mbar), the H_2 inlet valve is closed, and the main chamber is separated from beam and detector chamber.

2. Make sure that both in- and outflow valve for water cooling are opened.

3. Position the sample at the LEED- position (12/22.1/271) $\Theta = 138°$, to minimize possible undesired contamination during degassing of filament and capillary.

4. Note the base pressure of the system and start the H_2 tracking using the residual gas spectrometer. The H_2 tracker can operate throughout the experiment and should be observed while adjusting the control units. Degas QMS if necessary.

5. Begin heating the filament (From now on always be careful that the system pressure stays below 10^{-6} mbar): Slowly (within 5 minutes) increase the heating current I_H up to 1.5 A (U_H at around 10 V). The filament will start to glow and can be watched through the windows.

6. Switch on the HV-source and increase the acceleration voltage U_A to 800 V and limit the emission current I_E to 15 mA. The capillary will start to glow as well.

7. Now degas filament and capillary at this setting for a while and wait until the main chamber pressure settles and the system is thermalized.

8. Make sure the valve for pumping the H_2-pipe is closed and open the valve at the H_2-minican. Then carefully open the leak valve to the chamber and watch the pressure. Adjust to $5 \cdot 10^{-8}$ mbar (in fact, calculate displayed pressure $\cdot 2.4$, because

of pressure gauge factor for H_2). Also watch the H_2-tracker and notice the strong rise of the signal.

9. When pressure and counts of the tracker are stable, start increasing U_A to 1000 V. Increase the emission current limit to maximum (fully clockwise). The emission current should rise to around 25-30 meV. Now the H_2 tracker-signal should decrease a little delayed in time. Dissociation is now active and can be controlled by the emission current limiter.

10. To quit operation, decrease I_E to 15 meV, then decrease U_A to 0 V. Afterwards slowly decrease I_H of the filament. The pressure will return to $5 \cdot 10^{-8}$ mbar. Close the H_2 leak-valve, then close the minican. Finally close the valve for cooling water inlet.

As soon as the desired sample temperature is reached and the H-source is in operation and can be controlled, exposure can be started.

1. Limit the emission current I_E to no-dissociation (not lower than **15 meV**, as the electron stream becomes instable)

2. Bring the sample into exposure-position: (6/24/24.5) $\Theta = 268°$. **Be careful while moving the manipulator!** Watch cooling- pipes for LN_2 and remove them temporarily if necessary. Also watch inside the chamber to prevent damage on any system (especially the LEED-screen).

3. Start H- exposure by increasing the emission current I_E. Watch the H_2 tracker for dissociation and keep on going until the desired amount of exposure (Langmuir, see section 2.7.7, L = pressure $\cdot$ time) has been dosed, then stop dissociation by decreasing the emission current I_E.

4. Bring sample into desired analyzer-position (LEED or HAS, see laboratory journal)

5. To quit operation of the source, see step 10 above.

3.8.1 Proof of dissociation

Successful dissociation is proved by monitoring the system's pressure and the residual gas peak of H_2. Both methods are not well suited for a quantitative analysis of the degree of dissociation. However, a sophisticated characterization of a similar doser can be found in the paper by C. Eibl[78].

Pressure increase: As the H_2 molecule separates into two H atoms, the partial pressure will increase according to the ideal gas law. The different pumping speed for H and H_2 can be neglected as the H atoms will recombine before getting pumped. When there are also no other contributions to the pressure, from for example degassing filaments, the pressure should increase by about a factor of 2 (at 100 % dissociation).

H_2 peak decrease: The residual gas QMS can track the H_2-peak (mass 2) over time. Although the sensitivity and accuracy for such a low mass is rather bad and a particular H_2 background is always present, a significant decrease of the H_2 peak can be expected upon dissociation. The QMS is positioned far away from the H-source which makes recombination very likely and the drop must be considered rather small.

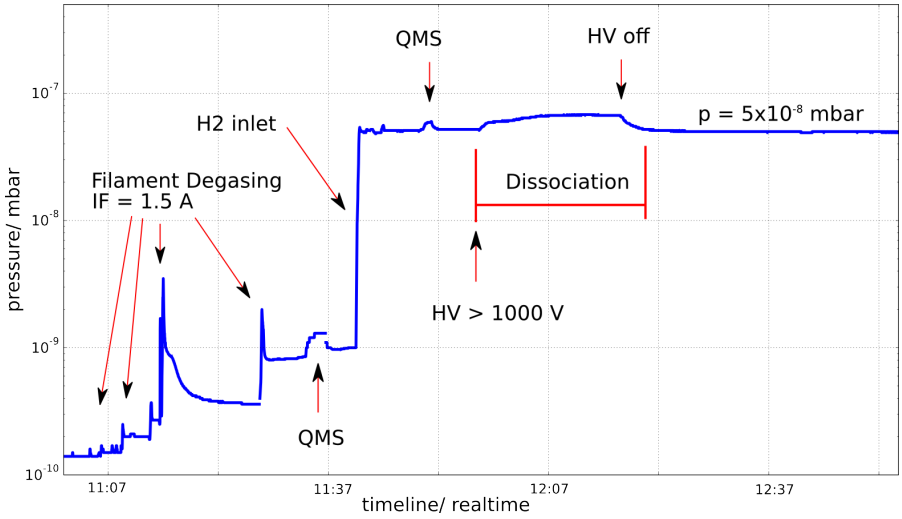

Figure 3.6: Pressure sequence during operation of the hydrogen source. Degassing processes as well as the QMS operation are visible. Upon H_2 inlet at a pressure of $5 \cdot 10^{-8}$ mbar and capillary heating, dissociation starts and becomes visible as a slight pressure increase. Quitting capillary heating stops dissociation and the pressure recovers.

In figure 3.6 and 3.7 these statements can be retraced.

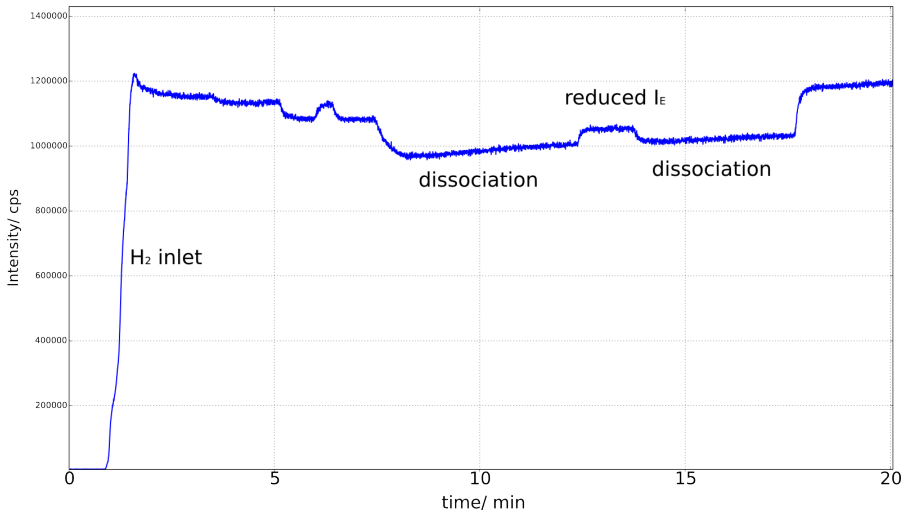

Figure 3.7: H_2 intensity track of the residual gas QMS during operation of the hydrogen source. H_2 signal decrease due to capillary heating is visible. Dissociation can be controlled by the emission current limiter.

3.8.2 Pressure at the capillary exit

The effective hydrogen pressure at the capillary exit p_c is important to estimate the dosage of hydrogen on the substrate. It can be related to the main chamber pressure increase following the paper by C. Eibl[78]. The effective pressure p_c can be calculated from the flux through the nozzle assuming equilibrium conditions in the capillary and the chamber.
The H_2 flux L through the capillary can be calculated from the rise of the partial pressure of H_2 Δp_{H_2} in the chamber:

$$L = KS\Delta p_{H_2}. \tag{3.4}$$

Here S is the pumping speed for molecular hydrogen and K is a constant factor ($K = N_A/RT = 2.41 \cdot 10^{19}$ mol/mbar l). In equilibrium the impingement rate N of the chamber gas on the capillary opening $A = 0.28$ mm^2 is equal to the Flux L out of the capillary:

$$L = A \cdot N = \frac{A \cdot p_c}{\sqrt{2\pi m k_B T}}. \tag{3.5}$$

Here, T is the temperature of the capillary, m the mass of a hydrogen molecule and k_B is Boltzmann's constant. At higher temperatures the molecule will dissociate into two atoms which changes the pressure. This can be considered by assuming constant mass flow $M = m \cdot N$ through the leak valve with and without dissociation. Introducing the

degree of hydrogen dissociation α as a function of temperature and pressure, this, after some mathematical conversion, leads to[78]

$$p_c(T,\alpha) \;=\; p_c(300K)\cdot\sqrt{\frac{T}{300}}\cdot\left(\frac{1+\alpha}{1-\alpha+\sqrt{2}\alpha}\right) \tag{3.6}$$

The pressure at the capillary exit is important when the exact exposure or dosage of hydrogen on the sample needs to be known. This is particularly important when adsorption systems at different coverages are studied.
In figure 3.8 the degree of hydrogen dissociation as a function of capillary temperature and the effective pressure at the capillary outlet as a function of temperature are shown for three different H_2 partial pressures in the main chamber. From estimating the capillary temperature and a particular main chamber pressure rise, the effective pressure can be found.

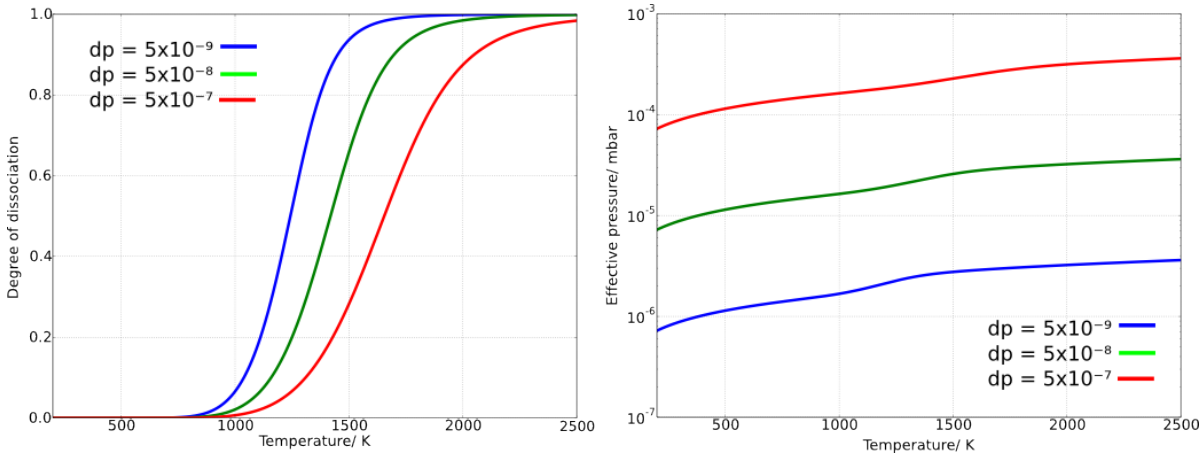

Figure 3.8: Degree of dissociation and effective hydrogen pressure at capillary exit versus temperature for different hydrogen partial pressures in the main chamber. Calculated following the paper of C.Eibl[78] and adapted for the particular system.

To treat the outflowing gas from the capillary as isotropic is of course not true. Experiments[78] always give an effective pressure of one order of magnitude lower than suggested by equation 3.6. This means the graphs in figure 3.8 give only an estimation. For an exact determination of the effective pressure corrections and experiments as described in the work of C. Eibl[78] are necessary.

3.8.3 Vacuum system of the main chamber

For sophisticated adsorption experiments, including deposition and thermal desorption, a good knowledge of the conditions and performance of the vacuum system is necessary. An important parameter is the pumping speed S (l/s), which is the gas volume pumped in a period of time by the system. Determining the pumping speed S for H_2 is particularly important to estimate the effective pressure at the hydrogen capillary outlet, as described in section 3.8.2.
In the molecular gas flow regime, the pressure of the pumped system follows an exponential behavior:

$$p_f \;=\; p_0 e^{-\frac{S}{V}\cdot t}. \tag{3.7}$$

Where p_f and p_0 are the final and the starting pressure, V is the chamber volume, and t the time needed to pump from p_0 to p_f Integrating this equation gives

$$S \;=\; \frac{V}{t}\cdot ln\left(\frac{p_0}{p_f}\right) \tag{3.8}$$

The experimental procedure was as follows: First UHV conditions have been created by several backing cycles at 140°C for at least 72 h, until we reached a base pressure $< 10^{-10}$ mbar. Then the system was flooded with H_2 using a fine leak valve at a distinct pressure. Then the valve has been closed and pressure over time was recorded every second.
From the logarithmic plots the decrease has been fitted in the linear regime, where the slope corresponds to S/V (see eq. 3.8). From a couple of measurements a slope of -0.18 $\pm$ 0.2 s^{-1} has been derived. Using the estimated chamber volume V = 120 l, the pumping speed S gives 22 l/s. The uncertainty of this value has been estimated to 10%, as the volume is not known exactly. The experimentally derived value is surprisingly small, as the used turbo molecular pump (Pfeiffer TMU521YP) has a nominal pumping speed of $S_{N_2} = 510$ l/s. According to the manual for the TMU521YP of Pfeiffer-Vacuum, for H_2 the pumping speed should be 80% of the nominal value.

3.9 Sample holder improvements

To make a wider range of samples and temperature conditions accessible for HAS experiments, some suggestions for improving the sample-holder construction have been gathered and are presented here. The current solution is well described in the thesis of A. Tamtögl[31].

3.9.1 Sample holder design

Within a project at the university, a UHV transport system for different samples is implemented at several laboratories at the institute. This enables the possibility to use different analysis methods on the same sample without exposing the sample to atmosphere and so prevent it from contamination or destruction. The sample-plate,

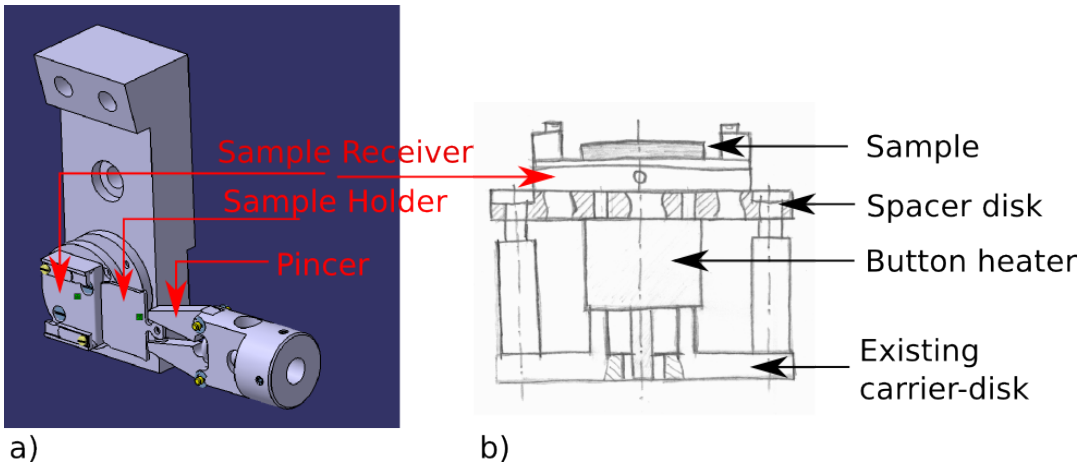

Figure 3.9: FerroVac- sample holder and transport pincer (a). Sample holder stack showing the assembly of button-heater, spacer disk and sample receiver onto the existing button heater carrier (b).

sample-receiver and pincer system of the company FerroVac is in principle shown in figure 3.9 a. In figure 3.9 b, the new sample holder stack is shown. It is necessary to use a spacer disc for connecting the sample receiver from FerroVac onto the present construction. The sample-plate, receiver and spacer disk -stack is made from titanium and slightly adapted for our needs. The receiver comes with additional M2 thread holes for cooling and temperature sensor connectors. The spacer disk is custom made.
The present sample holder system can be used as it is with the only exception, that the sample-cover plate is replaced by the spacer disk and the mounted receiver. Also the temperature measurement has to be replaced closer to the sample.

3.9.2 Cold-head cooling system

At present the sample is cooled using liquid nitrogen (LN_2) fed into a reservoir in the sample holder via a pipe system through the manipulator. The LN_2 is provided by a 100 l Dewar container which is sufficient for cooling the sample down to -160 °C for 8 to 9 hours (aluminum sample holder). For reaching lower temperatures and to enable a more controlled cooling procedure, an additional cold- head cooler can be connected to the sample. This issue has already been treated in the work of M. Polanz[81], where heat conduction simulations are presented which predict temperatures down to -190 °C. Here the practical implementation is discussed. It is necessary to mount the cold head

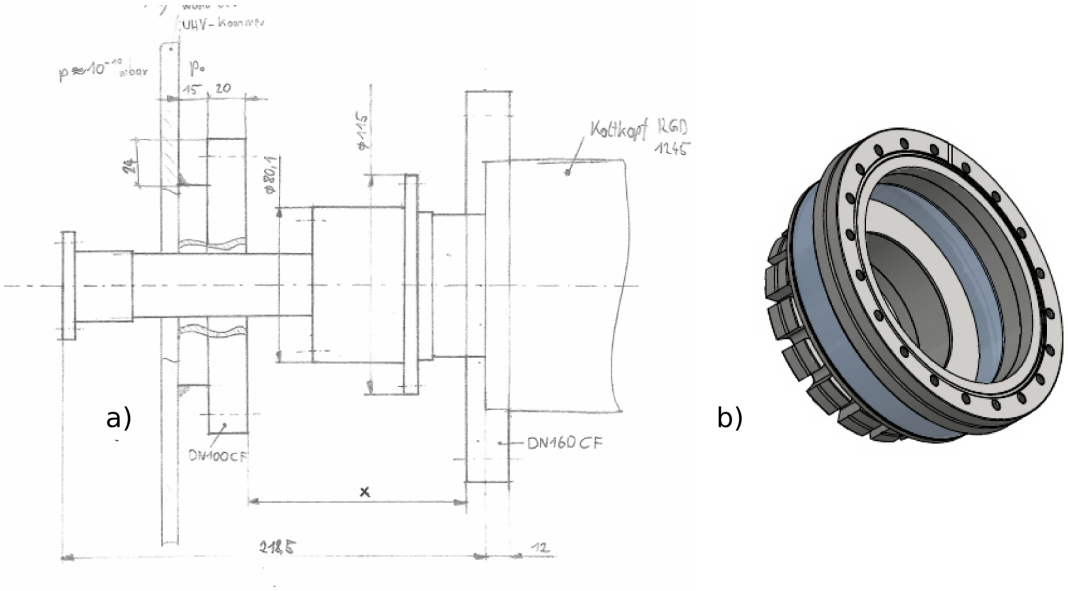

Figure 3.10: Cold-head reaching into the main-chamber including most important dimensions (a). Membrane- flange from COMVAT (b). The blue middle part indicates the welded membranes for vibration decoupling.

(Leybold, RGD 1245) onto the main chamber and to provide good thermal conduction from the cold-head tip to the sample. For the first problem a flange DN 160 CF (cold-head) to flange DN 100 CF (main chamber) connector is needed. The distance which the cold-head is reaching into the main chamber and vibrations from the cold-head strokes are critical. Also the outer dimensions of the two cold-head stages have to be considered (see figure 3.10 a). A custom-made membrane flange (COMVAT) fits all the requirements (figure 3.10 b) and is ready to be installed at the main chamber.
For a good heat conduction a thick and flexible, oxygen free copper wire should be used to connect cold-head tip and sample holder. As the space in and access to the

main chamber are restricted, this connection must be designed in a way so that it can be easily demounted using only one hand. This will be necessary when installing the cooling system and in case the manipulator is removed.

3.10 Sample preparation

Standard procedure for cleaning the Sb(111) surface are several cycles of Ar^+- ion sputtering (1.6 kV, p_{Ar} = 1x10^{-6} mbar, 15-20 min), followed by annealing at 200°C for > 24 h. Sample cleanness can be checked by performing Auger electron spectroscopy. At a base pressure of < 10^{-10} mbar the sample stays clean for days until contamination becomes visible in the HAS signal.

3.10.1 Auger electron spectroscopy

The main chamber is equipped with an Auger Electron Spectrograph (AES), using the 4-Grid LEED optics as a retarded field analyzer (RFA). As the AES is used infrequently and no fast-use manual is available, a summarized manual for standard measurements scanning for contamination on the Sb(111) surface is presented here. Detailed manuals and operation parameter as defined and provided by the producer (Omicron NanoTechnology) are however available and should be read carefully before using the AES for the first time.

Wire the HV-Screen of the LEED optics correctly. Use the bigger connector labeled "MUL Pre-Amp" instead of the LEED-connector (Omicron 10356). First, the electron gun (LaB_6) has to be adjusted, then the beam optics are set at the SPECTALEED control unit and at last the program *DATAuger* is fed with the scan parameters. Data acquisition of the signal is done by controlling the lock-in amplifier and oscillator, setting start and end energies, dwell time, step size and number of scans.

The following step by step manual shall be considered at each operation:

CAUTION: Make sure the main chamber pressure stays below 5x10^{-8} mbar while operating the AES.

- Turn potentiometer SCREEN, BEAM ENERGY and FILAMENT fully counter clockwise, the potentiometer EMISSION fully clockwise. Switch the control unit on.
- Select AUGER, and note that SCREEN HV and SUPPRESSOR are not active in Auger mode.
- Slowly increase filament current I_{Fil} to 1.2 A (> 1 min, never > 1.55 A !). Check the emission current I_E, which should reach 0.3 A. Reduce I_{Fil} to 1.1 A if possible after a while. Watch system pressure! Reduce I_{Fil} if necessary.
- Increase beam energy to 1.5 keV and set lens values as stated in the test sheet ($L_{1/3}$ = 720 and L_2 = 180).
- Set Wehnelt voltage to -42 V. I_E should drop to almost zero and the beam current I_0 rise to around 16 μA.
- Now wait until I_0 stays constant. The control unit is ready.

Bring sample into working distance (22 mm from the middle of the screen). Check last sample position for AES in the laboratory journal (currently: (12/22.1/273), $\theta = 138°$).

Start the DATAuger software (be sure the licence-key (USB stick) is mounted). First, carry out a **fast scan** to find the elastic peak and check beam optics and sample position. Setup –> Fast Scan... . Observe the elastic peak (height and shape) and optimize the parameters if necessary.

– **Parameters for fast scan:**

Oscillation frequency: 4.75 kHz LEED
Phase: 180°
Modus: High dynamic reserve, F-mode
Sensitivity: 100 mV
Time constant: 10 ms
Amplitude: 1 V_{pp}

Energy range: 1400-1550 eV
Dwell time: 200 ms

Then load a pre-defined experiment (Setup –> Experiment –> Sb2fmode), in which two runs are available. When the scans are active (ticked), they will be run one after the other. The parameters are set as default but can be changed at will by a double click. Also new experiments can be created. There is an elastic peak scan (elastic1f) and a differentiated AES scan (default) available. Auger spectra are normally shown as differentiated peaks.

– **Standard parameters for an elastic peak scan (elastic1f) are:**

Oscillation frequency: 4.75 kHz LEED
Phase: 180°
Modus: High dynamic reserve, F-mode
Sensitivity: 30 mV
Time constant: 30 ms
Amplitude: 1 V_{pp}
Energy range: 1400-1550 eV
Step size: 0.5 eV
Dwell time: 500 ms

– **Standard parameters for an AES-scan (default) are:**

Oscillation frequency: 4.75 kHz LEED
Phase: 90°
Modus: High dynamic reserve, 2F-mode
Sensitivity: 300 μV
Time constant: 300 ms
Amplitude: 4 V_{pp}
Energy range: 150-800 eV
Step size: 0.5 eV
Dwell time: 2000 ms

The elastic scan, shown in figure 3.11 a, can be used to check sample position, influence of the modulation amplitude and the energy resolution. The AES scan can be compared

to an AES-catalog to check for peaks other than the Sb-peak. Examples for clean/dirty sample are given in figure 3.11 b and c.
The Auger process is a competitive process to X-ray emission. For low mass atoms, the Auger process is more likely, which leads to more intense peaks for light elements. This means also a rather low C contamination becomes clearly visible.
From plot 3.11 (a) $\Delta E/E$ has been estimated to 0.8 %.

Shutting down the system:

- Reduce beam energy to zero. Switch filament off by first setting Wehnelt voltage to 0 V, then slowly decrease I_{Fil} ($>$ 1 min) to 0 A. Finally switch off the power supply.

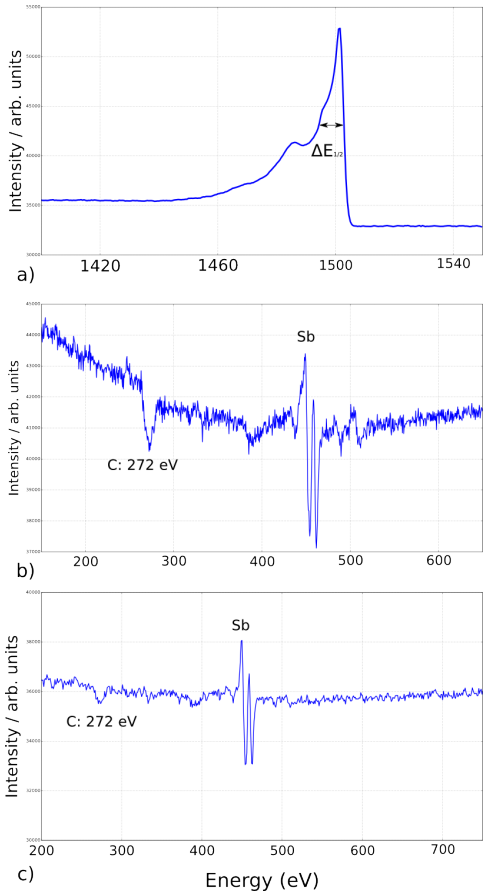

Figure 3.11: Exemplary AES-scans. Elastic peak for determining the resolution in (a). Differentiated AES scans from a dirty (b) and clean sample (c).

4 Results and discussion

4.1 The He-Sb(111) interaction potential

Good knowledge about the clean surface structure is essential to predict and interpret adsorption experiments. For this reason at first the clean Sb(111) structure will be discussed, before in the following sections the H/Sb(111) system will be treated.
According to section 2.6, the elastic Close-Coupling (eCC) approach can be used to calculate the corrugation of the electronic density distribution above a crystal surface from measured diffraction intensities. Thermal attenuation of the intensities is described by a DW-factor using the Debey-tempearture of 155 K for Sb(111) as determined by Tamtögl et al.[4]. This procedure requires an exact knowledge of the He-Sb(111) interaction potential. As presented in section 2.5, a variety of model potentials can be used and expanded into a Fourier-series. However, an analytical expression for the couplings in formula 2.66 can be found when assuming a Corrugated Morse Potential (CMP), which only contains the repulsive part of the potential (see formula 2.41). The central term of the potential, in contrast, which also contains the attractive part, can be chosen at will. This opens up the possibility for comparing reasonable potentials regarding their performance in reproducing the diffraction intensities. Especially the role and importance of the long range attractive potential part can be discussed following this procedure.
The application of this idea to Sb(111) has been published by P. Kraus et al.[8].
Here only the basic procedure and the most important results will be presented. The author's contribution to the paper was focused on the measurements and carrying out the calculations according to the code of Patrick Kraus, which is available on http://iep.tugraz.at/closecoupling.

The procedure follows a two-step fitting treatment:
Selective adsorption resonances (SARs) produce features in elastic and inelastic HAS measurements (see section 2.4.4). From the scattering geometry and the resonance conditions, bound state energies can be found when analyzing the peak positions from

Table 4.1: Fitted interaction potential parameters for the model potentials listed in section 2.5. Listed potentials see section 2.5.1.

Potential	D / meV	κ / Å^{-1}	z_p / Å	Δ	σ / Å	z_0 / Å	p	κ_r / Å^{-1}
MP	4.275	0.389	-	-	-	-	-	-
HMP	4.263	0.404	2.899	-	-	-	-	-
SMP	4.336	0.418	-	0.066	-	-	-	0.409
SMHP	4.358	0.367	6.625	0.061	-	-	-	0.367
9-3	4.454	-	-	-	5.941	-	-	0.624
12-3	5.225	-	-	-	6.065	-	-	0.848
Exp-3	4.445	1.376	-	-	-	7.168	-	0.539
Var-Ex	4.313	0.438	-	-	-	-	4.495	0.493

experiments. These bound states can now be used to fit the parameter of interesting interaction potentials to the measurements. The number of free parameters depends on the used potential and include in principle the potential stiffness, depth and its attractive part.
In the second step, the fitted potentials are plugged into the eCC algorithm which delivers the scattering intensities for a given surface structure including its corrugation. The peak-to-peak size of this corrugation is now fitted to measured elastic diffraction spectra.
Figure 4.1 a shows the fitted interaction potenials presented in section 2.5.1, the corresponding parameters are listed in table 4.1. The seven bound state energies on the Sb(111) surface used to fit the potentials can be found in the paper of Kraus et al[8].

The best fit results from the eCC calculation for a selection of used potential are plotted together with the experimentally found intensities in figure 4.1 b. Table 4.2 summarizes the results for all potentials and shows the derived peak-to-peak corrugation in percentage of the lattice constant together with the fitting-error.
The Morse-like potentials settle at a corrugation height of 14-17 % of the lattice constant. Steeper potentials tend to predict higher corrugations which is founded in the expression for the couplings that contain the stiffness. Also it is obvious, that potentials containing a non-physical attractive part, like the 9-3, the 12-3 or the CMP potential, are not able to reproduce higher order diffraction peaks. In contrast, the Shifted Hybrid Morse Potential (SHMP) -containing the $-1/z^3$ attractive part behavior- performs well also for higher order peaks and produces a reasonable fitting error. The SHMP therefore will be our choice for further calculations, including an iCC treatment. Figure 4.2 depicts the

Table 4.2: Best peak-to-peak corrugation values ξ_{pp} with respect to the lattice constant. Beam energy $E_i = 21.9$ meV, sample temperature $T_s = 300$ K. The eCC code corrected with the Debye-Waller factor was used. Err is the fitting error. Listed potentials see section 2.5.1.

Interaction potential	ξ_{pp} / %	Err / %
MP	13.65	5.23
HMP	14.69	7.27
SMP	14.69	6.45
SMHP	15.15	4.86
9-3	16.79	2.24
12-3	18.45	10.9
Exp3	16.35	4.74
Var-Ex	19.05	7.84

electronic density distribution (= Contour of constant surface electronic charge) above the surface, as predicted by the eCC treatment (SMHP). However, interaction potentials from first-principle calculations, as for example derived from R. Martínez-Casado [82] for the MgO(100) surface, should be considered in the future.

The obtained corrugation values are surprisingly high for a semimetal like Sb. The Sb(111) surface is conductive, where a flat surface corrugation similar to metals is expected due to to the Smoluchovski-effect [83].

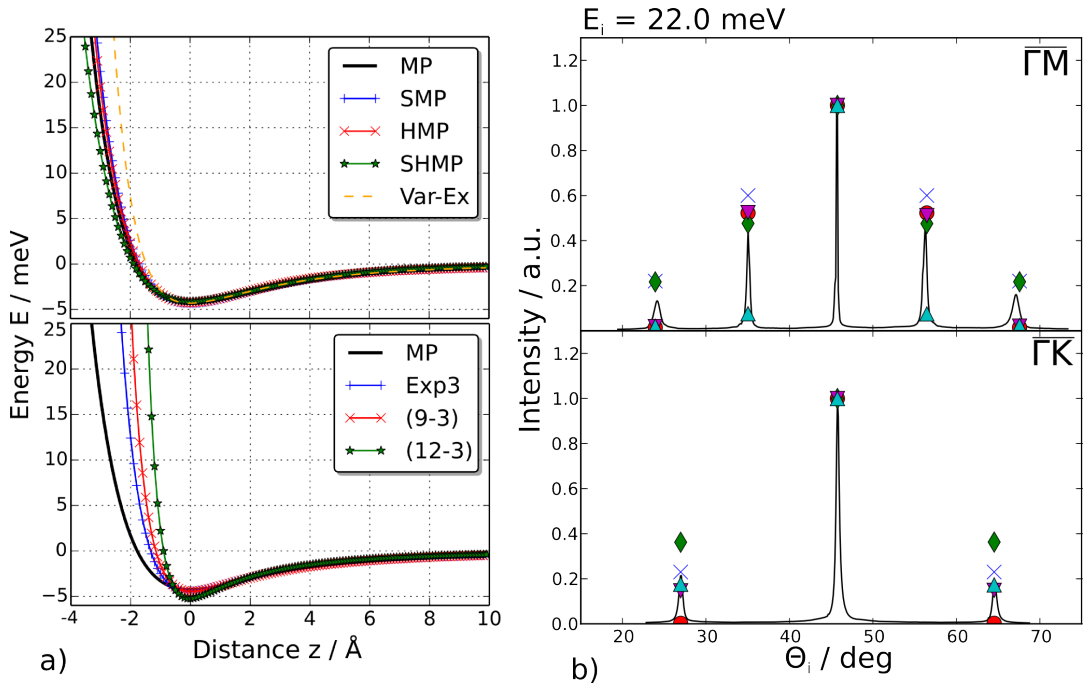

Figure 4.1: Elastic CC results for selected potentials on the clean Sb(111) structure, taken from the paper of P. Kraus[8]. In (a) the fitted potentials are illustrated. The upper graph shows Morse-like potentials whereas in the lower graph non-Morse potentials are shown. In (b) the intensity results from the eCC calculations are shown together with the experiment, indicated by the blue crosses (area of the peaks). Red circles, green diamonds, magenta downward triangles and cyan upward triangles signify the Morse, Shifted Hybrid Morse, 9-3 and 12-3 potentials, respectively. The intensities have been attenuated using a Debye- Waller factor at a surface temperature of 300 K.

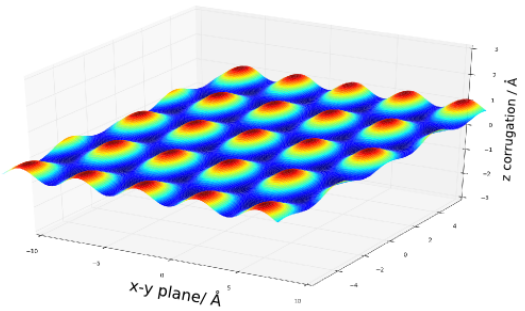

Figure 4.2: Illustration of the electronic corrugation above the clean Sb(111) surface as calculated via eCC for the SMHP-potential: $\xi_{pp} = 15.15\ \%\ \approx 0.67$ Å.

4.2 HAS on the H/Sb(111) adsorption system

In view of hydrogen adsorption on the Sb(111) surface the results of section 4.1 allow a couple of careful predictions.
The relatively high potential modulation could result in a predominance of adsorbate-substrate forces compared to mutual adsorbate-adsorbate interactions. This would consequently prevent H atoms from forming superstructures, at least at low sample temperatures. A strong weakening of the coherent intensity due to diffuse scattering can therefore rather be expected than additional diffraction peaks. Also surface diffusion is expected to be weak at low temperatures.
In the review of K. Christmann[51] it is suggested for H atoms on metals that they tend to occupy sites with the highest coordination number. In case of Sb(111) this would be a three fold site in the center of a triangle of Sb surface atoms.
If molecular hydrogen will dissociate and finally chemisorb on the Sb(111) surface is not easy to say. It is a question of the binding energy of a single adsorption site with respect to the intermolecular binding force and the shape of the interaction potential (see section 2.7.3).

Experimental conditions: In the following sections the H/Sb(111) system is investigated by means of HAS, LEED and AES.
All HAS measurements are elastic diffraction scans according to section 2.4.2 with the main chamber base pressure at $p_0 = 7 \cdot 10^{-11}$ mbar, carried out at a nozzle temperature of 75 K and a nozzle pressure of 60 bar. This corresponds to a beam energy of $E_{kin} = 16.18$ meV or a de Broglie wavelength of $\lambda = 1.13$ Å, respectively (see section 3.2). According to the hexagonal two dimensional structure of the Sb(111) surface (see figure 2.1) in $\overline{\Gamma M}$ direction, first and second order peaks are expected at $\pm$ 12.5° and $\pm$ 25.7° measured from the specularly scattered beam. The following experiments have all been carried out along this crystal direction.

4.2.1 H_2 on Sb(111)

The first attempt to adsorb hydrogen on the Sb(111) surface has been carried out using molecular hydrogen. The question is if H_2 will dissociate spontaneously and adsorb as atomic hydrogen on the surface, as described in 2.7.3.
The experimental procedure was as follows: After preparing a clean Sb(111) sample and checking the cleanliness using AES, a reference elastic spectrum has been measured by means of HAS. Then the main chamber ($p_0 = 7 \cdot 10^{-11}$ mbar) has been flooded with molecular hydrogen at a pressure of $p_{H_2} = (2.4 \cdot) 5 \cdot 10^{-8}$ mbar. After exposing the sample for a particular amount of time (1 min $\widehat{=}$ 5.4 L), another elastic scan is performed. This has been done with the sample at room temperature and cooled down to -160°C.
The measurements in figure 4.3 a and b clearly show that the diffraction spectrum stays unchanged at both sample temperatures even at high exposure. Also, the diffraction spectrum confirms the geometric structure of the Sb(111) surface. Neither the geometric nor the electronic structure of the surface changes. From this it can be concluded that no spontaneous dissociation of hydrogen on Sb(111) takes place between -160°C and 20°C sample temperature. LEED investigations suggest the same result. The binding energy of atomic hydrogen on Sb(111) must therefore be lower than half of the intermolecular binding energy of H_2, 4.57 eV, or the activation energy for dissociation is too high.
The spectra of the cooled sample in figure 4.3 b produce higher intensity compared to the room temperature spectra because of less inelastic contributions. The strong asymmetry of the cooled measurement compared to the room temperature measurement may arise from temperature induced alignment problems.
According to this result, molecular hydrogen needs to be pre- dissociated before adsorption on the Sb(111) surface.

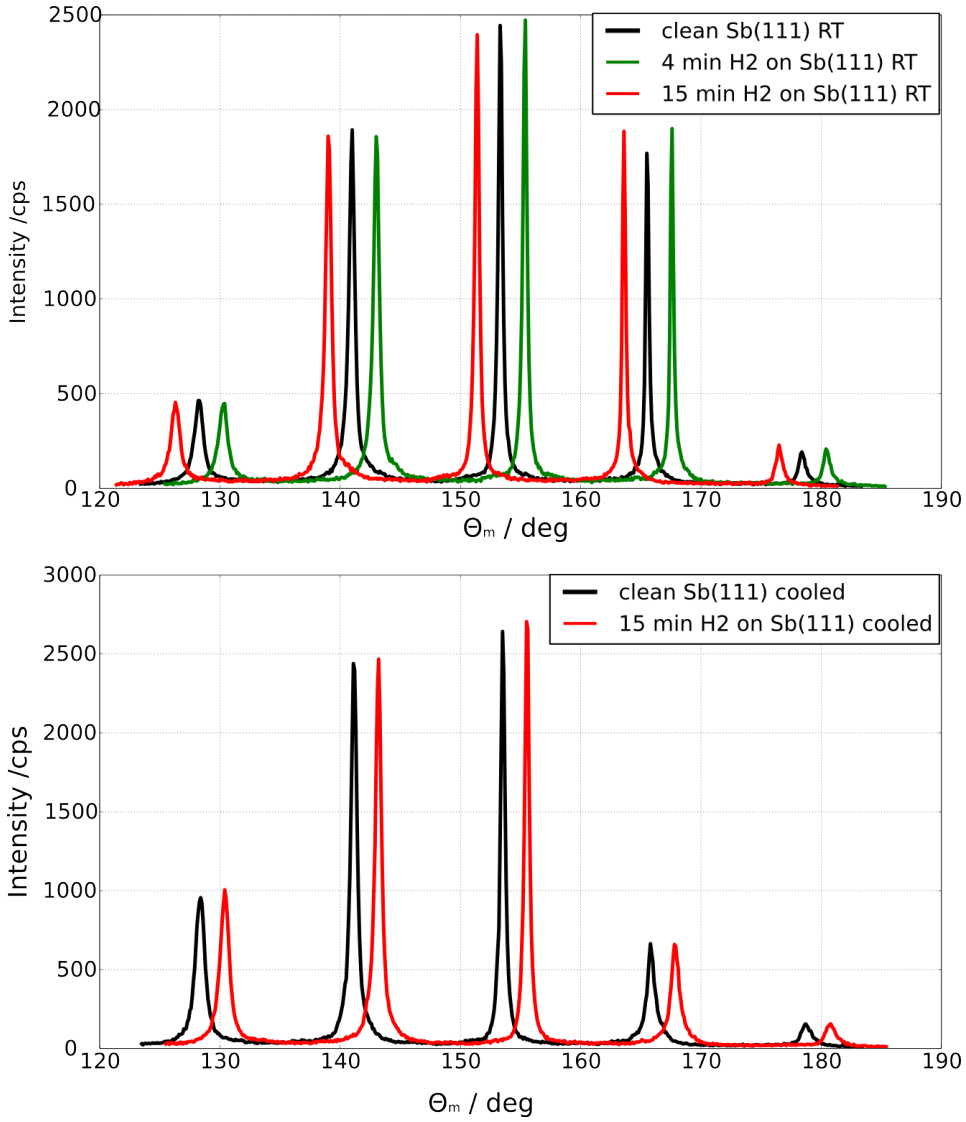

Figure 4.3: HAS scans of clean and molecular hydrogen- exposed Sb(111) with sample at room temperature and cooled to -160°C. The H_2 exposed spectra are shifted ± 2° for better visibility. The beam intensity is plotted versus the manipulator angle Θ_m.

4.2.2 H on Sb(111)

In section 4.2.1 it has been shown that no spontaneous dissociation of the hydrogen molecule occurs on the Sb(111) surface. This means the intermolecular bonding has to be broken before a possible successful adsorption. A description of the used atomic hydrogen source to dissociate the molecule in advance can be found in section 3.7.
The experimental procedure was as follows: Starting out with a clean sample, elastic reference scans have been produced first with the sample at room temperature and then cooled down to -160°C. A large amount of atomic hydrogen (>1000 L) is then dosed to the cooled surface and an elastic scan is produced right afterwards. In figure 4.4 this sequence is shown. The diffraction pattern of the cooled Sb(111) surface completely disappears when exposing it to atomic hydrogen. Only the multi-phonon background remains in the signal. LEED investigations of the cooled sample before and after H adsorption (see figure 4.6) show the same results.
Then the sample is heated up back to room temperature and now the diffraction pattern returns.(figure 4.4). The observed spectrum is now lower in intensity than the clean sample measurement with the peaks located at the same angles. This suggests a change of the electronic corrugation due to an adsorbed (1x1) hydrogen superstructure. In the next step, the sample is heated to 200°C in order to desorb the hydrogen overlayer. With the sample back at room temperature another elastic scan shows that the original intensity recovers pretty well and the clean Sb(111) surface is restored (figure 4.5).

In another experiment, atomic hydrogen was exposed on the clean sample at room temperature. Figure 4.7 makes clear that also in this case the intensity is lowered significantly compared to the clean structure scan. This can again be explained by a change of the electronic corrugation induced by an adsorbed (1x1) hydrogen superstructure. The LEED pictures of the clean and the H adsorbed layer in figure 4.8 differ only slightly in intensity, as the electrons probe much deeper, but it gives evidence for an ordered structure. However, the HAS intensity is more than twice as high as the elastic spectrum derived from the H/Sb(111) system, where the hydrogen has been adsorbed at the cool sample and the superstructure emerged during warming up to room temperature. An explanation could be that the Sb(111) surface is not completely covered and there is still a great signal contribution from uncovered areas in between ordered hydrogen islands. The exposure has been the same in both experiments which suggests that the sticking coefficient is much lower on the sample at room temperature compared to the cooled sample.

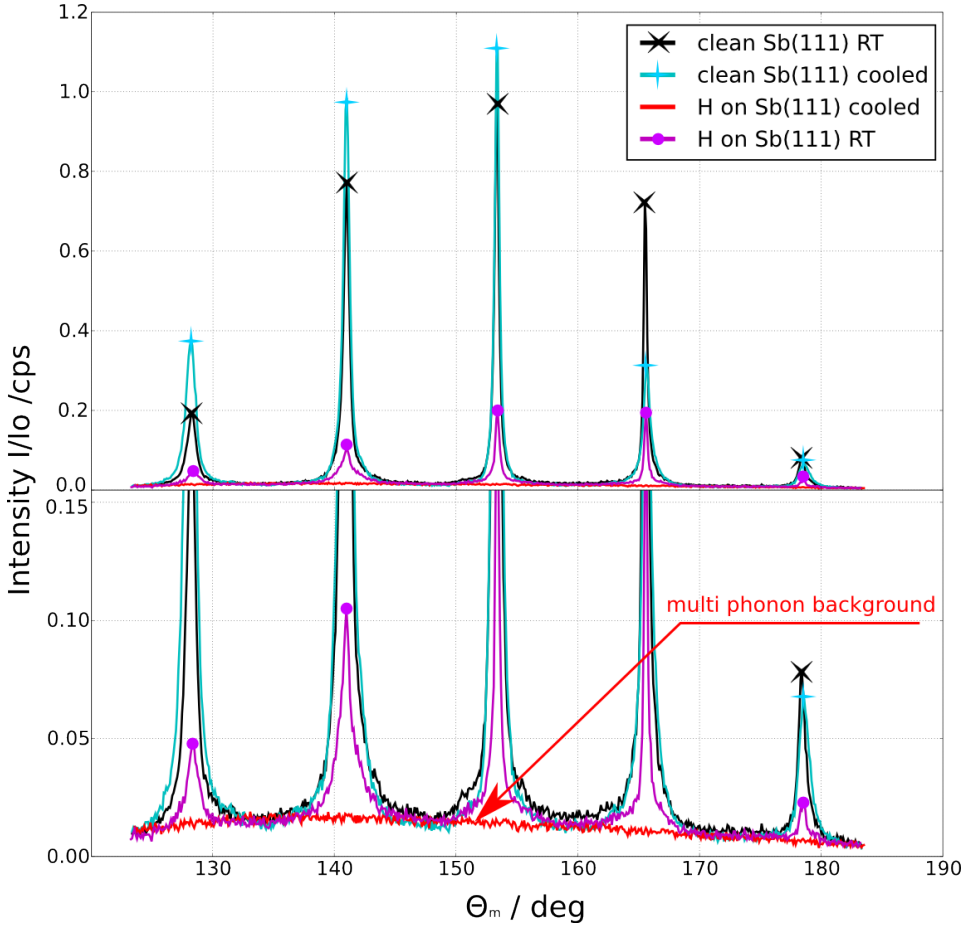

Figure 4.4: HAS scans of clean and atomic hydrogen- exposed Sb(111) with sample at room temperature and cooled to -160°C. The beam intensity is plotted versus the manipulator angle Θ_m. The intensity is normalized to the clean sample at room temperature measurement (black stars). Cooling down the sample gives the magenta plus line. After adsorbing atomic hydrogen only the multi phonon background (red line) remains. When warming up the sample back to room temperature, the cyan pattern marked with circles emerges. The bottom frame zooms out the lower part of the spectrum.

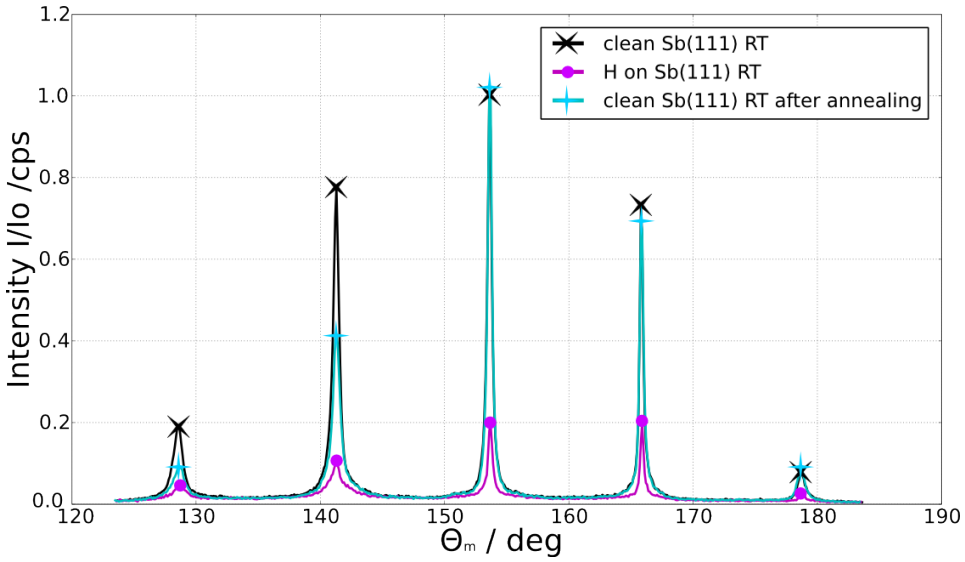

Figure 4.5: HAS scans of clean and atomic hydrogen- exposed Sb(111) with sample at room temperature and cooled to -160°C. The beam intensity is plotted versus the manipulator angle Θ_m. The intensity is normalized to the clean sample at room temperature measurement (black stars). The magenta circles refer to the H/Sb(111) system at room temperature. After annealing the sample at 200°C and cooling the sample back to room temperature, another elastic scan produced the cyan plus pattern. At least the specular peak is recovered completely after desorbing the hydrogen overlayer.

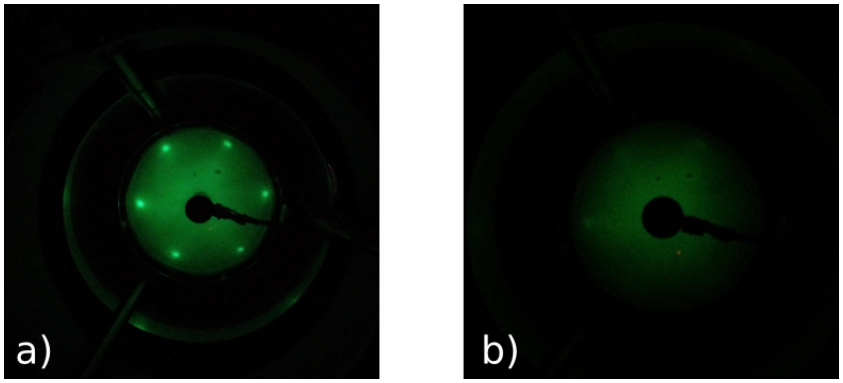

Figure 4.6: LEED pictures of the cool sample before (a) and after (b) hydrogen adsorption. The intensity vanishes almost completely.

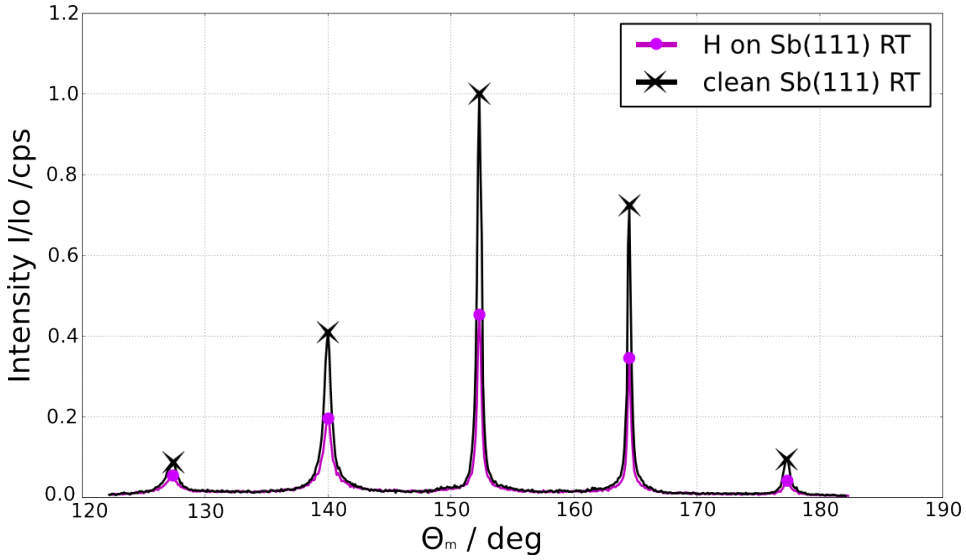

Figure 4.7: HAS scans of clean and atomic hydrogen- exposed Sb(111) with sample at room temperature. The beam intensity is plotted versus the manipulator angle Θ_m. The intensity is normalized to the clean sample at room temperature measurement (black stars). The magenta circles refer to the H/Sb(111) system adsorbed and measured at room temperature. The intensity is twice as high as in figure 4.4 and 4.5, where hydrogen was adsorbed on the cool sample.

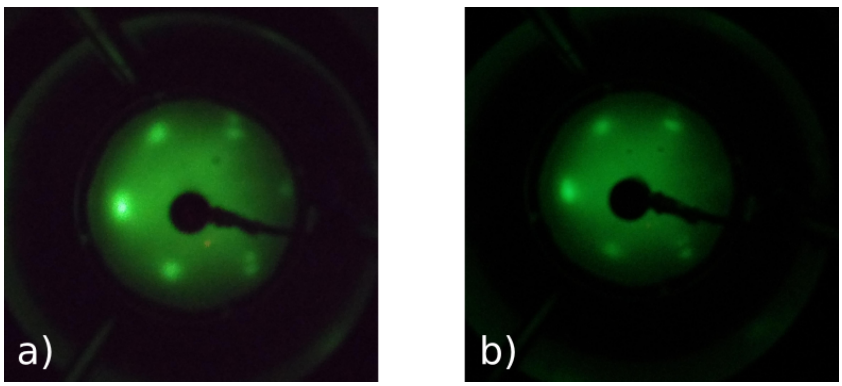

Figure 4.8: LEED pictures (25 eV) of the sample at room temperature before (a) and after (b) hydrogen adsorption. There is only a slight intensity attenuation visible, as the LEED (25 eV) electrons probe much deeper than the HAS beam.

From these results it can be concluded that atomic hydrogen adsorbed on the Sb(111) surface crystallizes in a (1x1) saturation phase at high exposure. When exposed to the cooled surface (-160°C), the H atoms are in an amorphous, randomly distributed state. This is confirmed by HAS (figure 4.4) and LEED (figure 4.6) measurements. With elevated temperatures, surface diffusion sets in giving the atoms the chance to transfer into an ordered state (figure 4.4). This ordered (1x1) phase can be desorbed by heating the sample to 200°C (figure 4.5). Atomic hydrogen also adsorbs on the Sb(111) surface at room temperature, as indicated by figure 4.7, probably with a lower sticking coefficient.

The exact parameter for the 2D lattice gas - solid transition, the activation energy for diffusion and the desorption energy can be derived by further experiments. One possibility is observing the specular intensity within the whole temperature region from -160°C to 200°C and its deviation from the Debye-Waller behavior.

A possible (1x1) hydrogen superstructure on the hexagonal Sb(111) surface is shown in figure 4.9. The hydrogen atoms are located at the adsorption sites with the highest coordination number, which is a three-fold site in the center of a triangle of Sb atoms. When comparing to figure 2.4, the H atoms are then located above the green subsurface atoms.
The corrugation of the H saturated layer is altered compared to the clean Sb(111) surface. From eCC calculations it will be possible to figure out if the corrugation is lowered or enhanced, which in turn gives insight into the binding character of the H atom on the surface.

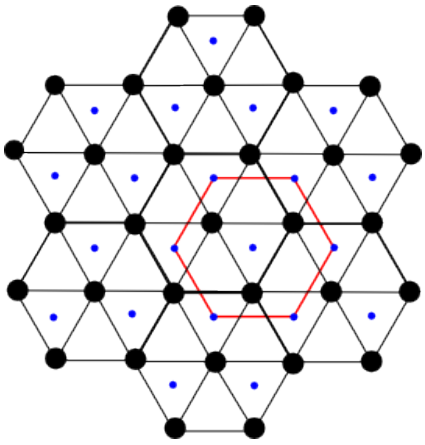

Figure 4.9: Possible H (small blue dots) superstructure on the Sb(111) surface (big black dots), obeying the hexagonal sixfold symmetry.

AES scans on the hydrogen saturated surface at room temperature have been carried out to suspend the possibility of contamination from the operation of the hydrogen source. In figure 4.10 b no additional contamination compared to the clean surface scan in figure 4.10 a can be seen. Quite the contrary happened: The carbon peak disappeared on the hydrogen saturated layer which means that the surface carbon has reacted with incoming atomic hydrogen and is desorbed from the surface before H adsorption. The surface has even become cleaner, despite the hydrogen layer.

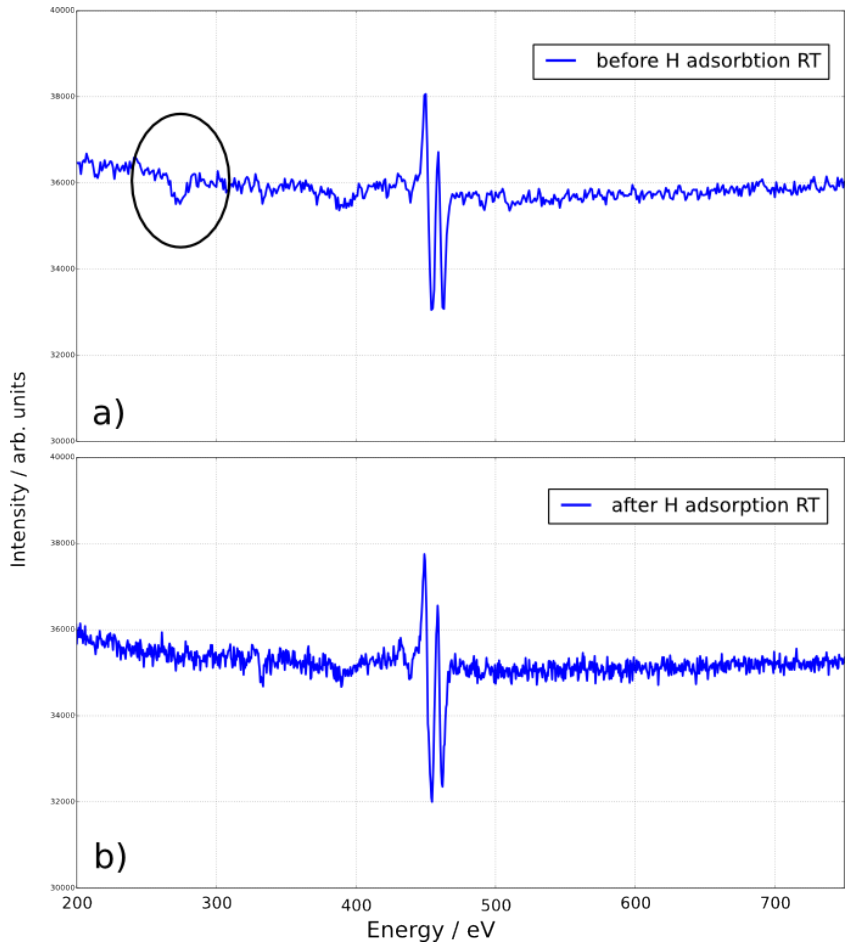

Figure 4.10: Diffracted AES scans of the Sb(111) sample before (a) and after (b) exposure to atomic hydrogen. In both graphs (a) and (b) the Sb peaks are clearly visible. The in (a) circled C peak on the contrary disappears upon exposure to atomic hydrogen. This suggests a chemical reaction between H and C forming a molecule which desorbs from the surface before H adsorbs on the Sb(111) surface.

Estimation of the binding energies:

Because of the fact that atomic hydrogen reacts with the carbon contamination on the Sb(111) surface, it can be concluded for the binding energy of C on the Sb(111) surface that it is weaker than the C-H bond, which is 4.26 eV.

As hydrogen adsorption on the Sb(111) surface is obviously not an exothermic reaction, the binding energy of H on Sb(111) must be lower than half the formation energy of the hydrogen molecule, -2.29 eV. This value is comparable to the binding energy of hydrogen on noble metal surfaces[15], like Au(111) (-2.18 eV), Ag(111) (-2.12 eV) or Au(100) (-2.27 eV).

However, Redhead's peak maximum equation[84], which is used in thermal desorption spectroscopy, can be used to estimate the activation energy of desorption.

$$E_{des} = RT_m \left[ln(\nu T_m/\beta) - 3.46\right] \tag{4.1}$$

Assuming a desorption temperature of 200°C (annealing temperature), a frequency factor of 10^{13} 1/s and a heating rate β of 0.035 K/s, gives a desorption energy of 140 kJ/K which is about 1.45 eV. This value has an error of about 20 %.
The real desorption energy is expected to be lower and can only be derived from an exact measurement of the hydrogen desorption via HAS or thermal desorption spectroscopy.

4.2.3 Summary of the results from adsorption experiments

From the experiments described in section 4.2.1 and 4.2.2 the most important statements can be summarized as follows:

- Molecular hydrogen does not adsorb spontaneously on the Sb(111) surface and has to be pre-dissociated before adsorption.
- Atomic hydrogen adsorbs on the Sb(111) surface in an amorphous state at low surface temperatures (-160°C) and forms a (1x1) saturated superstructure upon adsorption at room temperature.
- The binding energy of H on Sb(111) must be lower than half the formation energy of the hydrogen molecule, -2.29 eV. According to Redhead's equation the binding energy must even be lower than -1.5 eV.
- The amplitude of the electronic corrugation above the Sb(111) surface is altered upon hydrogen adsorption. Further eCC calculations might reveal insight into the binding character of the H-Sb(111) bonding.
- There is a phase transition from a randomly distributed amorphous layer to a (1x1) superstructure between (-160°C) and room temperature.
- The H(1x1)/Sb(111) superstructure can be desorbed via annealing of the sample at 200°C. No hydrogen contamination is present on the clean Sb(111) surface.
- Atomic hydrogen cleans the Sb(111) surface from carbon contamination. This suggests a binding energy of C on Sb(111) weaker than the C-H bonding energy, 4.26 eV.

4.2.4 Future experiments and analysis topics

The experiments and results described above can be extended and substantiated by further measurements and analysis. In the following list suggestions and possible further investigations are presented.

- Temperature dependency of the diffraction spectrum to find out possible phase transitions (onset of ordering) and desorption energy.
- Coverage dependency of the adsorption system by exposing the clean surface to a defined dosage and subsequent elastic measurements.

- Further elastic measurements from the second high symmetry direction of the surface ($\overline{\Gamma K}$).
- Measuring beam energy drift spectra to find bound states of the (1x1)H/Sb(111)-He interaction potential.
- Elastic Close-Coupling calculations to determine electronic corrugation of the (1x1)H/Sb(111) system.
- Thermal desorption experiments with adsorbed deuterium to determine the exact desorption temperature using the residual gas QMS.
- Inelastic HAS measurement on the (1x1)H/Sb(111) system to reveal the surface phonon dispersion.
- Inelastic HAS measurements to find the dispersionless hydrogen vibrational modes. The result can be used to model bond length, vibration frequency and adsorption site of the adsorbed hydrogen.

5 Summary

The aims of this work were to upgrade the helium atom scattering apparatus H.A.N.S for enabling hydrogen adsorption experiments and to carry out the first helium scattering measurements on the H/Sb(111) system. Both objectives have been achieved.

The source for atomic hydrogen can be operated easily following the provided manual. Furthermore, the proof for successful hydrogen dissociation is given and an estimation of the effective pressure at the capillary outlet can be found, which is important for determining the dosage.

The theoretical part of the thesis deals with basic concepts of surface physics with special focus on the mechanism of hydrogen adsorption on various surfaces. Also the basics of helium atom scattering are given, where the applicability of the method on adsorption systems is discussed in more detail. For analysing the gained elastic HAS measurements to reveal the surface structure and its electronic corrugation, the quantum mechanical Close-Coupling (CC) approach is presented to calculate the scattering intensities. Also the CC treatment is applied onto the clean Sb(111) surface to reveal the interaction potential with the probing He-atom and to determine the surface corrugation, which is important for adsorption and diffusion processes.
For the clean Sb(111) surface, a Shifted Hybrid Morse Potential reproduced the measurements best, when assuming a peak to peak corrugation of about 15 % of the lattice constant (a = 4.31 Å).

The performed elastic HAS measurements on the H/Sb(111) system indicate two adsorption phases: At low surface temperatures (-160°C) the hydrogen atoms adsorb randomly distributed, which cancels any coherent diffraction. At elevated temperatures the diffraction pattern is recovered, only lowered in intensity compared to the clean surface, which suggests an ordered (1x1) superstructure with the atoms adsorbed on the three fold sites of the hexagonal Sb(111) lattice. The clean Sb(111) surface can be regained

by annealing the sample at 200°C. Interestingly, atomic hydrogen "cleaned" the Sb(111) surface from residual carbon contamination which has been shown by Auger electron spectroscopy. This fact indicates a surface reaction of hydrogen with carbon, forming a molecule which is desorbed from the surface before hydrogen adsorption starts. Molecular hydrogen on the contrary, showed no influence on the surface structure within the observed temperature range.

The described experiments have been the first adsorption experiments carried out on the H.A.N.S apparatus. Although the ability of the apparatus for investigating adsorption systems has been shown successfully, the results and interpretations are still of qualitative nature. For more exact and quantitative statements further experiments and a closer analysis will be necessary in the future. Suggestions are given within the thesis.

6 Danksagung

Das erste Dankeschön gilt meinem Betreuer Professor Wolfgang E. Ernst, der mir von Beginn an großes Vertrauen und seine ständige Unterstützung schenkte.
Besonders bedanken möchte ich mich aber auch bei meinen zwei großen Mentoren, Patrick und Michael, die mir nicht nur alle für meine Arbeit wichtigen physikalische Themen in schonender, frustfreier und sogar amüsanter Weise näherbrachten, sondern auch (und nicht weniger wichtig), mich im Umgang mit unserer sehr sensiblen und launischen Anlage mit viel Geduld einwiesen. Um gegenüber bisweilen zermürbender Laborarbeit, kopfzerbrechender Theorie und frustrierender Analysestunden zu bestehen, stand mir zusätzlich ein treuer Gefährte, Florian "Apo", stets zu Seite. Das gleiche Schicksal teilend, konnten wir durch gegenseitige moralische und fachliche Unterstützung so manche schwere Phase in eine bereichernde und lehrreiche Zeit verwandeln, in der neben guter Arbeit der gebührende Spaß nie zu kurz gekommen ist. An dieser Stelle möchte ich auch dem gesamten Institut danken, das mich so freundlich aufgenommen hat.
Wichtigen sozialen Support, um hin und wieder die Gedanken von der Arbeit zu befreien und auch die süßen Seiten des Lebens nicht zu vernachlässigen, leisteten Freunde und Studienkollegen immer genau dann, wenn es am Nötigsten war. Danke Berni, danke Michi, danke Raph und Andi, danke Nerds und vor allem; danke liebe Carina!
Erholsame Wochenenden und unersetzliche Unterstützung schenkte mir nicht zuletzt meine ganze Familie und viele Freunde zu Hause, denen ich auch von Herzen danken möchte.

7 Bibliography

[1] A. Tamtögl, M. Mayrhofer-Reinhartshuber, N. Balak, W. E. Ernst, and K. H. Rieder. Elastic and inelastic scattering of He atoms from Bi(111). *J. Phys.-Cond. Mat.*, 22:1–6, 2010.

[2] M. Mayrhofer-Reinhartshuber, A. Tamtögl, P. Kraus, K. H. Rieder, and W. E. Ernst. Vibrational dynamics and surface structure of Bi(111) from helium atom scattering measurements. *J. Phys.-Cond. Mat.*, 24:035410, 2012.

[3] A. Tamtögl, P. Kraus, M. Mayrhofer-Reinhartshuber, D. Campi, M. Bernasconi, G. Benedek, and W. E. Ernst. Surface and subsurface phonons of Bi(111) measured with helium atom scattering. *Phys. Rev. B*, 87:035410, 2013.

[4] A. Tamtögl, M. Mayrhofer-Reinhartshuber, P. Kraus, and W. E. Ernst. Surface Debye temperature and vibrational dynamics of Antimony(111) from helium atom scattering measurements. *Surface Science*, 617(0):225 – 228, 2013. ISSN 0039-6028. doi: http://dx.doi.org/10.1016/j.susc.2013.08.001. URL `http://www.sciencedirect.com/science/article/pii/S0039602813002252`.

[5] P. Kraus, A. Tamtögl, M. Mayrhofer-Reinhartshuber, G. Benedek, and W. E. Ernst. Resonance-enhanced inelastic He-atom scattering from subsurface optical phonons of Bi(111). *Phys. Rev. B*, 87:245433, Jun 2013. doi: 10.1103/PhysRevB.87.245433. URL `http://link.aps.org/doi/10.1103/PhysRevB.87.245433`.

[6] M. Mayrhofer-Reinhartshuber, A. Tamtögl, P. Kraus, and W. E. Ernst. Helium atom scattering investigation of the Sb(111) surface. *J. Phys.: Condens. Matter*, 25 (39):395002, 2013. URL `http://stacks.iop.org/0953-8984/25/i=39/a=395002`.

[7] M. Mayrhofer-Reinhartshuber, P. Kraus, A. Tamtögl, S. Miret-Artés, and W. E. Ernst. Helium-surface interaction potential of Sb(111) from scattering experiments and close-coupling calculations. *Phys. Rev. B*, 88:205425, Nov 2013. doi: 10.1103/PhysRevB.88.205425. URL `http://link.aps.org/doi/10.1103/PhysRevB.88.205425`.

[8] P. Kraus, M. Mayrhofer-Reinhartshuber, Ch. Gösweiner, F. Apolloner, S. Miret-Artés, and W. E. Ernst. A Comparative Study of the He-Sb(111) Interaction Potential from Close-Coupling Calculations and Helium Atom Scattering Experiments. *Surface Science*, 630:208–215, 2014.

[9] Axel Groß. Hydrogen on metal surfaces: Forever young. *Surface Science*, 606(7-8): 690 – 691, 2012.

[10] Hans Lüth. *Solid Surfaces, Interfaces and Thin Films*. Springer, fourth edition, 2001.

[11] C. Kittel. *Introduction to Solid State Physics*. Wiley, 2004. ISBN 978-0-4714-1526-8.

[12] N.D. Mermin N. W. Ashcroft. *Festkörperphysik*. Oldenbourg, 2005.

[13] Andrew Zangwill. *Physics at Surfaces*. Cambridge University Press, 1996.

[14] G. A. Somorjai. *Chemistry in two Dimensions: Surfaces*. Cornell University, 1981.

[15] Peter Ferrin, Shampa Kandoi, Anand Udaykumar Nilekar, and Manos Mavrikakis. Hydrogen adsorption, absorption and diffusion on and in transition metal surfaces: A DFT study. *Surface Science*, 606:679 – 689, 2012. ISSN 0039-6028.

[16] D. Hsieh, Y. Xia, L. Wray, D. Qian, A. Pal, J. H. Dil, J. Osterwalder, F. Meier, G. Bihlmayer, C. L. Kane, Y. S. Hor, R. J. Cava, and M. Z. Hasan. Observation of unconventional quantum spin textures in topological insulators. *Science*, 323(5916): 919–922, 2009. doi: 10.1126/science.1167733. URL `http://www.sciencemag.org/content/323/5916/919.abstract`.

[17] A. Ogg. XV. The crystalline structure of antimony and bismuth. *Philosophical Magazine Series 6*, 42(247):163–166, 1921. doi: 10.1080/14786442108633744. URL `http://www.tandfonline.com/doi/abs/10.1080/14786442108633744`.

[18] B. Stegemann, C. Ritter, B. Kaiser, and K. Rademann. Characterization of the (0001) cleavage surface of antimony single crystals using scanning probe microscopy: Atomic structure, vacancies, cleavage steps, and twinned interlayers. *Phys. Rev. B*, 69:155432, Apr 2004. doi: 10.1103/PhysRevB.69.155432. URL `http://link.aps.org/doi/10.1103/PhysRevB.69.155432`.

[19] F. Jona. Low-energy electron diffraction study of surfaces of antimony and bismuth. *Surface Science*, 8(1–2):57 – 76, 1967. ISSN 0039-6028. doi: 10.1016/0039-6028(67)90073-8. URL http://www.sciencedirect.com/science/article/pii/0039602867900738.

[20] Rosenberg, A. J., A. A. Menna, and T. P. Turnbull. Kinetics of the oxidation of antimony. *Journal of The Electrochemical Society*, 107(3):196–199, 1960. doi: 10.1149/1.2427650. URL http://jes.ecsdl.org/content/107/3/196.abstract.

[21] H. Sormann and E. Schachinger. Theoretische Festkörperphysik, 2012. URL https://itp.tugraz.at/LV/ewald/TFKP/.

[22] D. Campi, M. Bernasconi, and G. Benedek. Phonons and electron-phonon interaction at the Sb(111) surface. *Phys. Rev. B*, 86:075446, Aug 2012. doi: 10.1103/PhysRevB.86.075446. URL http://link.aps.org/doi/10.1103/PhysRevB.86.075446.

[23] D. Neuhaus. *Helium Atom Scattering from Surfaces*. Springer, 1992.

[24] D. Neuhaus, F. Joo, and B. Feuerbacher. Adsorbate-induced surface-phonon softening on Pt(111). *Phys. Rev. Lett.*, 58:694–697, Feb 1987. doi: 10.1103/PhysRevLett.58.694. URL http://link.aps.org/doi/10.1103/PhysRevLett.58.694.

[25] J.P. Toennies. Scattering of Molecular Beams from Surfaces. *Applied Physics*, 3(2):91–114, 1973. ISSN 0340-3793. doi: 10.1007/BF00884407. URL http://dx.doi.org/10.1007/BF00884407.

[26] Daniel Farías and Karl-Heinz Rieder. Atomic beam diffraction from solid surfaces. *Rep. Prog. Phys.*, (61):1575–1664, 1998.

[27] R.B. Doak. *Helium Atom Scattering from Surfaces*. Springer, 1992.

[28] Bene Poelsema and George Comsa. *Scattering of Thermal Energy Atoms from Disorderd Surfaces*. Springer, 1989.

[29] J. Peter Toennies. Phonon inelastic scattering of He atoms from single crystal surfaces. *Journal of Vacuum Science & Technology A*, 2(2):1055–1065, 1984. doi: http://dx.doi.org/10.1116/1.572655. URL http://scitation.aip.org/content/avs/journal/jvsta/2/2/10.1116/1.572655.

[30] G. Benedek, M. Pardo, and J. P. Toennies. Theory of inealstic atom scattering from surface electron-hole and plasmon excitation. *In Conference Proceedings Vol. 94, "Highlights on Spectroscopies of Semiconductors and Nanostructures", SIF, Bologna*, 2007.

[31] A. Tamtögl. *Surface Dynamics and Structure of Bi(111) from Helium Atom Scattering.* PhD thesis, Graz University of Technology, 2012.

[32] A. S. Sanz and S. Miret-Artés. Selective adsorption resonances: Quantum and stochastic approaches. *Phys. Rep.*, 451:37, October 2007. ISSN 0370-1573. URL `http://www.sciencedirect.com/science/article/pii/S0370157307003250`.

[33] H. Hoinkes. The physical interaction potential of gas atoms with single-crystal surfaces, determined from gas-surface diffraction experiments. *Rev. Mod. Phys.*, 52: 933–970, 1980.

[34] V. Celli. *Helium Atom Scattering from Surfaces.* Springer, 1992.

[35] W. A. Steele. *The Interaction of Gases with Solid Surfaces.* Pergamon Press Ltd., 1974.

[36] M. Mayrhofer-Reinhartshuber. Helium Atom Scattering from Surfaces including the Pseudo Random Chopper Technique. Master's thesis, Graz University of Technology, 2010.

[37] P. Kraus. *Classical and quantum-mechanical atom-surface interaction models applied to He-scattering measurements on Bi(111) and Sb(111).* PhD thesis, Graz University of Technology, 2014.

[38] A. F. Devonshire. The Interaction of Atoms and Molecules with Solid Surfaces. V. The Diffraction and Reflexion of Molecular Rays. *Proceedings of the Royal Society of London. Series A, Mathematical and Physical Sciences*, 156(887):pp. 37–44, 1936. ISSN 00804630. URL `http://www.jstor.org/stable/96713`.

[39] J. E. Lennard-Jones and A. F. Devonshire. The Interaction of Atoms and Molecules with Solid Surfaces. VII. The Diffraction of Atoms by a Surface. *Proceedings of the Royal Society of London. Series A-Mathematical and Physical Sciences*, 158(894): 253–268, 1937. URL `http://rspa.royalsocietypublishing.org/content/158/894/253.full.pdf`.

[40] C.Schwartz, M. W. Cole, and J. Plíva. Semiempirical determination of the atom-surface interaction. *Surface Science*, 75(1):1 – 16, 1978. ISSN 0039-6028. doi: http://dx.doi.org/10.1016/0039-6028(78)90048-1. URL http://www.sciencedirect.com/science/article/pii/0039602878900481.

[41] M. W. Cole and T. T. Tsong. Bound State vibrational Spectrum of the 3-9 Atom-Surface Interaction. *Surface Sci.*, 69:325–335, 1977.

[42] A. Tsuchida. Scattering of molecules by a crystal surface: I. He and LiF surface. *Surface Science*, 14(2):375 – 394, 1969. ISSN 0039-6028. doi: http://dx.doi.org/10.1016/0039-6028(69)90086-7. URL http://www.sciencedirect.com/science/article/pii/0039602869900867.

[43] H. Chow. Atomic band structure effects on resonant scattering of atoms from solid surfaces. *Surface Science*, 66(1):221 – 237, 1977. ISSN 0039-6028. doi: http://dx.doi.org/10.1016/0039-6028(77)90409-5. URL http://www.sciencedirect.com/science/article/pii/0039602877904095.

[44] L. Mattera, F. Rosatelli, C. Salvo, F. Tommasini, U. Valbusa, and G. Vidali. Selective adsorption of 1 H2 and 2 H2 on the (0001) graphite surface. *Surface Science*, 93(2):515–525, 1980. URL http://www.sciencedirect.com/science/article/pii/0039602880902794.

[45] Salvador Miret-Artés. Resonant inealstic scattering of atoms from surfaces. *Surface Science*, (339), 1995.

[46] B. Gumhalter. Different aspects of the Debye-Waller factor in various atom-surface scattering theories. *Surface Science*, 347(347):237–248, 1996.

[47] P. K. Johansson and B. N. J. Persson. On the Debye-Waller Factor in Molecular Beam Scattering Experiments. *Solid State Communications*, 36(36):271–273, 1980.

[48] A. C. Levi. Quantum Theory of Atom-Surface Scattering: Debye-Waller Factor. *Surface Science*, 88(88):221–254, 1979.

[49] P. Kraus, A. Tamtögl, M. Mayrhofer-Reinhartshuber, F. Apolloner, Ch. Gösweiner, S. Miret-Artés, and W. E. Ernst. The surface structure of Bi(111) calculated from Helium Atom Scattering measurements using the inelastic Close Coupling formalism. *Physical Review B*, submitted, 2014.

[50] J. Frenkel. Theorie der Adsorption und verwandter Erscheinungen. *Zeitschrift für Physik*, 26(1):117–138, 1924. ISSN 0044-3328. doi: 10.1007/BF01327320. URL http://dx.doi.org/10.1007/BF01327320.

[51] K. Christmann. Interation of hydrogen with solid surfaces. *Surf. Sci. Rep.*, 9:1–163, 1988.

[52] John C. Tully. Theories of the dynamics of inealstic and reactive processes at surfaces. *Ann. Rev. Phys. Chem.*, 31, 1980.

[53] S. Andersson and J. Harris. Observation of Rotational Transitions for H_2, D_2, and HD Adsorbed on Cu(100). *Phys. Rev. Lett.*, 48:545–548, Feb 1982. doi: 10.1103/PhysRevLett.48.545. URL http://link.aps.org/doi/10.1103/PhysRevLett.48.545.

[54] Peter Nordlander and Claes Holmberg. Physisorption interaction of H2 with noble metals. *Surface Science*, 152:702–709, 1984.

[55] Peter Nordlander and Claes Holmberg. Physisorption interaction of H2 with simple metals. *Surface Science*, 175, 1986.

[56] S. C. Wang and R. Gomer. Diffusion of hydrogen, deuterium, and tritium on the (110) plane of tungsten. *The Journal of Chemical Physics*, 83(8):4193–4209, 1985. doi: http://dx.doi.org/10.1063/1.449084. URL http://scitation.aip.org/content/aip/journal/jcp/83/8/10.1063/1.449084.

[57] David A. King. Thermal desorption from metal surfaces: A review. *Surface Science*, 47(1):384 – 402, 1975. ISSN 0039-6028. doi: http://dx.doi.org/10.1016/0039-6028(75)90302-7. URL http://www.sciencedirect.com/science/article/pii/0039602875903027. Proceedings of the Third Symposium on Surface Physics University of Utrecht, The Netherlands 26-28 June 1974.

[58] A.M. de Jong and J.W. Niemantsverdriet. Thermal desorption analysis: Comparative test of ten commonly applied procedures. *Surface Science*, 233(3):355 – 365, 1990. ISSN 0039-6028. doi: http://dx.doi.org/10.1016/0039-6028(90)90649-S. URL http://www.sciencedirect.com/science/article/pii/003960289090649S.

[59] D. Farías, M. Patting, and K. H. Rieder. A helium atom scattering study of the H/NiAl(110) adsorption system. *The Journal of Chemical Physics*, 117(4):1797–

1803, 2002. doi: http://dx.doi.org/10.1063/1.1486216. URL http://scitation.aip.org/content/aip/journal/jcp/117/4/10.1063/1.1486216.

[60] Ch Wöll. Hydrogen adsorption on metal oxide surfaces: a reinvestigation using He-atom scattering. *Journal of Physics: Condensed Matter*, 16(29):S2981, 2004. URL http://stacks.iop.org/0953-8984/16/i=29/a=012.

[61] R. Apel, D. Farías, H. Tröger, E. Kirsten, and K.H. Rieder. Atomic beam diffraction and resonant scattering studies of clean Rh(311) and the c(1x1)H phase. *Surface Science*, 364(3):303 – 311, 1996.

[62] Bene Poelsema, Robert L. Palmer, Günter Mechtersheimer, and George Comsa. Helium Scattering as a probe of the clean and adsorbate covered Pt(111) surface. *Surface Science*, 117:60–66, 1982.

[63] Klaus Kern, Peter Zeppenfeld, Rudolf David, and George Comsa. Two-dimensional phase transitions studied by thermal He scattering. *Journal of Vacuum Science & Technology A*, 6(639), 1987.

[64] Bene Poelsema, Siebe T. de Zwart, and George Comsa. Scattering Cross Section of Low-Coverage CO on Pt(111) from Thermal He and H2 Beams. *Physical Review Letters*, 49(8):578–581, 1982.

[65] G. Armand, L. Schwenger, and H.-J. Ernst. Helum-adsorbate cross section on highly corrugated substrates. *Physical Review B*, 53(8), 1996.

[66] B. H. Choi, A. P. Graham, K. T. Tang, and J. P. Toennies. Helium atom scattering from isolated CO molecules on a Pt(111) surface: Experiments versus close-coupling Calculations for a realistic He-CO potential. *Journal of Chemical Physics*, 112(23), 2000.

[67] Bene Poelsema, Larens K. Verheij, and George Comsa. Direct Evidence for Two.-Dimensional Xe Gas.Solid Phase Transition on Pt(111) by Means of Thermal He Scattering. *Physical Review Letters*, 1983.

[68] J.W.M. Frenken and B.J. Hinch. *Helium Atom Scattering from Surfaces*. Springer, 1992.

[69] A. P. Graham, A. Menzel, and J. P.Toennies. Qusielastic helium atom scattering measurements of microscopic diffusional dynamics of H and D on the Pt(111) surface. *Journal of Chemical Physics*, 111(4), 1999.

[70] B. H. Choi, A. P. Graham, K. T. Tang, and J. P. Toennies. Scattering from isolated molecules on metal surfaces: The relationship between elastic and inealstic intensities. *Journal of Chemical Physics*, 2002.

[71] N. Balak. Charakterisierung, Aufbau und Steuerung einer Ultrahochvakuum Atomstrahlanlage. Master's thesis, Graz University of Technology, 2009.

[72] D. R. Miller. *Atomic and Molecular Beam Methods*, volume 1, chapter 2, pages 14–53. Oxford University Press, 1983.

[73] T. Reisinger, G. Bracco, S. Rehbein, G. Schmahl, W. E. Ernst, and B. Holst. Direct Images of the Virtual Source in a Supersonic Expansion. *J. Phys. Chem. A*, 111 (111):12620, 2007.

[74] H. Pauly. *Atom, Molecule, and Cluster Beams I.* U.S. Government Printing Office, 2000.

[75] Mayrhofer-Reinhartshuber. *Surface Structure and Dynamics of Bi(111) and Sb(111) from He Atom Scattering Experiments.* PhD thesis, Graz University of Technology, 2014.

[76] G. Comsa. Coherence length and/or transfer width. *Surface Science*, 81(1):57–68, 1979.

[77] U. Bischler and E. Bertel. Simple source of atom hydrogen for ultrahigh vacuum application. *Jounal of Vacuum Science & Technology A*, 11(11):458, 1993.

[78] G. Lackner C. Eibl and A. Winkler. Quantitative characterization of a highly effective atatom hydrogen doser. *Journal of Vacuum Science & Technology A*, 16 (16):2979, 1998.

[79] K. G. Tschersich and V. von Bonin. Formation of an atomic hydrogen beam by a hot capillary. *Journal of Applied Physics*, 84(84):4065, 1998.

[80] L. Marx. Inbetriebnahme einer atomaren Wasserstoffquelle, 2012.

[81] Markus Polanz. Helium atom scattering measurements of the sb(111) surface icluding the close cpupling algorithm. Master's thesis, Graz University of Technology, 2013.

[82] R. Martínez-Casado, G. Mallia, D. Usvyat, L. Maschio, and S. Casassa. He-atom scattering from MgO(100): calculating diffraction peak intensities with a semi ab initio potential. *Phys. Chem. Chem. Phys.*, 13(14750):7, 2011.

[83] R. Smoluchowski. Anisotropy of the Electronic Work Function of Metals. *Phys. Rev.*, 60(9):661–674, November 1941. URL `http://link.aps.org/doi/10.1103/PhysRev.60.661`.

[84] P. A. Redhead. Thermal Desorption of Gases. *Vacuum*, 12:203, 1962.